Mechanistic Models of Cardiac Action Potentials and Drug Effects in Rabbit Ventricular Myocytes

Zhechao Yang

Submitted in fulfilment of the requirements for the

Degree of Doctor of Philosophy

School of Mathematics and Statistics

College of Science and Engineering

University of Glasgow

February 2026

Declaration

I, Zhechao Yang, declare that this thesis and the work presented in it are my own. I confirm that where I have consulted the published work of others, this is always clearly attributed. The first published work [1] is introduced in Chapter 4 and the second published work [2] is introduced in Chapter 5.

Published works

Yang Z, Gao H, Smith GL, Simitev RD. (2025) Dominant ionic currents in rabbit ventricular action potential dynamics. PLoS One 20(7): e0328261. doi.org/10.1371/ journal.pone.0328261.

Simitev, R. , Gilchrist, R., Yang, Z., Myles, R. , Burton, F. and Smith, G. (2025) A large population of cell-specific action potential models replicating fluorescence recordings of voltage in rabbit ventricular myocytes. Royal Society Open Science, 12(3): 241539, 2025. doi.org/10.1098/rsos.241539.

Abstract

The heart's rhythmic electrical activity is governed by a complex interplay of ionic currents, which vary significantly between cells and individuals. Accurately modelling this variability is crucial for understanding normal cardiac function and predicting the impact of therapeutic interventions. This thesis presents three complementary studies in computational cardiac electrophysiology, focusing on parameter sensitivity, intercellular variability, and pharmacodynamic modelling in rabbit ventricular myocytes.

First, a global Sobol sensitivity analysis was applied to the Shannon model of rabbit ventricular action potentials to determine the ionic currents most influential in shaping key electrophysiological biomarkers. This analysis identified the background chloride current (I_{Clb}) as the primary driver of variability, with substantial contributions from I_{K1}, I_{Kr}, I_{Ks}, I_{NaCa}, I_{tos}, and I_{CaL}. A reduced model retaining just six conductances was shown to reliably reproduce action potential duration and other biomarkers across varying conditions, streamlining future personalization efforts.

In the second study, fluorescence voltage recordings from over 1,200 rabbit ventricular myocytes provided by Professor Godfrey Smith from University of Glasgow were used to generate a population of cell-specific action potential models. Each model was individually fitted to replicate the full waveform of a single cell. This approach captured the natural variability in electrophysiological properties across the population and revealed that action potential metrics such as duration are maintained through complex interactions among weakly correlated ionic parameters. The results demonstrate the feasibility of high-throughput, cell-level model calibra-

tion and underscore the importance of considering inter-cellular variability in cardiac simulations.

Finally, the third project explored the pharmacodynamics of the anti-arrhythmic drug dofetilide. By integrating paired recordings of action potentials before and after drug application, a novel model-based framework was developed to test the predictive accuracy of inferred conductances. Dofetilide-induced changes in action potential duration were simulated by scaling the rapid delayed rectifier potassium current (I_{Kr}), and predictions were validated across four drug concentrations. The results demonstrated strong model performance at lower concentrations and highlighted increasing variability at higher doses, underscoring the need for more comprehensive models at therapeutic extremes.

Together, these studies emphasize the importance of accurate parameter identification, the role of cellular heterogeneity in shaping electrophysiological behavior, and the value of mechanistic modelling in drug safety assessment. This work advances the field toward personalized cardiac modelling and improves our ability to predict both natural and drug-modified electrical dynamics in the heart.

Acknowledgements

I would like to thank my supervisors, Prof Radostin Simitev, and Dr Hao Gao. You have been a constant source of guidance and patience. I have really enjoyed my PhD and it would not have been possible without you.

To the whole SofTMech team, I want to thank you not only for your funding, but also for providing me with inspiration and irreplaceable experiences that will last a lifetime.

To Mum and Dad, thank you for all your help and encouragement over all these years of study. Without you it would not have been possible and I would not be where I am today.

Finally, to David Gilmour, Mark Knopfler, Camel and Eric Clapton, thank you for your music giving me power, especially when I feel gutted and frustrated.

Contents

List of Figures

List of Tables

Chapter 1

Introduction

The heart is a finely tuned organ whose function depends on tightly regulated electrical activity at the cellular level. This electrical activity is governed by a variety of interacting ionic currents that generate and shape the cardiac action potential (AP)—the fundamental carrier of electrical signaling in the heart. Variation in these ionic currents, whether natural or drug-induced, can significantly influence cellular behavior and, in turn, whole-organ function. The work presented in this thesis focuses on quantifying, modelling, and predicting these variations using mathematical models of cardiac electrophysiology. Particular emphasis is placed on the role of inter-cellular variability and pharmacological modulation in shaping electrical behavior. These themes are explored through three novel studies, as outlined below.

1. **Chapter 4: Sensitivity Analysis of Ionic Currents in Rabbit Ventricular Myocytes:** A global Sobol sensitivity analysis is applied to the Shannon model [3] to identify the ionic currents most responsible for variability in AP biomarkers. This study highlights the dominant role of the background chloride current and provides a reduced model formulation capable of accurately reproducing key electrophysiological features. These results have been published in Yang et al.[1].

2. **Chapter 5: Population-Based Modelling of Cell-Specific APs:** A large population of cell-specific models is calibrated to fluorescence voltage recordings from over 1,200 rabbit ventricular myocytes. Each model captures the full

waveform of a single cell, enabling an exploration of natural electrophysiological variability and parameter interdependence within healthy myocytes. These findings have been published in Simitev et al.[2]

3. **Chapter 6: Mechanistic Modelling of Anti-Arrhythmic Drug Effects:** Mechanistic models of cardiac electrophysiology, expressed as systems of ordinary differential equations, provide a framework to interpret effects of anti-arrhythmic drugs in terms of biophysically meaningful parameters. This study enables me to directly assess and predict drug-induced changes in ionic conductances, creating a foundation for high-throughput tools in pre-clinical pharmacology.

In order to address these questions, complicated systems governing cardiac electrical behavior at the cellular level need to be considered. The remaining chapters introduce the biological and mathematical background necessary for this work, including an overview of cardiac cell types, electrophysiological mechanisms, and the modelling frameworks used throughout the thesis.

1.1 Project 1: Dominant Ionic Currents in Rabbit Ventricular AP Dynamics

The first piece of novel work is to identify sensitive parameters in cardiac cellular electrophysiology. The aim of the project is to rank the parameters of a realistic mathematical model of the rabbit ventricular AP in terms of their influence on the model outputs. Such ranking has a number of applications, for instance generating reduced-order models from the full system, proposing hypothetical targets for pharmacological intervention, or for parameter estimation from data, as indeed attempted in the second project.

Mathematical models of cardiac APs are essential tools for studying the electrical activity of cardiac cells and understanding their physiological and pathological behaviors. In this work, I conduct a global sensitivity analysis of a mathematical model of rabbit ventricular myocyte APs, and rank key parameters based on their impact on aspects of the model's output.

Ventricular APs are transient deviations from the resting electrical potential across the sarcolemma, and play an essential role in cardiac function. They are triggered by electrical stimuli and dynamically sustained by ionic conductance changes regulated by voltage and ion concentrations. The complexity of the underlying cellular processes and structures necessitates nonlinear, stiff, and high dimensional mathematical models of the AP [4]. Consequently, their analysis, numerical simulation, and comparison with experimental data is challenging. Often a model reduction is needed to a simplified system while retaining the predictive power of the original model.

A widely used approach for model reduction and simplification is sensitivity analysis. This method can be viewed as an optimization problem, where the objective is to minimize the model's dimensionality while ensuring that the discrepancy between the outputs of the original and reduced models remains sufficiently small. In practice, this involves identifying model quantities whose variations have negligible impact on the output and replacing them with appropriate constants. Compared to other model reduction techniques such as variable lumping, coordinate transformations, manifold reduction, truncation via singular value decomposition, or homogenization, sensitivity analysis offers a key advantage: it retains the physiological interpretability of model variables, parameters, and components [5].

This study is motivated by the need to model recent experimental measurements reported by [6]. In that work, AP waveforms were measured in hundreds of isolated rabbit ventricular myocytes, both before and after drug administration. Cells were sourced from various regions of the left ventricle across multiple animals. The most surprising finding was that AP waveforms varied more significantly between individual cells than between regions or even between different animals. Cell-specific mathematical models are required to capture this pronounced cell-to-cell variability. Such models can be developed by adjusting a subset of parameters in a generic baseline model, such as [3]. To achieve this, a critical step is understanding how variations in parameter values influence the AP waveform. The overall goal of this study is to perform this sensitivity analysis, with specific objectives outlined further below.

Goals	Methods & Models	Results
Gemmell et al. [7]		
•To perform a systematic exploration of the effects of simultaneously varying the magnitude of six transmembrane current conductances in two rabbit-specific ventricular AP models.	•Clutter-based dimension reordering. •Rabbit-specific ventricular AP model: [3].	•$g_{\mathrm{Ca,L}}$ had the greatest influence on AP duration variability at both 400 and 1000 ms, along with g_{K1} and g_{to} at 400 and 1000 ms, respectively.
Sobie [8]		
•To investigate how maximum ion channel conductances affect the outputs of a simplified cardiac cell model, specifically focusing on AP shape and restitution.	•Multivariable Regression. •Cardiac cell models: [9], [10], [11].	•Blocking rapid delayed rectifier current (I_{Kr}) causes a greater prolongation of AP duration than blocking slow delayed rectifier current (I_{Ks}), which has little effect. Changes in inward rectifier current (I_{K1}) have a much greater effect on AP duration than changes in I_{Kr} in the model of [10].
Coveney & Clayton [12]		

Continued on next page

Continued from previous page

Goals	Methods & Models	Results
•To study how different ionic conductances in two cardiac cell models affect the AP duration and other electrophysiological properties.	•Variance based sensitivity analysis. •Cardiac cell models: [13], [14].	•Changes in maximum conductance of the ultra-rapid K + channel (I_{Kur}) would have opposite effects on AP duration.
Romero et al. [15]		
•To investigate the impact of variability in ionic currents on the electrophysiological properties of human ventricular cells.	•Local sensitivity analysis. •Human ventricular model: [16].	•AP duration is moderately sensitive to changes in maximal conductances of all currents involved in repolarization and also I_{Ks} and I_{CaL} kinetics.
Chang et al. [17]		
•To investigate how uncertainty in input parameters influences electrophysiological features and mechanical variables.	•Variance based sensitivity analysis. •Cardiac cell model: [9].	•The analysis showed that parameters like G_{si}, G_{K}, and G_{b} were crucial in determining the variability in AP duration, a key electrophysiological measure.
Romero et al. [18]		

Continued on next page

Continued from previous page

Goals	Methods & Models	Results
•To characterise the sensitivity of selected cellular biomarkers of arrhythmic risk to ionic current properties in rabbit ventricular models. •To compare with experimental data.	•Local sensitivity analysis.•Rabbit cell models: [3], [19].	•AP duration is significantly influenced by most repolarization currents. •APtriangulation is mainly regulated by I_{K1}.•AP duration restitution properties, and Ca_i^{2+} rate dependence arestrongly affected by I_{NaK}, I_{CaL} and I_{NaCa}.
Johnstone et al.[20]		
•To investigate the impact of variability in ionic currents on the electrophysiological properties of human ventricular cells.	•Variance based sensitivity analysis. •Human ventricular model: [16].	•V_{max} is sensitive to G_{Na}, G_{CaL}. V_{m}, A_{90} and A_{50} are both influenced by a similar group of inputs, and resting voltage is influenced by G_{K1} and pump currents.
Del Corso et al. [21]		

Continued on next page

Continued from previous page

Goals	Methods & Models	Results
•To identify which of the uncertain inputs mostly affect electrophysiology of the left ventricle.	•Variance based sensitivity analysis. •Cardiac cell model: [16].	•The most influential input parameters for AP duration and shape similarity are the maximal IKr, IKs and ICal conductances (G_{Kr}, G_{Ks} and G_{CaL}) along with the extracellular Ca and Na concentration.
Chang & Clayton [22]		
•To investigate the impact of variability in ionic currents on the electrophysiological properties of human ventricular cells.	•Variance based sensitivity analysis. •Cardiac cell model: [13].	•AP upstroke (max dV/dt) and maximum voltage were highly sensitive to G_{Na}. Dome voltage was most sensitive to G_{Kur} and G_{CaL}, whilst G_{K1} had a strong effect on A_{90} and resting voltage. A_{50} was most sensitive to G_{CaL}.
Pathmanathan et al. [23]		

Continued on next page

Continued from previous page

Goals	Methods & Models	Results
•To demonstrate feasibility of performing comprehensive UQ/SA for cardiac cell models and demonstrate how to assess robustness and overcome model failure when performing cardiac UQ analyses.	•Variance based sensitivity analysis. •Human ventricular model: [16].	•E_{h}, plays a dominant role in determining MaxUpstrokeVelocity. TimeOfMaxUpstrokeVelocity is controlled by three parameters E_{m}, k_{m} and E_{z}. (E_{h}, $\log(\delta_{\mathrm{h}})$, E_{r}, E_{d}, E_{f}), which were the parameters identified to be highly influential.
Mora et al. [24]		
•To study the electrical activity and ionic homeostasis of failing myocytes. •To compare with experimental data.	•Single-parameter sensitivity analysis. •Human ventricular model: modified [25].	•I_{NaL} and I_{NaK} are the most important contributors to AP duration variations. SERCA plays an important role in modulating Ca^{2+}, with the Na^{2+}/Ca^{2+} exchanger (NCX) and other Ca^{2+} cycling proteins also playing a significant role.
Sadrieh et al. [26]		

Continued on next page

Continued from previous page

Goals	Methods & Models	Results
•To extend existing sensitivity analyses to electrocardiogram (ECG) signals derived from multicellular systems and quantify the contribution of ionic conductances to emergent properties of the ECG.	•Partial least squares analysis. •Human ventricular model: [25].	•A_{90} is approximately fourfold more sensitive to changes in G_{CaL} than in isolated cells but less sensitive to changes in G_{K1} and G_{ncx}.
Parikh et al. [27]		
•To apply global sensitivity analysis to the existing Comprehensive in vitro Proarrhythmia Assay (CiPA) in silico framework to identify the key model components that derived metrics are most sensitive to.	•Variance based sensitivity analysis. •Human ventricular model: CiPAORd model, modified from [25].	•The Sobol sensitivity indices indicate that A_{90} is the most sensitive to sbIKr block, qNet to sbINaL, and peakCa to bICaL.

Table 1.1: Selected works on sensitivity analysis of cardiac cellular electrophysiology models

There is a substantial body of literature on sensitivity analysis of detailed cardiac AP models, with a selection of the most notable studies summarized in Table 1.1. Among these, only the work of [18] specifically addressed rabbit ventricular AP models. Their study systematically investigated how parameter variations affect a wide range of electrophysiological properties, including steady-state AP and intracellular

calcium concentrations ($[Ca^{2+}]_i$), AP duration and triangulation, AP duration rate dependence and restitution curves, and AP duration adaptation to abrupt changes in basic cycle length (BCL). A major limitation of [18] is its use of local sensitivity analysis, where parameters are varied by fixed percentages ($\pm 15\%$ and $\pm 30\%$) around Shannon model baseline values. This approach is valid only near reference values and ignores interactions between multiple parameters. Experimental data from [6] show significant variability that the baseline Shannon model cannot capture, and its nonlinearity suggests parameter sensitivity varies across the space. Thus, global sensitivity analysis, which evaluates parameter influence across the full space and considers nonlinear interactions, is essential for a more complete understanding of model behaviour.

Several methods for global sensitivity analysis, including partial rank correlations and Fourier amplitude sensitivity, are well-documented in the literature [28]. For this study, I have chosen the Sobol global sensitivity method [29], based on its robustness and efficiency. Sobol's method quantifies the contribution of input variables or parameters to the variance of a model's output, helping to identify the most influential factors. A brief informal outline of the theoretical concepts behind Sobol analysis is provided further below.

Our work has three main objectives. First, I estimate Sobol sensitivity indices for all maximal current strength parameters in the Shannon model, focusing on their influence on selected AP biomarkers, including duration, plateau potential, and resting potential. Second, I rank these parameters based on their grand total Sobol sensitivity indices to identify the most influential ionic currents. Third, we validate these rankings and propose a hierarchy of reduced models, demonstrating that dimensionality reduction is feasible without significant loss of predictive accuracy.

1.2 Project 2: A Large Population of Cell-specific AP Models Replicating Fluorescence Recordings of Voltage in Rabbit Ventricular Myocytes

As discussed above, eight most influential parameters are determined by global sensitivity analysis and this can give a guideline for the choice of parameter estimation, leading to the next project. The second project, presented in Chapter 5, is to model a large population of cell-specific AP waveforms replicating fluorescence recordings of voltage in rabbit ventricular myocytes. The aim of the project is to perform statistical inference of a subset of the parameters given in project 1.1 of a realistic mathematical model of the rabbit ventricular AP from data provided by Professor Godfrey Smith from University of Glasgow for over 1200 experimentally measured cells. This is significant, because inter-cell variability is increasingly being found to be substantial, thus challenging the current paradigm that a typical cell electrophysiology exists. The methodology is also important due to increasing availability of automated measurements and large volumes of experimental data.

Despite sharing identical genetic backgrounds and being cultured under the same external conditions, individual cardiomyocytes often display noticeable differences in their electrical activity. These inter-cellular variations in electrophysiological behavior have been consistently observed across multiple species and experimental techniques [30, 31, 32]. This heterogeneity is clinically significant, for instance, therapeutic interventions targeting specific ion channels may have variable outcomes depending on the individual characteristics of each myocyte [33]. Since directly measuring the full spectrum of ionic conductance differences across a large number of cells is impractical, computational modelling offers an essential framework for exploring this variability at the cellular level.

Approaches to simulate cardiomyocyte diversity have evolved into two principal strategies: population-based modelling and sample-specific modelling [34, 35]. Both

begin with a well-established generic model of the cardiac AP appropriate for the species and tissue under study [4]. In the population-based approach, researchers generate a large number of model variants by sampling model parameters from assumed statistical distributions. These variants may then be filtered using experimental benchmarks to select only biologically plausible behaviors [15, 32]. In contrast, sample-specific modelling involves tailoring parameter sets to match the experimental data of individual cells [36]. Population-based models benefit from scalability and statistical power, enabling the construction of model populations with tens of thousands of members. This facilitates robust analysis of variability patterns. However, a major limitation lies in the lack of one-to-one correspondence between individual model variants and real cells, which can reduce their accuracy for predicting responses to stimuli or interventions. Sample-specific models, on the other hand, offer this precise mapping, allowing for individualized analysis and simulation. Yet, their reliance on rich datasets and intensive computational resources has limited their application to small-scale studies.

This work aims to bridge the gap between population-wide generality and cell-specific precision by integrating both approaches. Recent advancements have made this hybrid strategy feasible. High-throughput optical imaging techniques now allow for the rapid collection of voltage data from thousands of isolated cardiomyocytes [37, 38], and algorithmic improvements in parameter inference have enabled efficient model fitting at scale [39]. In earlier work by [6], voltage-sensitive fluorescent dyes were used to record AP waveforms from nearly 500 rabbit ventricular myocytes, identifying considerable variability in AP duration at 90% repolarization (A_{90}), with interquartile ranges up to 50 ms. A conventional population-based modelling analysis was performed using the Shannon model [3], with 50,000 randomized parameter sets filtered to match the A_{90} distribution. However, this analysis made limited use of the rich waveform data available, considering only a single biomarker (A_{90}) per cell.

1.3 Project 3: Mechanistic Modelling of Anti-Arrhythmic Drug Action from Paired Cardiac Cell Recordings

Dofetilide is a class III anti-arrhythmic agent that selectively inhibits the rapid delayed rectifier potassium current (I_{Kr}) and thereby prolongs cardiac repolarization [40]. Despite its well-established clinical relevance, quantitative estimates of I_{Kr} inhibition at different dofetilide concentrations remain inconsistent across studies. For example, reported unblocked fractions of 0.756 at 3 nM and 0.412 at 30 nM [41], to markedly different values reported by [42]. These discrepancies highlight the lack of consensus on how dofetilide modulates I_{Kr} across physiologically relevant concentrations (see Table 1.3).

Anti-arrhythmic drugs such as dofetilide act by modulating ionic currents that shape the cardiac AP. Mechanistic models of cardiac electrophysiology, expressed as systems of ordinary differential equations, provide a framework to interpret these effects in terms of biophysically meaningful parameters. To predict drug action reliably across heterogeneous cell populations, model parameters must be estimated directly from experimental data.

However, generating comprehensive drug-response experimental datasets presents practical challenges. Techniques such as manual patch-clamp electrophysiology, while offering high temporal and biophysical resolution, are inherently low-throughput, require highly trained personnel and expensive equipment, and often limit the number of concentrations and conditions that can be measured directly [43]. Even with automated platforms, consumable costs and infrastructure requirements elevate the overall investment for detailed drug screening [44]. More broadly, drug development is a long and costly process, with cardiac safety evaluations adding significant time and resource demands; reducing attrition and data sparsity at the preclinical level could yield substantial savings in time and expenditure [45]. These limitations mean that extensive drug-response measurements across all concentrations of interest are often unavailable or infeasible. Computational modelling thus plays an important role

in bridging gaps in experimental data by enabling prediction of drug effects where direct measurements are sparse and in guiding the design of targeted experiments.

In previous pilot work of 1.2, I developed a large population of cell-specific AP models calibrated to rabbit ventricular myocyte recordings. This framework provides a prototype for an open and reproducible workflow for parameter estimation and characterization of inter-cell variability. However, the estimated parameters were not directly validated against drug-response data, leaving open the question of their predictive robustness when applied to pharmacological perturbations.

This present study addresses this gap by explicitly modelling the pharmacodynamic effects of dofetilide at multiple concentrations, with the dual aims of (i) resolving uncertainty in the reported inhibition factor and (ii) testing the robustness of inferred conductances across different drug concentrations. Specifically, building upon prior work, this study introduces a novel and rigorous framework for quantifying drug effects. Previous studies have often relied on fitting models to single, pre-drug AP and ionic current recordings or optimizing models against aggregated data and published drug response factors. In contrast, I am the first to perform parameter estimation simultaneously on paired AP traces, one recorded before and one after dofetilide administration obtained from the same single biological myocyte. This multi-output optimization approach allows for the direct and precise inference of cell-specific drug inhibition parameters, such as the unblocked fraction, alongside the baseline cellular conductances, significantly enhancing the predictive robustness of the resulting models.

The main objectives of this study are twofold. Firstly, to identify and quantify the pharmacodynamic action of dofetilide by performing simultaneous parameter estimation using paired AP recordings obtained from the same biological cell before and after drug exposure. This is achieved through a multi-output optimization framework that simultaneously fits both waveforms, enabling the direct inference and validation of drug-induced modulation of ionic conductances rather than merely reproducing baseline electrophysiological behavior. Secondly, to estimate and validate cellular model parameters under the assumption that drug effects are known and fixed. Based on the drug action identified in the first objective, dofetilide is modelled via a prescribed

inhibition factor φ applied to $\hat{\alpha}_{\text{Kr}}$, the maximal conductance of I_{Kr}. This constrained estimation framework is used to assess whether conductance parameters inferred at a single drug concentration generalize across different concentrations, thereby enabling prediction of drug responses in scenarios where experimental recordings are limited or unavailable. There is a substantial body of literature on parameter estimation of detailed cardiac AP models, with a selection of the most notable studies summarized in Table 1.2.

By confronting uncertain pharmacodynamic data with detailed mathematical models, this work provides a systematic assessment of dofetilide action across concentrations and establishes a pipeline for a mechanistic, data-driven way to assess and compare potential anti-arrhythmic compounds at an early stage of drug development.

Goals	Methods & Models	Results
Li et al. [42]		
•To evaluate drug effects on multiple cardiac ion channels in vitro and using these data in a predictive in silico model of the adult human ventricular myocyte.	•Global optimization: Genetic Algorithm-based Parameterization for Systems Modelling (GAPSM). •Cardiac cell model: IKr-Dynamic ORd Model [25].	•modelling dynamic drug–hERG channel interactions and multi-ion channel pharmacology improves the prediction of torsadogenic risk. IC50s and Hill coefficients (hs) for dofetilide on hERG are 4.9 and 0.9 respectively.
Tsujimae et al. [41]		

Continued on next page

Continued from previous page

Goals	Methods & Models	Results
•To establish a human atrial AP model that can differentiate the effects of drugs and reproduce the reverse-frequency-dependent nature of dofetilide-type.	•Nonlinear least-squares fitting. •Cardiac cell model: [13].	•Slow activation and deactivation of IKs underlie the reverse-frequency-dependent atrial APD prolongation induced by IKr blockers. It also demonstrated that the effects of these compound types on APD prolongation depended on the kinetics of their interactions with IKr. Unblocked fractions of IKr are 0.159, 0.412, and 0.756 for 30, 100, and 300 nM dofetilide, respectively.
Li et al. [46]		

Continued on next page

Continued from previous page

Goals	Methods & Models	Results
•To apply the prespecified model and metric to independent CiPA validation drugs. To address whether mechanistic in silico models can show high TdP risk prediction accuracy in a rigorous prospective study specified by the newly proposed CiPA paradigm	•Global optimization: Covariance Matrix Adapting Evolutionary Strategy (CMAES). •Cardiac cell model: CiPAORdv1.0 Model [47].	•The CiPA in silico model and the qNet/torsade metric score metric demonstrate high accuracy in TdP risk prediction, which suggests it may be fit for regulatory use under the CiPA paradigm. Dofetilide exerts multi-channel influence on INa at higher concentrations, with unblocked fractions equal to 0.99, 0.95, 0.84 at 30, 100 and 300 nM respectively.
Mann et al. [48]		

Continued on next page

Continued from previous page

Goals	Methods & Models	Results
•To apply a global optimization approach to improve the existing in silico models so that they reproduced all three clinical data sets more closely.	•Global optimization: Pattern Search Algorithm. •Human ventricular model: O'Hara-Rudy Model [25].	•. In-silico models of cardiac electrophysiology have the potential to be tremendously useful in complementing traditional preclinical drug testing studies and they should be carefully validated and optimized to clinical data before they can be used for this purpose.
Krogh et al. [49]		

Continued on next page

Continued from previous page

Goals	Methods & Models	Results
•To determine if the model optimized to congenital long QT data better predicts risk of drug-induced long QT arrhythmogenesis, in particular Torsades de Pointes risk.	•Global optimization: Pattern Search Algorithm. •Human ventricular model: O'Hara-Rudy Model[25].	•Results underscore the importance of currents beyond those directly impacted by a drug block in determining torsadogenic risk. Study also highlights the need for rich data in cardiac myocyte model optimization and substantiates such optimization as a method to generate models with higher accuracy of predictions of drug-induced cardiotoxicity.
Dutta et al. [47]		

Continued on next page

Continued from previous page

Goals	Methods & Models	Results
•To optimize the IKr-dynamic ORd model by refining model parameters using published human cardiomyocyte experimental data under control and drug block conditions. To use this optimized model and manual patch clamp data, developing an updated version of the metric that quantifies the net electronic charge.	•Genetic Algorithm-based Parameterization for Systems Modelling (GAPSM). •Cardiac cell model: IKr-Dynamic ORd Model [25].	•This work presents an optimized model that is more consistent with experimental data, an improved metric that can classify drugs at concentrations both near and higher than clinical exposure, and a physiological framework to check the relationship between a metric and EAD.
Bot et al. [50]		
•To obtain additional insight into the ionic mechanisms responsible for the transmural AP heterogeneity.	•Genetic Algorithm. •Ventricular neonatal mouse cardiomyocyte model: Pandit et al. Model [51].	•Rapid GA optimization of a cell-specific mathematical model improves CTC performance and may therefore expand the applicability and usage of the CTC technique.

Table 1.2: Selected works on parameter estimation of cardiac cellular drug-induced electrophysiology models

Dofetilide concentration	3 nM	30 nM	100 nM	300 nM
Snyders & Chaudhary [52]	0.75-0.80	0.27-0.34	0.11-0.15	0.05-0.06
Li et al. [42]	0.61	0.16, 0.19[53]	0.06	0.02
Tsujimae et al. [41]	not available	0.756	0.412	0.159
Crumb et al. [54]	0.40	0.08	0.03	0.01
Kramer et al. [55]	0.85	0.50	0.25	0.11

Table 1.3: Investigation of the unblocked fraction for $I_{\mathbf{Kr}}$ at each dofetilide concentration.

1.4 Aims

Mathematical modelling has become an indispensable tool for exploring complex biological processes, and the work presented in this thesis further exemplifies its value in cardiac electrophysiology. Firstly, once a biophysically detailed model is constructed, it allows for rapid and cost-effective experimentation in silico, reducing dependence on laborious and expensive wet-lab protocols. Furthermore, mathematical models can reveal underlying ionic mechanisms that are challenging or impossible to measure experimentally, such as the individual contributions of membrane currents or transporters in shaping the AP. These insights not only advance theoretical understanding but also guide the design of future experimental investigations. Another key advantage is that simulation-based approaches are non-invasive, making them particularly useful for testing potential drug effects without posing risks to human or animal subjects. Additionally, personalized models offer the promise of predictive medicine by forecasting how an individual's cardiac cells might respond to various interventions, enabling earlier and more precise treatment.

Ultimately, this work contributes to identifying which model parameters must be estimated to accurately reproduce APs from optical recordings. This foundational step ensures that subsequent modelling efforts are both efficient and biologically relevant. Building on that, a scalable pipeline is presented for generating cell-specific models from high-throughput voltage imaging data. This approach captures the variability observed across real cells and overcomes key limitations of traditional population-based or manually calibrated models. The pipeline developed can be further refined to be applied to novel compounds with uncertain pharmaco-

dynamics, leading to a mechanistic, data-driven way to assess and compare potential anti-arrhythmic compounds at an early stage of drug development.

Chapter 2

Electrophysiological Background

In this chapter, the electrophysiological function of the heart is introduced with a particular focus on ventricular myocytes, their ionic mechanisms, and their roles in generating the cardiac AP. The aim is to provide a clear understanding of the biophysical principles that underlie the modelling and simulation efforts explored later in this thesis.

2.1 Introduction

The contraction of the heart is driven by a precisely orchestrated sequence of electrical events that originate within the heart itself. This intrinsic conduction system ensures that each chamber contracts at the appropriate time, allowing the heart to function as an efficient pump. The electrical activity begins in the sinoatrial (SA) node, often referred to as the natural pacemaker, located in the right atrium. From there, the signal propagates through the atrial myocardium, triggering atrial contraction, and then passes through the atrioventricular (AV) node, where conduction is briefly delayed. This delay allows the ventricles to fill with blood before contraction. The impulse then travels rapidly through the His-Purkinje system, activating the ventricles from apex to base, and ensuring efficient ejection of blood [56].

Structurally, the heart consists of four chambers: two atria and two ventricles, separated by valves and surrounded by specialized muscle tissue. The ventricles serve as the main pumping chambers, with the left ventricle generating higher pressures

to deliver oxygenated blood to the systemic circulation. To support this function, the ventricular wall is thicker and more muscular than that of the atria and this mechanical function is tightly coupled to the underlying electrical activation of the ventricular myocardium.

2.2 Cardiac Tissue and Cell Types

The ventricular wall is composed of three major layers: the epicardium, myocardium, and endocardium [57]. Among these, the myocardium constitutes the bulk of the ventricular mass and contains various cell types such as myocytes, fibroblasts, endothelial cells, and vascular smooth muscle cells [58]. By volume, the cardiac tissue is made up of approximately 75% myocytes. Myocytes are muscle cells [59]. This work will focus mainly on cardiac myocytes, also referred to as cardiomyocytes.

Cardiomyocytes are elongated, striated cells that contain a rich complement of ion channels, pumps, and exchangers embedded in their membranes. These proteins regulate ionic fluxes that determine the resting membrane potential, AP shape, and excitation–contraction coupling. Cardiomyocytes are connected via gap junctions, which allow for the passage of electrical current between cells, ensuring synchronous activation of the tissue [56].

2.3 Cellular Electrophysiology

Electrophysiology is the study of the electrical activity in biological systems, arising from the movement of ions across cell membranes. In the heart, this electrical activity underlies the initiation and coordination of contraction, enabling efficient pumping of blood. This thesis focuses on the electrophysiology of cardiac myocytes, the principal electrically active cells in the myocardium and on how their ionic currents and APs can be characterized, modeled, and used to investigate both physiological variability and the effects of pharmacological interventions.

The cell membrane, or sarcolemma in muscle cells, is a selectively permeable barrier that regulates the passage of ions and other molecules between the intracellular

and extracellular environments. Structurally, it consists of a bilayer of phospholipids, with hydrophilic heads facing outward toward aqueous environments and hydrophobic tails oriented inward. Embedded within this lipid matrix are membrane proteins, including ion channels, pumps, and exchangers, which control ionic movement [60].

Among these membrane proteins are ion channels, which enable ions to move across the membrane through either active or passive processes. Active transport requires the expenditure of metabolic energy, while passive transport relies on electrochemical gradients and does not consume energy directly. Because of the electrical charge of the ions, this results in a potential difference across the cell membrane, which is called the transmembrane potential, or simply the membrane potential. In cardiac electrophysiology, it is the generation, maintenance, and modulation of this membrane potential driven by the movement of ions that forms the basis of study.

2.3.1 Cellular Electrical Activity: AP Dynamics

The electrical behavior of cardiomyocytes is determined by the dynamics of AP, which in turn is governed by changes in membrane permeability and the resulting ionic currents. Ion movement is driven by both chemical gradients and electrical potentials. While sodium (Na^+), potassium (K^+), and calcium (Ca^{2+}) are the principal ions involved, each is regulated by multiple channel types whose expression varies between species and between atrial and ventricular tissue. In addition to sarcolemmal channels, cardiomyocytes contain ion channels in subcellular structures such as the sarcoplasmic reticulum and mitochondria [56].

Each ionic current contributes to specific phases of the ventricular AP, classically divided into five stages [61]:

Phase 0 – Rapid depolarisation: Activation by an adjacent cell increases Na^+ channel permeability, producing a rapid influx of Na^+ and a steep rise in membrane potential.

Phase 1 – Early repolarisation: Na^+ channels inactivate while K^+ channels open, causing a brief drop in membrane potential.

Phase 2 – Plateau: Inward Ca^{2+} currents and outward K^+ currents balance, maintaining a near-constant potential. Ca^{2+} entry during this phase triggers further Ca^{2+} release from the sarcoplasmic reticulum, initiating contraction.

Phase 3 – Repolarisation: Ca^{2+} channels inactivate while delayed rectifier K^+ currents dominate, restoring the resting potential.

Phase 4 – Resting: Na^+ and Ca^{2+} channels are minimally active. Inward rectifier K^+ currents maintain the resting membrane potential.

These important changes in ion channel activity define the time course and morphology of the cardiac AP and determine the electrical behavior of the myocyte. A typical AP waveform for a ventricular muscle cell is shown in Figure 2.1.

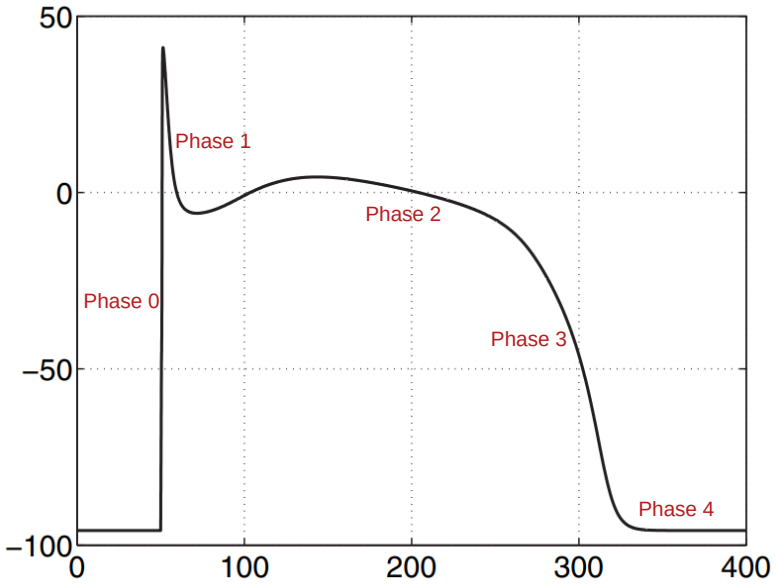

Figure 2.1: Schematic representation of the ventricular AP from a dog, showing the five classical phases (0–4). The AP is computed with a model by [62].

2.3.2 Cellular Variability

Cardiomyocytes, despite being genetically identical and exposed to uniform extracellular environments, often display striking differences in their electrophysiological properties. This variability has been well documented over several decades and across multiple species, and it has profound implications for both physiology and pharmacology.

One of the earliest demonstrations of intrinsic heterogeneity came from studies of transmural differences within the ventricular wall. Antzelevitch et al. [30] showed that epicardial, endocardial, and midmyocardial cells differ in AP morphology and pharmacological sensitivity, providing a cellular basis for regional dispersion of repolarization. Subsequent work in the atrium further established that ionic current expression varies even within a single chamber. For example, Feng et al. [31] identified regional differences in ionic mechanisms of canine right atrial APs, with heterogeneous contributions from repolarizing currents shaping local electrophysiological profiles. These experimental observations revealed that cell-to-cell differences are not merely noise but fundamental features of cardiac tissue organization.

More recently, computational and statistical approaches have been employed to systematically capture and explain such heterogeneity. Britton et al. [32] pioneered the use of experimentally calibrated "populations of models," showing that variation in ionic conductances can explain observed inter-subject variability in AP biomarkers. Sachse et al. [61] extended this approach to human atrial tissue, comparing sinus rhythm and atrial fibrillation, and demonstrated that differences in ionic properties across individuals help determine both normal and pathological electrophysiological states. In ventricular disease contexts, Passini et al. [63] used patient-specific modelling of hypertrophic cardiomyopathy to uncover how subtle conductance differences amplify susceptibility to pro-arrhythmic events. Similarly, Zhou et al. [64] combined in vivo recordings and in silico models of human ventricular cardiomyocytes to reveal mechanistic links between variability in repolarization dynamics and the emergence of alternans, a precursor to arrhythmia.

From a clinical perspective, such variability has significant consequences. Because pharmacological agents act on specific ionic targets, the heterogeneous distribution of conductances means that patients and even cells within the same heart—may respond differently to the same therapy. Niepel et al. [65] emphasized that non-genetic cell-to-cell variability challenges conventional pharmacological assumptions, as drug efficacy and toxicity can vary widely within a population. Building on this, Yang and Clancy [33] demonstrated, through in silico modelling, that sex-specific differences in ionic current expression alter susceptibility to ventricular tachyarrhythmias, highlighting

the importance of personalized modelling in predicting drug safety.

Taken together, these studies show that inter-cellular variability is not only experimentally observable but also mechanistically significant. It influences tissue-level electrical stability, shapes the response to therapeutic interventions, and contributes to individual risk profiles for arrhythmia. However, direct experimental quantification of the full spectrum of ionic conductance differences across large populations of cells remains infeasible. Consequently, mechanistic mathematical modelling has become essential for bridging the gap between experimental observation and clinical translation, offering a framework to explore how microscopic variability propagates to macroscopic outcomes in health and disease.

2.3.3 Strategies for the Modelling of Variability

The increasing recognition that cardiomyocyte electrophysiology exhibits significant variability has motivated a range of computational strategies to capture and explain this diversity. Recent reviews [35, 66] emphasize that variability should not be treated as noise but as an essential property of cardiac systems, shaping both normal physiology and pathological dynamics. Two principal modelling paradigms have emerged to address this challenge: population-based modelling and sample-specific modelling [35]. Both strategies begin with a well-established "baseline" cardiomyocyte AP model, chosen to represent the relevant species, tissue, or condition. Such baseline models have a long history, with decades of development leading to highly detailed mathematical formulations of ventricular myocyte function [67], as well as comprehensive reviews describing the evolution of cardiac electrophysiology modelling over the past 70 years [4].

Population-based approaches explore variability by creating large ensembles of model variants through random sampling of ionic conductances and kinetic parameters from prescribed distributions. In many studies, these populations are subsequently filtered or calibrated against experimental biomarkers to exclude implausible behaviours. For instance, Romero et al. [15] investigated how ionic current variability influences human ventricular electrophysiology, while Muszkiewicz et al. [68] employed experimentally constrained populations of models to capture inter-individual

variability and move beyond the "single virtual physiological human" paradigm. Similarly, Morotti and Grandi [69] applied statistical regression techniques to large model populations to assess pro-arrhythmic risk in a data-driven manner. The strength of population-based modelling lies in scalability: ensembles of 10^4 or more randomized models can be generated, enabling robust statistical analyses that exceed the capacity of experimental studies limited by practical sample sizes. Such simulations are particularly powerful for uncovering subtle patterns of variability and for quantifying population-level drug responses. However, their key limitation is the lack of a one-to-one correspondence between any given model in the ensemble and an actual biological cell. As a result, populations may reproduce some biomarker distributions while failing to generalize to others, thereby reducing predictive precision.

In contrast, sample-specific approaches aim to reconstruct the electrophysiological behaviour of individual cells by re-estimating the parameters of a baseline model directly from experimental data. Early work by Dokos and Lovell [36] laid the methodological foundation for parameter estimation in cardiac ionic models, while Syed et al. [70] demonstrated the use of genetic algorithms for fitting atrial APs. Later studies expanded these ideas across species and contexts: Bot et al. [71] applied genetic optimization to mouse cardiomyocytes, Groenendaal et al. [72] advanced the concept of cell-specific models with explicit tailoring of ionic conductances, and Krogh-Madsen et al. [73] improved fidelity through dynamic protocols coupled with optimization methods. Most recently, efficient parameter estimation was proposed in [74] for archetypal myocyte models, illustrating the continued refinement of this approach. The major advantage of sample-specific modelling is its one-to-one correspondence between real cells and in silico reconstructions, which allows for prediction of unmeasured quantities, quantification of cell internal states, and exploration of responses to untested stimuli. However, this fidelity comes at a cost: large, high quality datasets are required to constrain the models, and parameter optimization is computationally demanding. Consequently, applications have typically been limited to individual cells or small cohorts rather than large scale population studies.

Overall, both strategies offer complementary insights. Population-based models capture broad variability patterns and provide scalable tools for risk assessment,

but lack individualized mapping. Sample-specific models provide precision at the single-cell level but are resource intensive and limited in throughput. As emphasized in recent reviews [35, 66], bridging these paradigms by combining population wide scalability with individualized calibration represents a promising direction for future work, particularly as experimental high throughput datasets become increasingly available.

2.4 Drug Effects on Cardiac Ion Channels

Pharmacological modulation of cardiac ion channels is the primary mechanism through which drugs alter electrophysiological activity and influence rhythm stability. Many therapeutic agents and numerous non-cardiac compounds interact with specific ion channel subtypes, thereby changing the amplitude, kinetics, or voltage dependence of ionic currents that underlie the cardiac AP. Depending on the target and the nature of the interaction, such effects can be either beneficial, as in the suppression of arrhythmogenic activity, or detrimental, producing conduction slowing, repolarisation abnormalities, and potentially lethal arrhythmias such as torsade de pointes (TdP).

Traditionally, anti-arrhythmic drugs are classified by the Vaughan Williams scheme [75]. Class I agents inhibit the fast sodium current, reducing phase-0 depolarisation and slowing conduction. Class II compounds act through β-adrenergic receptor blockade, indirectly modulating calcium and potassium currents via cyclic-AMP signaling. Class III agents typified by dofetilide selectively block the rapid delayed rectifier potassium current, thereby prolonging the AP duration and refractory period. Class IV drugs suppress the L-type calcium current, decreasing plateau amplitude and contractile strength. While these classifications remain clinically useful, it is now recognized that most drugs exhibit some degree of multichannel pharmacology, and that the overall electrical outcome depends on the balance between inward and outward current blockade.

Our third project in 1.3 will mainly focus on the drug action of dofetilide on the blockade of rapid delayed rectifier current which mediated by the human Ether-à-go-go-Related Gene (hERG) encoding the Kv11.1 potassium channel. The hERG chan-

nel's distinctive gating kinetics, slow activation and rapid inactivation enable it to stabilize the repolarization process and prevent premature excitability [55]. Dofetilide is a highly selective Class III anti-arrhythmic agent that exerts its therapeutic effect almost exclusively through potent inhibition of the hERG channel, thereby prolonging the AP duration and effective refractory period in atrial and ventricular tissue. Clinically, dofetilide is used to restore and maintain sinus rhythm in patients with atrial fibrillation and flutter. Owing to its strong and selective blockade of rapid delayed rectifier current, it has also become a reference compound in the Comprehensive in vitro Proarrhythmia Assay (CiPA) initiative for validating in silico and in vitro models of drug-induced proarrhythmia [42, 54, 55]. Despite its clinical utility, dofetilide exhibits reverse use dependence and a narrow therapeutic window, making it prone to cause excessive QT prolongation and torsade de pointes in susceptible individuals [41]. While prior studies have clarified its electrophysiological profile, the detailed mechanisms of its channel-binding kinetics and dynamic modulation of repolarisation remain incompletely understood. These aspects will be investigated in greater depth in Chapter 6, where the mechanistic basis of dofetilide action will be examined using computational and experimental approaches.

Chapter 3

Mathematical Modelling and Analysis of Cardiac Electrophysiology

This chapter focuses on the derivation and formulation of mathematical models of cardiac electrophysiology at the cellular level, beginning with the description of ion channel currents. Fundamental transport equations are introduced, followed by simplified ionic flux formulations that are commonly employed in cardiac modelling and then mathematical representations of ion channel gating dynamics are discussed. Later in this chapter, the global sensitivity analysis and parameter estimation methods used to study the single cell models are outlined.

3.1 Introduction to Mathematical Modelling of Cardiac Electrophysiology

Mathematical descriptions of electrophysiology can broadly be divided into two classes. The first class consists of detailed models of cellular electrophysiology, commonly referred to as ion current models. These models explicitly represent changes in membrane permeability through individual ion channels located in the cell membrane and intracellular organelles, and are used to compute the resulting transmembrane poten-

tial. The second class comprises more abstract formulations, often termed membrane potential models, which provide a phenomenological description of electrical activity using systems of equations derived from dynamical systems theory.

Membrane potential models typically involve a small number of variables and equations, yet are capable of reproducing key qualitative features of excitable behaviour. A significant advantage of such models is that their reduced complexity permits analytical investigation, particularly through fast and slow decomposition techniques, as discussed in detail by Keener and Sneyd [60]. A well-known example is the FitzHugh-Nagumo model, proposed in 1961 [76] and it is shown to be possible to reproduce the most important characteristics of the AP with a simple two-variable model. Although these models have been successfully applied across a wide range of physical, chemical, and biological systems, they do not explicitly represent ionic mechanisms and are therefore not well suited for studies requiring the interactions with other electrophysiological cell types.

In contrast, ion current models provide a mechanistic representation of cellular electrical activity at the level of individual ion channels. While this increased physiological detail comes at a higher computational cost, such models are essential when the intracellular dynamics, intercellular coupling, or interactions with mechanical processes are of interest. The origins of ion current modelling lie outside cardiac electrophysiology. In 1952, Hodgkin and Huxley introduced the first quantitative description of ionic currents underlying AP generation, based on experiments conducted on the giant axon of the squid. The unusually large diameter of this axon enabled direct experimental manipulation using the technology available at the time. Their work led to the formulation of voltage dependent ion channels and the first mathematical description of channel gating dynamics [77]. These modelling techniques were subsequently adapted to cardiac tissue by Noble in the early 1960s, resulting in the first ion current model of Purkinje fibre electrophysiology [78]. Since then, numerous models have been developed for different cardiac cell types, species, and physiological conditions, including models of human atrial and ventricular myocytes, as well as human induced pluripotent stem cell-derived cardiomyocytes.

The work presented in this thesis makes use of a well-established ion current model

developed to describe rabbit ventricular cardiomyocytes in [3]. A convenient starting point for modelling cellular electrophysiology is to represent the cell membrane as a simple electrical circuit composed of two fundamental elements. The lipid bilayer of the membrane acts as a capacitor, storing electrical charge, while ion channels provide resistive pathways for ionic current flow. By applying Kirchhoff's current law to this circuit, the transmembrane current can be written as

$$C_m \frac{dV}{dt} = -I_{\text{ion}} + I_{\text{app}}, \tag{3.1}$$

where C_m denotes the membrane capacitance, V is the transmembrane potential, and I_{ion} represents the total ionic current flowing through membrane channels. I_{app} is an applied stimulus current, which is used to trigger the AP of the cell.

3.2 Ion Channel Currents

Ion channel currents arise from the transmembrane movement of charged ions through specialised protein channels embedded in the lipid bilayer of the cell membrane. These currents are driven by gradients in both ionic concentration and electrical potential and play a central role in shaping the cardiac AP.

From a modelling perspective, ion channel currents are expressed as functions of the transmembrane potential, ionic concentrations, and variables describing the state of channel gating. While the underlying biophysical mechanisms are complex, simplified mathematical representations are widely used to capture the dominant electrophysiological behaviour while remaining computationally tractable [60].

3.2.1 The Nernst Equilibrium Potential

In this section, we examine the transport of a single ionic species and derive an expression describing the equilibrium state in which the flux due to diffusion exactly balances the flux driven by an electrical field. We begin by considering the case in which no concentration gradients are present. Under this assumption, the ionic flux

generated by an electrical field is given by Planck's equation:

$$J_E = m\frac{z}{|z|}cE, \tag{3.2}$$

where m denotes the ionic mobility, z is the ionic charge, c is the concentration, and E represents the electric field. The electric field may be expressed as the negative gradient of the electric potential ϕ, which yields

$$J_E = -m\frac{z}{|z|}c\nabla\phi. \tag{3.3}$$

When spatial variations in ionic concentration are present, the electrically driven flux is accompanied by a diffusive contribution. Diffusion causes ions to move from regions of higher concentration to regions of lower concentration, and the associated flux is described by Fick's law,

$$J_D = -D\nabla c, \tag{3.4}$$

where D is the diffusion coefficient of the ion.

In physiological systems, differences in both electrical potential and ionic concentration exist across the cell membrane. Consequently, the total ionic flux is given by the sum of the electrically driven and diffusive components,

$$J = J_D + J_E. \tag{3.5}$$

The ionic mobility m is related to the diffusion coefficient D through the Einstein relation,

$$m = \frac{D|z|F}{RT}, \tag{3.6}$$

where R is the universal gas constant, T is the absolute temperature, and F is Faraday's constant. Substituting this expression into (3.3) and (3.5) yields

$$J = -D(\nabla c + \frac{zF}{RT}c\nabla\phi), \tag{3.7}$$

which is known as the Nernst-Planck equation.

We are interested in the equilibrium configuration, in which the net ionic flux vanishes, i.e. $J = 0$. Hence under the assumption of one-dimensional ionic transport across the membrane, integration of the Nernst–Planck equation in the equilibrium case leads directly to the Nernst equilibrium potential:

$$v_{\text{eq}} = \frac{RT}{zF} \ln\left(\frac{c_e}{c_i}\right), \tag{3.8}$$

where c_e and c_i denote the extracellular and intracellular concentrations, respectively. The potential v_{eq} is referred to as the Nernst equilibrium potential.

3.2.2 Models for Ionic Flux

Any mathematical representation of passive ionic transport must, at a minimum, satisfy the condition imposed by the Nernst equilibrium potential (3.8), namely that the net flux is zero when the membrane potential equals v_{eq}. The simplest formulation that meets this requirement is a linear flux model, given by

$$J = G(v - v_{\text{eq}}), \tag{3.9}$$

where G denotes the membrane permeability of the channel. Depending on the specific transport mechanism being modelled, G may be treated as a constant or as a function of time, membrane potential, and, in some cases, ionic concentrations.

To obtain ionic flux expressions of greater complexity, the Nernst–Planck equation must be integrated explicitly. Under the constant-field assumption, the potential gradient may be written as $\nabla\phi = v/L$, where L denotes the membrane thickness and equation (3.7) yields:

$$\frac{dc}{dx} - \frac{zFv}{RTL}c + \frac{J}{D} = 0. \tag{3.10}$$

This equation is a first-order ordinary differential equation for the concentration c, with boundary values prescribed at both sides of the membrane and the flux J appearing as an additional unknown.

Solving this equation gives the ionic flux as

$$J = \frac{D}{L}\frac{\frac{zFv}{RT}\left(c_i - c_e \exp\left(-\frac{zFv}{RT}\right)\right)}{1 - \exp\left(-\frac{zFv}{RT}\right)}, \tag{3.11}$$

This flux density J becomes an electrical current density when multiplied by zF, the amount of charge carried per mole, and thus

$$I = \frac{D}{L}\frac{\frac{z^2F^2v}{RT}\left(c_i - c_e \exp\left(-\frac{zFv}{RT}\right)\right)}{1 - \exp\left(-\frac{zFv}{RT}\right)}, \tag{3.12}$$

This is the famous Goldman– Hodgkin–Katz (GHK) current equation, and plays an essential role in models of cellular electrical activity.

3.2.3 Models of Channel Gating

Ion channels that respond to changes in the transmembrane potential are fundamental to the electrical activity of excitable cells. These channels are formed by large protein complexes embedded in the cell membrane, whose conformational changes regulate the flow of ions. In many electrophysiological models, ion channels are represented as assemblies of multiple subunits, each of which may exist in either an open or closed state. Assuming that each subunit operates independently, the probability that a channel composed of n identical subunits is open is given by

$$O = g^n. \tag{3.13}$$

More generally, channels may contain several distinct subunit types. For example, if a channel contains m subunits of type g and n subunits of type h, the probability that the channel is open is

$$O = g^m h^n. \tag{3.14}$$

The ionic current through the membrane is then computed as the product of the maximum conductance and the fraction of open channels. For a linear current

formulation, this yields

$$I = G_{\max} O(v - v_{\text{eq}}), \tag{3.15}$$

where $G_{\max}$ is the maximum conductance corresponding to all channels being open, and v_{eq} is the Nernst equilibrium potential for the ion.

3.2.4 The Hodgkin–Huxley Model

A classical framework for modelling these ion channel gates was introduced in Section 3.1 to describe AP generation in the squid giant axon [77]. The Hodgkin–Huxley model describes three ionic currents: a sodium current I_{Na}, a potassium current I_{K}, and a leakage current I_{L}. These are given by

$$I_{\text{Na}} = G_{\text{Na}} m^3 h (\nu - \nu_{\text{Na}}), \tag{3.16}$$

$$I_{\text{K}} = G_{\text{K}} n^4 (\nu - \nu_{\text{K}}), \tag{3.17}$$

$$I_{\text{L}} = G_{\text{L}} (\nu - \nu_{\text{L}}), \tag{3.18}$$

where $\nu = v - v_{\text{eq}}$ denotes the deviation from the resting potential, $G_{\text{Na}}, G_{\text{K}}, G_{\text{L}}$ are the maximal conductances for each current and ν_{Na}, ν_{K}, and ν_{L} are shifted equilibrium potentials. The variables m, h, and n are gating variables governed by equations of the form

$$\frac{dg}{dt} = \alpha_g(\nu)(1 - g) - \beta_g(\nu) g, \tag{3.19}$$

with voltage-dependent rate functions α_g and β_g.

The total ionic current is obtained by summing the individual contributions,

$$I_{\text{ion}} = I_{\text{Na}} + I_{\text{K}} + I_{\text{L}}, \tag{3.20}$$

and the transmembrane potential evolves according to equation 3.1

$$C_m \frac{d\nu}{dt} = -(I_{\text{Na}} + I_{\text{K}} + I_{\text{L}}) + I_{\text{app}}. \tag{3.21}$$

While the Hodgkin-Huxley model reproduces key features of neuronal APs, its parameterization is not suitable for cardiac electrophysiology because cardiomyocytes

involve a wider range of ion channels and complex intracellular calcium dynamics that are not represented in this original model. Nevertheless, the structure of the model and its gating formulations serve as fundamental building blocks for more detailed and physiologically accurate cardiac cell models.

3.2.5 Models of Cardiomyocytes

When modelling the electrical behaviour of the entire heart and its manifestation in ECG recordings, ventricular myocyte cells play a more significant role and a key distinction between Hodgkin-Huxley model and ventricular myocytes model lies in the role of calcium dynamics. Cardiac myocyte APs are governed by sodium, potassium, and calcium currents, each comprising several distinct ion channels. Existing cardiomyocyte models vary depending on cardiac region and species. Figure 3.1 shows an example of cardiomyocyte model, the ionic channel schematic of the rabbit ventricular myocyte AP model by Shannon [3], which will be utilised and discussed in all three projects.

The Shannon model provides a comprehensive description of ionic dynamics across four distinct intracellular and extracellular compartments: the sarcoplasmic reticulum, the junctional cleft, the subsarcolemmal space, and the bulk cytosol. The model tracks a total of 38 state variables, including ionic concentrations and channel gating variables, and incorporates 15 transmembrane ionic currents. These include the major depolarizing and repolarizing currents I_{Na}, I_{CaL}, I_{Kr}, I_{Ks}, and I_{K1}, as well as transient outward potassium currents (I_{tof} and I_{tos}), chloride currents (I_{ClCa} and I_{Clb}), and electrogenic transport mechanisms such as the sodium–calcium exchanger (I_{NaCa}), sodium–potassium pump (I_{NaK}), and sarcolemmal calcium pump (I_{Cap}). Additional background and pump currents (I_{Nab}, I_{Cab}, and I_{Kp}) are also included.

In total, the model comprises approximately 180 parameters, reflecting its detailed biophysical representation of ventricular electrophysiology. A more detailed description of the Shannon model, including the full system of governing ordinary differential equations, is provided in Section 4.2.1.

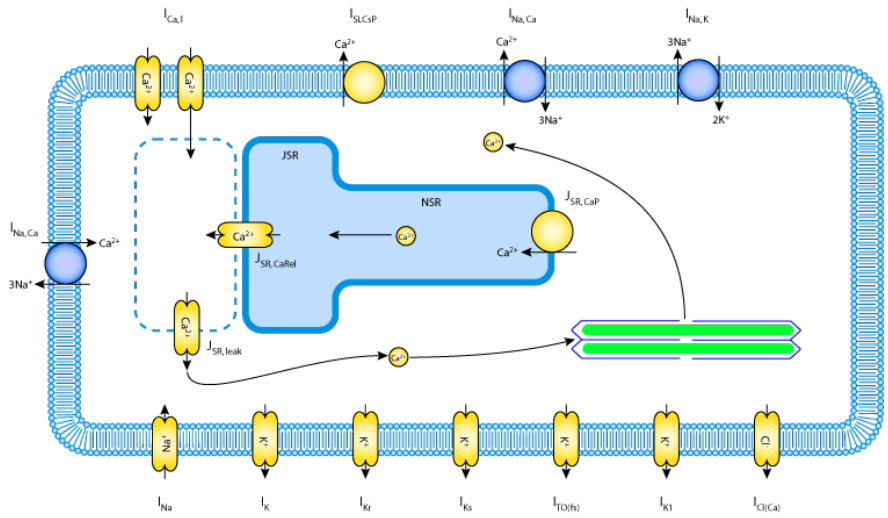

Figure 3.1: Schematic of the ionic channels in the Shannon model [3] for rabbit ventricular myocytes. Reproduced from the CellML repository [79]. This work is licensed under a Creative Commons Attribution 3.0 Unported License.

3.3 Global Sensitivity Analysis

In computational electrophysiology, mathematical models of cardiac myocytes describe the AP as an emergent property of numerous interacting ionic currents and transport mechanisms. While such models are mechanistically detailed, they often include a large number of parameters, many of which may exhibit biological variability or uncertainty. As a result, it becomes important to identify which parameters (e.g., ionic conductances) most strongly influence specific electrophysiological outputs, such as AP duration or resting membrane potential.

To systematically investigate the influence of these parameters, global sensitivity analysis (GSA) techniques can be employed. Unlike local sensitivity methods, which examine the effect of small perturbations around a fixed point, GSA explores the entire parameter space and accounts for interactions between parameters. This approach is particularly well suited for highly nonlinear and non-monotonic systems, such as those encountered in cardiac electrophysiology models.

In Project 1 described in Section 1.1 of this thesis, a GSA was applied to the Shannon model [3] of the rabbit ventricular myocyte to determine which ionic currents are the dominant contributors to AP output variability. Among available GSA techniques, the Sobol method developed in [80] was selected due to its ability to

decompose output variance into contributions from individual parameters and their higher-order interactions. The following subsection provides an overview of the Sobol sensitivity analysis method and its application to cardiac modelling.

3.3.1 Sobol Sensitivity Analysis

The Sobol method is a global, model-independent sensitivity analysis technique based on variance decomposition [29]. It is particularly suitable for nonlinear and non-monotonic models, where local derivative-based approaches may fail to capture complex parameter interactions. The primary objective of Sobol sensitivity analysis is to quantify the contribution of input parameters to the variability of a model output and to determine which parameters can be considered as "drivers" or "key factors" of system behaviour.

The essence of the Sobol method lies in decomposing the total variance of the model output into contributions arising from individual parameters and their interactions. This decomposition yields quantitative sensitivity indices, including the first-order index, which measures the direct effect of a parameter, and the total-order index, which accounts for both individual effects and higher-order interactions. Such variance-based measures provide a comprehensive assessment of parameter importance.

In cardiac electrophysiology modelling, Sobol sensitivity analysis has been widely applied to investigate how variability in ionic conductances and kinetic parameters influences AP biomarkers, such as AP duration, resting membrane potential, and upstroke velocity [12, 20, 22]. These studies have demonstrated that AP morphology is often governed by a subset of dominant ionic currents, while other parameters contribute primarily through interaction effects. Global sensitivity analysis has therefore become an important tool for identifying influential ionic mechanisms, guiding model reduction, and informing experimental design in AP modelling.

The practical implementation of the Sobol method can be summarized in the following six steps:

- Sampling: The method requires generating a set of input parameter combinations, often referred to as samples. These samples are drawn from the parameter

space according to a specific sampling scheme, such as Latin Hypercube Sampling or Monte Carlo Sampling. The number of samples should be sufficiently large to ensure good coverage of the parameter space.

- Model Evaluation: Each sample of input parameters is used to run the model and obtain the corresponding output values. The model is typically run multiple times to obtain a robust estimate of the output variance.

- Variance Decomposition: The next step involves decomposing the total variance of the model output into contributions from different factors. This decomposition is achieved through mathematical formulas based on the moments of the model output distribution.

- Calculation of Sensitivity Indices: The decomposed variances are used to calculate sensitivity indices, such as the first-order sensitivity index and second-order sensitivity index. These indices quantify the relative importance of individual parameters and their interactions in contributing to the output variance.

- Analysis and Interpretation: The calculated sensitivity indices are then analyzed and interpreted to assess the significance of each parameter and interaction. Parameters with high sensitivity indices indicate greater influence on the output, while low sensitivity indices suggest parameters with minimal impact.

- Ranking and Decision-Making: Based on the sensitivity indices, parameters can be ranked according to their importance. This ranking helps in decision-making processes, resource allocation, parameter prioritization, and further model refinement.

3.4 Parameter Estimation

Global sensitivity analysis not only provides insight into the relative importance of model parameters, but also plays a critical role in guiding subsequent parameter estimation. A common and effective strategy is to restrict parameter estimation to those parameters identified as most influential by sensitivity analysis, while fixing

less influential parameters at fixed values. Parameter estimation itself is a central and longstanding challenge in computational biology and electrophysiology. The objective is to determine parameter values that enable a mathematical model to reproduce experimentally observed behaviour, such as AP morphology, duration, and restitution properties. This task is often formulated as an inverse problem, in which parameters are inferred from observations of the model output [81]. In the context of cardiac myocyte models, this inverse problem is particularly challenging due to the strong nonlinearity of the governing equations, the presence of measurement noise, and the possibility of non-identifiability, whereby multiple parameter sets produce similar electrophysiological responses [82].

Parameter estimation problems of this form are typically solved using global optimisation techniques. Two common formulations are to identify parameter values that either minimise a predefined error or cost function, measuring the discrepancy between model predictions and experimental data, or maximise a likelihood function that quantifies the probability of observing the data given a particular parameter set. Both approaches are widely used in cardiac electrophysiology and lead to challenging optimisation problems due to the nonlinearity, non-convexity, and high dimensionality of detailed ionic current models.

In this thesis, parameter estimation is performed using derivative-free global optimisation methods. In Project 1.2, the Covariance Matrix Adaptation Evolution Strategy (CMA-ES) is employed to identify parameter values that maximise the likelihood function. CMA-ES, originally introduced by Hansen and Ostermeier [83], is an evolutionary optimisation algorithm designed for nonlinear, non-convex, and high-dimensional search spaces. The method proceeds by iteratively evolving generations of candidate solutions sampled from a multivariate Gaussian distribution. This distribution is characterised by a mean vector, representing the current best estimate of the optimal parameters, and a covariance matrix that is adaptively updated at each generation to capture correlations between parameters and improve search efficiency.

In Project 1.3, parameter estimation is performed using the Exponential Natural Evolution Strategy (xNES) designed by [84], which is particularly well suited for joint parameter estimation problems involving strong parameter interactions. xNES

belongs to the family of natural evolution strategies and performs optimisation by following the natural gradient of the expected fitness with respect to the parameters of the search distribution [84]. This approach provides improved stability and performance in complex, high-dimensional optimisation problems when gradient information is unavailable or unreliable.

Both CMA-ES and xNES are implemented using the Python package `PINTS` (Probabilistic Inference on Noisy Time-Series), developed by Clerx et al. [85]. `PINTS` is a computational framework for optimisation and Bayesian inference in ordinary differential equation models driven by noisy time-series data, such as those encountered in electrochemistry and cardiac electrophysiology. The package provides a wide range of derivative-free optimisation algorithms, along with predefined error measures for optimisation and likelihood functions for maximum-likelihood and Bayesian inference.

In addition to optimisation-based parameter estimation, `PINTS` supports several sampling-based inference methods, including adaptive Markov chain Monte Carlo and nested sampling techniques, enabling the estimation of full parameter distributions and uncertainty quantification, which will be also be used in Section 5.3.2. This flexibility makes `PINTS` particularly well suited for the analysis of complex electrophysiological models.

Chapter 4

Dominant Ionic Currents in Rabbit Ventricular Action Potential Dynamics

In this chapter, I explored the complexity of a mathematical model used to understand the electrical activity of rabbit ventricular cells. Such models involve many parameters, which makes it difficult to match them with experimental data or to personalize them for individual cells. To address this, I used a method for global sensitivity analysis introduced in Section 3.3.1 to identify which ion current parameters have the most impact on the AP output of the model. Our analysis shows that the background chloride current is the main factor influencing the variability of the rabbit ventricular action potential. Other important currents include the inward rectifier potassium current, various potassium currents, sodium-calcium exchanger current, the slow component of the transient outward potassium current, and the L-type calcium current. These factors play a significant role in determining key features of the action potential, such as its duration, plateau potential, and resting potential. Based on these results, I proposed a sequence simplified models obtained by retaining variability in a few most influential parameters while fixing the rest to appropriate constant values. This approach is also applicable to other mathematical models of cardiac action potentials and can make them more useful for personalized simulations,

and in areas like digital twins and predicting drug responses in biomedical research.

4.1 Introduction

Mathematical models of ventricular APs incorporate a large number of ionic currents and parameters in order to capture the complexity of cardiac electrophysiology. While this level of detail enables biophysically realistic simulations, it also introduces challenges related to model interpretability, parameter identifiability, and computational cost. In particular, not all ionic currents contribute equally to shaping AP morphology and derived electrophysiological biomarkers. Identifying the dominant contributors is therefore a crucial step toward model reduction, efficient parameter estimation, and mechanistic interpretation of experimental data.

Building on the motivation outlined in Section 1.1, this chapter presents a systematic global sensitivity analysis of the Shannon model of rabbit ventricular myocytes. The primary objective is to quantify the relative importance of maximal ionic conductances in determining key AP characteristics, including AP duration, plateau potential, and resting membrane potential. Unlike local sensitivity approaches that probe parameter effects only in the vicinity of a baseline model, a variance-based global method is employed to capture nonlinear effects and parameter interactions across a broad physiologically relevant parameter space.

Using Sobol sensitivity indices, ionic currents are ranked according to their contribution to output variance, allowing the identification of a small subset of dominant conductances. These rankings are subsequently used to construct a hierarchy of reduced models, demonstrating that substantial dimensionality reduction can be achieved while preserving predictive accuracy for key electrophysiological biomarkers. The results presented in this chapter establish a principled foundation for parameter selection in later chapters, particularly for the cell-specific model calibration and drug-response prediction studies developed in this thesis. The work presented in this chapter is published in [1]:

Yang Z, Gao H, Smith GL, Simitev RD. (2025) Dominant ionic currents in rabbit ventricular action potential dynamics. PLoS One 20(7): e0328261. doi.org/10.1371/

journal.pone.0328261.

4.2 Method and Model

4.2.1 Shannon's AP Model and Output Biomarkers

To understand the cell-to-cell variability reported in [6], I consider the Shannon model [3] introduced in Section 3.2.5, a mathematical model for the rabbit ventricular myocyte AP. This model, along with that of [19], is among the two widely used models for this cell type. I chose the Shannon model as it better captures the measurements of [6], as detailed in their analysis. As typical for models of myocyte electrophysiology, the Shannon model takes the form of a system of ordinary differential equations

$$\begin{aligned}
\frac{d}{dt}V(t) &= -\left(\sum_{i=1}^{N}\alpha_i I_i(V,\mathbf{z},\mathbf{c},\boldsymbol{\theta}) + I_{\text{stim}}\,(t,\mathbf{u})\right),\\
\frac{d}{dt}\mathbf{z}(t) &= \mathbf{g}(V,\mathbf{z},\boldsymbol{\theta}),\\
\frac{d}{dt}c_k(t) &= s_k\left(\sum_{j_k}\alpha_{j_k} I_{j_k}(V,\mathbf{z},\mathbf{c},\boldsymbol{\theta})\right), \qquad j_k \subseteq \{x\in\mathbb{N}\mid 1\le x\le N\}.
\end{aligned} \tag{4.1}$$

Here, V is the electric potential across the cell membrane, t represents time. Vector $\mathbf{z}$ represents variables describing channel gating configurations such as activation and inactivation or Markov model states, and vector $\mathbf{c}$, with components c_k, represents ionic intracellular concentrations, while $\mathbf{g}$ and s_k are functional dependences. Model parameters, such as maximal conductances and channel kinetics, are contained in the vector $\boldsymbol{\theta}$, while $\mathbf{u}$ represents external protocol parameters, including stimulus timing, duration, and strength. The transient changes in membrane potential, known as APs, are controlled by the sum of currents I_i flowing across the membrane or between internal compartments (e.g., organelles). The Shannon model includes $N = 15$ distinct currents, detailed in Table 4.1. Their explicit formulations and parameter values are available in [3]. The factors α_i multiply the ionic currents everywhere the latter appear, and represent increase or decrease of current strengths relative to their baseline values. They have been embedded in the model for the purposes of the sensitivity analysis, as they allow the original model formulation to be used without

Ionic current, I_i	Description
I_{CaL}	L-type Ca^{2+} current.
I_{Cab}	Background Ca^{2+} current.
I_{Cap}	Ca^{2+} pump current.
I_{ClCa}	Ca^{2+}-activated Cl^- current.
I_{K1}	Inward rectifier K^+ current / Time-independent K^+ current.
I_{Kp}	Background potassium K^+ current.
I_{Kr}	Fast delayed rectifier K^+ current.
I_{Ks}	Slow delayed rectifier K^+ current.
I_{Clb}	Cl^- background current.
I_{Na}	Fast Na current.
I_{NaCa}	Na^+/Ca^{2+} exchanger current.
I_{NaK}	Na-K pump current.
I_{Nab}	Background Na^+ current.
I_{tof}	Fast component of the transient outward potassium current.
I_{tos}	Slow component of the transient outward potassium current.

Table 4.1: The fifteen ionic currents of the Shannon [3] mathematical model for the rabbit ventricular myocyte AP.

modification. A stimulus current, I_{stim}, is used to excite the cell and is applied at a basic cycle length (t_{BCL}). Under physiological pacing conditions, the system reaches a periodic train of APs irrespective of the initial conditions.

The model equations are solved numerically. To avoid coding errors, I use a machine readable model specification file available from the CellML model repository [86]. Numerical integration is done using the Myokit suite for cardiac cellular electrophysiology simulations [87], which in turn employs solvers for nonlinear differential/algebraic equation from the SUNDIALS library [88].

Due to the large number of parameters in the Shannon model, it is not computationally feasible to include all in a sensitivity analysis. Following previous studies e.g. [6, 18], I restrict the attention to investigating the influence of the relative strengths of ionic currents. To measure these I introduce $N = 15$ auxiliary parameters denoted by α_i in equations (4.1). These can be interpreted as scaling factors of the maximal conductances for currents of the Ohmic form, or of the max I_i for currents of the Goldman-Hodgkin-Katz form. In essence, the factors α_i represent the relative strengths of ionic currents compared to their "baseline" values published in

[3].

The influence of the sensitivity parameters α_i on the model will be assessed by measuring the variation of $K = 6$ biomarkers y_i that capture important characteristics of the AP waveform $V(t; \alpha_1, \alpha_2, \ldots, \alpha_N)$. These model output quantities are listed and defined in Table 4.2. In the Table and throughout the rest of the text t_0 and t_{BCL} refer to the start and the end of the last AP, and $V(t)$ refers to its voltage trace. In summary, the relationships between biomarkers and parameters can be represented formally by a mapping $\mathbf{f}$ as

$$\mathbf{y} = \mathbf{f}(\boldsymbol{\alpha}), \qquad \boldsymbol{\alpha} = (\alpha_1, \alpha_2, \ldots, \alpha_N). \tag{4.2}$$

4.2.2 Sobol's Sensitivity Analysis of Variance Decomposition

I employ a global method for sensitivity analysis based on variance decomposition, originally proposed by [80]. The starting point is the relationship (4.2) between AP output biomarkers $\mathbf{y}$ and the relative strengths of ionic currents $\boldsymbol{\alpha}$. The sensitivity of each biomarker y^k can be analyzed independently of the others. For simplicity, I drop the superscript k and focus on a single scalar model output, $y = f(\boldsymbol{\alpha})$. To ensure that biomarker values are comparable in magnitude, the values are then normalized $\tilde{y} = \tilde{f}(\alpha)$ by computing their standard z-score $\tilde{f}(\boldsymbol{\alpha}) = z(f(\boldsymbol{\alpha}))$, defined as $z(x_i) = (x_i - \mu)/\sigma$ for a general set of values $\{x_i,\ i = 1, \ldots, L\}$ with mean and standard deviation μ and σ, respectively.

Consider the parameter vector as a vector of $N = 15$ independent random variables, $\boldsymbol{\alpha} = (\alpha_1, \alpha_2, \ldots, \alpha_N)$. The standardized biomarker $\tilde{Y}$ is then also a random variable, given by $\tilde{Y} = \tilde{f}(\boldsymbol{\alpha}) = f(\alpha_1, \alpha_2, \ldots, \alpha_N)$, where f is a deterministic function specified in Table 4.2 and consequently so is $\tilde{f}$. It can be shown that any function of independent random variables has a functional decomposition of the form

$$\tilde{f}(\boldsymbol{\alpha}) = \tilde{f}_0 + \sum_{i=1}^{N} \tilde{f}_i(\alpha_i) + \sum_{1 \le i < j \le N} \tilde{f}_{ij}(\alpha_i, \alpha_j) + \cdots + \tilde{f}_{1,2,\ldots,N}(\alpha_1, \alpha_2, \ldots, \alpha_N), \tag{4.3a}$$

AP/$[Ca^{2+}]_i$ biomarker	Symb y^k	Definition (Description)
Peak potential	$V_{\max}$	$V_{\max} = \max_t V(t)$.
Resting potential (alt. maximal diastolic potential)	V_{rest}	$V_{\text{rest}} = V(t_{\text{BCL}})$, where t_{BCL} is the "basic cycle length".
AP duration at 90% repolarization	A_{90}	$A_{90} = V^{-1}\big(V_{\max} - 0.9\lvert V_{\max} - V_{\text{rest}}\rvert\big) - t_0$ (The time from stimulus to the moment where the potential reaches 90% of full repolarization as defined by the difference between peak and resting potential.)
AP duration at 30% repol.	A_{30}	Ditto.
Plateau potential	V_{plt}	$V_{\text{plt}} = V(t_0 + A_{90}/2)$.
Bulk	B	$B = \int_0^{t_{\text{BCL}}} \lvert V(t) - V_{\text{rest}}\rvert \, dt$.
$[Ca^{2+}]_i$ at the end of diastole	ED	$\text{ED} = [Ca^{2+}]_i(t_{\text{BCL}})$.
Peak systolic value of $[Ca^{2+}]_i$	PSV	$\text{PSV} = \max_t [Ca^{2+}]_i(t)$.
Time from stimulus to peak $[Ca^{2+}]_i$	T_{peak}	$T_{\text{peak}} = [Ca^{2+}]_i^{-1}\big(\text{PSV}\big)$-$t_0$.
Period of time when $[Ca^{2+}]_i$ remains elevated above a threshold of 50% recovery from the peak value to the resting value, informally duration at 50% amplitude	D_{50}	$D_{50} = [Ca^{2+}]_i^{-1}\big(\text{PSV} - 0.5\lvert\text{PSV} - \text{ED}\rvert\big) - t_0$.

Table 4.2: A list of the six AP output biomarkers y^k used for sensitivity analysis, as well as four intracellular calcium biomarkers and definitions of their corresponding relationships to the parameters of the Shannon model, $y^k = f^k(\alpha_1, \alpha_2, \ldots, \alpha_N)$. The dependence of y^k on parameters is due to the voltage potential being parameter dependent, $V = V(t; \alpha_1, \alpha_2, \ldots, \alpha_N)$, as discussed in the text.

where the quantities $\tilde{f}_I(\alpha_I)$ are defined as:

$$\tilde{f}_I(\alpha_I) = \mathbb{E}[\tilde{f}(\boldsymbol{\alpha}) \mid \alpha_I] - \sum_{J \subset I} \tilde{f}_J(\alpha_J), \tag{4.3b}$$

for any subset of indices $I \subseteq \{1, 2, \ldots, N\}$, and $\mathbb{E}[\cdot]$ is the expectation value operator. These quantities represent the interaction "effects" on the output $\tilde{Y}$ of all variables indexed by the set I, where the sum is taken over all proper subsets J of I. For

example,

$$\tilde{f}_0 = \mathbb{E}[\tilde{f}(\boldsymbol{\alpha})],$$
$$\tilde{f}_i(\alpha_i) = \mathbb{E}[\tilde{f}(\boldsymbol{\alpha}) \mid \alpha_i] - \tilde{f}_0,$$
$$\tilde{f}_{ij}(\alpha_i, \alpha_j) = \mathbb{E}[\tilde{f}(\boldsymbol{\alpha}) \mid \alpha_i, \alpha_j] - \tilde{f}_i(\alpha_i) - \tilde{f}_j(\alpha_j) - \tilde{f}_0,$$

represent the overall mean value of the output, the correction effects due to the isolated "action" of each single parameter (first-order effects), and the correction effects due to the interactions of all possible combinations of two parameters (second-order interaction effects), respectively. The decomposition (4.3a) can be easily verified by nested back-substituting (4.3b) into (4.3a), and taking into account the fact that the conditional expectation of a deterministic function in the case all of its values are deterministic is equal to the value of the function itself, formally

$$\mathbb{E}[\tilde{f}(\alpha_1, \alpha_2, \ldots, \alpha_N) \mid \alpha_1 = \alpha_1, \alpha_2 = \alpha_2, \ldots, \alpha_N = \alpha_N] = \tilde{f}(\alpha_1, \alpha_2, \ldots \alpha_N).$$

The standard measure of the variation of the biomarker $\tilde{Y}$ is the variance $\mathbb{V}[\tilde{f}(\boldsymbol{\alpha})]$. Substituting the functional decomposition (4.3) into the definition of variance:

$$\mathbb{V}[\tilde{f}(\boldsymbol{\alpha})] = \mathbb{E}[(\tilde{f}(\boldsymbol{\alpha}) - \mathbb{E}[\tilde{f}(\boldsymbol{\alpha})])^2],$$

expanding the products, and using the fact that cross terms are orthogonal

$$\mathbb{E}[\tilde{f}_I(\alpha_I)\tilde{f}_J(\alpha_J)] = 0 \quad \text{for} \quad I \neq J, \qquad I, J \subseteq \{1, 2, \ldots, N\},$$

along with the property

$$\mathbb{V}[\tilde{f}_I(\alpha_I)] = \mathbb{E}[\tilde{f}_I(\alpha_I)^2],$$

I find that the total variance has the decomposition:

$$\mathbb{V}[\tilde{f}(\boldsymbol{\alpha})] = \sum_{i=1}^{N} \mathbb{V}[\tilde{f}_i(\alpha_i)] + \sum_{1 \leq i < j \leq N} \mathbb{V}[\tilde{f}_{ij}(\alpha_i, \alpha_j)] + \cdots + \mathbb{V}[\tilde{f}_{1,2,\ldots,N}(\alpha_1, \alpha_2, \ldots, \alpha_N)]. \tag{4.4}$$

With this, direct measures of the "main effect" of a given parameter α_i, and the "higher-order effects" of interactions between combinations of parameters on the output $\tilde{Y}$ are defined as the corresponding "partial" variances in the decomposition (4.4) normalised by the total variance,

$$S_i = \frac{\mathbb{V}[\tilde{f}_i(\alpha_i)]}{\mathbb{V}[\tilde{f}(\boldsymbol{\alpha})]}, \quad S_{ij} = \frac{\mathbb{V}[\tilde{f}_{ij}(\alpha_i, \alpha_j)]}{\mathbb{V}[\tilde{f}(\boldsymbol{\alpha})]}, \quad S_I = \frac{\mathbb{V}[\tilde{f}_I(\alpha_I)]}{\mathbb{V}[\tilde{f}(\boldsymbol{\alpha})]}. \tag{4.5a}$$

These quantities are known as first-order, second-order and higher-order Sobol sensitivity indices, respectively, and represent fractional sensitivities in the sense that they add up to unity,

$$1 = \sum_{i=1}^{N} S_i + \sum_{1 \le i < j \le N} S_{ij} + \cdots + S_{1,2,\ldots,N}.$$

Finally, the "total effect" of a parameter α_i is quantified by the so called Sobol total-effect index, defined as the sum of all sensitivity indices related to this parameter and its possible interactions,

$$S_{T_i} = S_i + \sum_{j \neq i} S_{ij} + \sum_{\substack{j \neq i, k \neq i \\ j < k}} S_{ijk} + \cdots + S_{1,2,\ldots,N}. \tag{4.5b}$$

The Sobol sensitivity indices (4.5) are estimated via quasi-random sampling. To achieve this, the parameter space is sampled using a quasi-Monte Carlo method, which generates the so-called "Sobol sequences" – sequences of low-discrepancy quasi-random numbers designed to fill space uniformly [80]. The values of the function $\tilde{f}$ and the terms of its functional decomposition (4.3) are evaluated at these sequences. Finally, the "Jansen" estimator [89] is used to calculate the Sobol sensitivity indices from the sampled data. The Sobol indices reported in this chapter are critically on the choice of base distribution over the parameter space. The expectations and variances appearing above are therefore taken with respect to a specific base distribution. Consequently, the resulting sensitivity indices should be interpreted as measures of parameter importance under the chosen sampling distribution, and may differ if an alternative distribution is adopted. For this study, I employ an implementation of

this procedure available from the SALib Sensitivity Analysis Library in Python [90]. Further technical details are omitted here, except to note that the consistency and bias of index estimation depend on the number M of randomly sampled points in the parameter space. This dependence is investigated further below.

Sobol index estimates are random values drawn from a sampling distribution. To assess their uncertainty, bootstrapping is used [91]. The original sample is resampled with replacement 1000 times, generating bootstrap samples from which Sobol indices are recalculated. This process constructs empirical sampling distributions, providing 95% confidence intervals for the indices and assessing variability due to finite sample size M. Bootstrapping is preferred over repeated Monte Carlo estimations, which are computationally more expensive.

4.2.3 Parameter Ranking and Dimensionality Reduction

Sensitivity studies lead to a rank of sensitivity parameters in descending order of their influence on the model output. The ranking can be further exploited to reduce the dimensionality of the parameter space of the problem.

A number of different criteria for parameter ranking may be employed. In this section I define a "grand" total Sobol sensitivity index for each of the sensitivity parameters α_i, as

$$S_{Gi} = \sum_{k=1}^{K} w_k S_{Ti}^k. \tag{4.5c}$$

Here S_{Ti}^k is the total Sobol index given by equation (4.5b) which measures the overall influence of the parameter α_i on a single AP biomarker y^k. In contrast the grand total index S_{Gi} measures the overall influence of the parameter α_i on all AP biomarkers $\mathbf{y}$. The weights w_k can be used to tune the importance of the outputs from any a priori considerations; here I take $w_k = 1, k = 1, \ldots, K$ as I consider all biomarkers to be of equal interest. The sensitivity parameters can then be ranked in descending influence by sorting the values of their grand total Sobol sensitivity indices. In the following, I denote parameter vectors where the components are ordered in decreasing grand

total Sobol index by angular brackets

$$\langle \boldsymbol{\alpha} \rangle = \langle \alpha_1, \alpha_2, \ldots, \alpha_N \rangle, \qquad S_{G1} \geq S_{G2} \geq \ldots \geq S_{GN}, \tag{4.6}$$

and distinguish it from parameter vectors $\boldsymbol{\alpha}$ where the order of components is immaterial.

If parameters are independent, the dimensionality of the parameter space can be reduced by keeping the values of a subset of $N - M$ parameters ($M \in [0, N]$) fixed to "hard-coded" constants. The natural choice is to fix the parameters with smallest grand total Sobol sensitivity indices as their influences on the model output are relatively less significant. Whether this is an acceptable approximation can be measured at any fixed point in the parameter space by the relative difference/error

$$e^{\langle M \rangle} = \frac{1}{K} \sum_{k=1}^{K} \left| \frac{(y_j^{\langle M \rangle, k} - y_j^k)}{y_j^k} \right|, \tag{4.7a}$$

between the output vectors of the reduced and the "full" models given by

$$\mathbf{y}^{\langle M \rangle} = \mathbf{f}(\langle \alpha_1, \alpha_2, \ldots \alpha_M, 1, \ldots, 1 \rangle), \tag{4.7b}$$

$$\mathbf{y} = \mathbf{f}(\langle \alpha_1, \alpha_2, \ldots \alpha_M, \alpha_{M+1}, \ldots, \alpha_N \rangle), \tag{4.7c}$$

respectively.

To obtain a global measure of the discrepancy over the entire parameter space I use quasi random Monte-Carlo sampling (similarly to assessing variability in section 4.2.2), and compute the mean relative error from the generated samples of parameter vector values

$$E^{\langle M \rangle} = \frac{1}{LK} \sum_{j=1}^{L} \sum_{k=1}^{K} \left| \frac{(y_j^{\langle M \rangle, k} - y_j^k)}{y_j^k} \right|, \tag{4.8}$$

where $L = 2000$ is the number of samples. This has the advantage over a mean squared error or over a Euclidian norm that it can be interpreted directly as the relative average discrepancy between full and reduced models. When $E = 0$ agreement is perfect. Using the relative error has the further advantage of non-dimensionalising

the errors of individual components which are otherwise measured in different units and may have significantly different magnitudes.

4.3 Results and Discussion: Sensitivity Analysis of Shannon model

In the following I present and discuss the results of applying the Sobol sensitivity analysis for a standard setup where the the stimulus amplitude was set to 9.5 A/F and trains of 1000 APs were generated with $t_{\mathrm{BCL}} = 500\,\mathrm{ms}$. Biomarkers were measured in the final AP from each train. Sample sequences of such measurements with size $M = 8192$ were used to then evaluate the sensitivity indices. I investigated the effects of varying these standard setup choices, and found that the results and conclusions do not differ significantly. As an illustration, the percentage differences in biomarker values from their respective values measured at the 2000th beat are plotted in Figure 4.1 as a function of the length of the train, and show that trains of 1000 APs are sufficiently long to reach the steady state in the simulations even though rare random fluctuations smaller than 2% may occur occasionally due to accumulation of numerical error. To further assess the robustness of the numerical results, additional simulations were performed using a stricter CVODE absolute tolerance of (10^{-11}), compared with the standard value of (10^{-6}) used throughout this chapter. Figure 4.1 shows that the stricter tolerance reduces the amplitude of the small residual oscillations visible in some biomarkers during long pacing trains. This suggests that these fluctuations are primarily caused by accumulated numerical error rather than by intrinsic oscillatory dynamics of the model. Importantly, the overall convergence behaviour and the steady-state biomarker values remain qualitatively unchanged. The sensitivity analysis and the associated conclusions are therefore not sensitive to the solver tolerance choice within this range. Consequently, the standard tolerance value of (10^{-6}) was retained throughout this work as a suitable compromise between numerical accuracy and computational efficiency. The other standard setup choices are also justified further below.

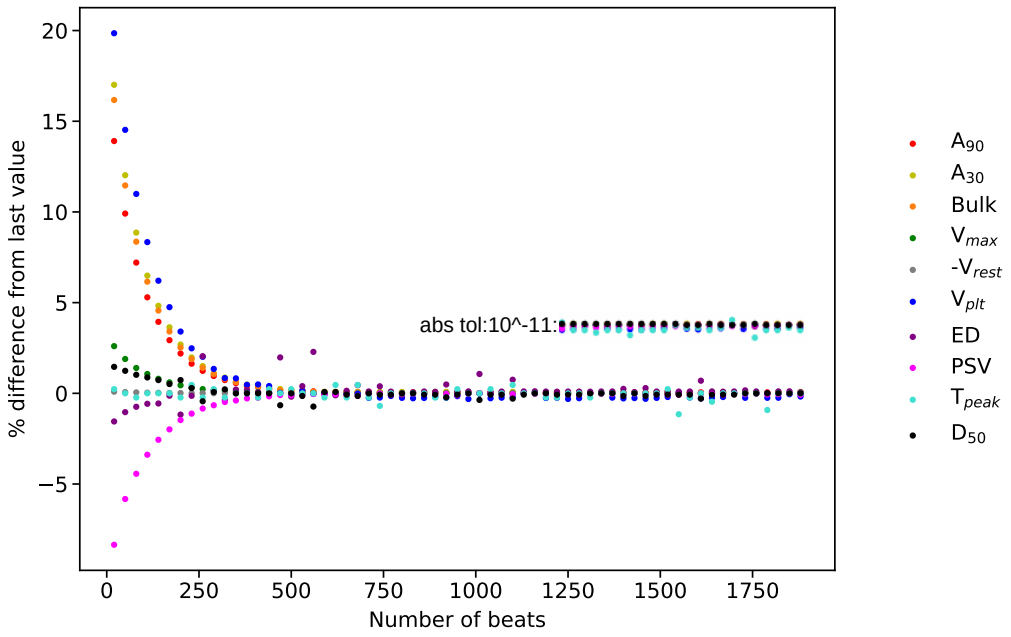

Figure 4.1: Biomarkers as a function of the length of AP train. The percentage differences in biomarker values from their respective values measured in the 2000th AP are plotted for increasing number of pre-pacing beats. The simulations are performed at 50% block of I_{NaK} and 70% block of I_{NaCa} and all other parameters at baseline values. Biomarkers are specified in the figure legend. Results obtained using the standard CVODE absolute tolerance of (10^{-6}), employed throughout this chapter, are shown over the full pacing interval, while the results obtained using a stricter tolerance of (10^{-11}) are overlaid for beats greater than 1250 for comparison.

4.3.1 The Parameter Range of Normal Response

To fulfill their physiological functions, biological cells exhibit a variety of complex behaviors under different conditions. Similarly, mathematical models of the AP, such as the Shannon model (4.1), have qualitatively distinct solutions across their parameter space due to their non-linear nature [92]. The simplest response to periodic stimulation $I_{\mathrm{stim}}(t)$ is a rapid return to a stable equilibrium (resting state), known as a 1:0 response, which mimics non-excitable cells. At other parameter values, a bifurcation to a periodic solution occurs, where each stimulus elicits a single AP, producing a 1:1 response that models normal physiological behaviour. Secondary bifurcations from the 1:1 response can result in a 2:1 response, where one stimulus generates an AP while the next does not, or a 2:2 response, where alternating stimuli produce long and short APs in a stable 2-periodic pattern. This 2:2 response, known as alternans, is thought to reflect early signs of instability. Further tertiary instabilities can lead to chaotic regimes, representing abnormal electrophysiological behavior, which may culminate in fibrillation. The review article of [92] discusses nonlinear and stochastic dynamics in the heart.

Naturally, sensitivity to parameters is expected to vary significantly across different solution regimes. I restrict our sensitivity analysis of the Shannon model to the parameter region corresponding to the normal 1:1-response, as this represents the most common physiological behavior. To perform this analysis, it is first necessary to identify the region in the parameter space where the primary normal response occurs. This region, occasionally called a "Busse balloon" in the context of pattern-forming dynamical systems [93], is not the primary focus of this study. Instead, our goal is to identify a sufficiently large region of normal response suitable for sensitivity analysis. To achieve this, I begin with the baseline Shannon model, where $\{\alpha_i = 1\}_{i=1}^{N}$, as the baseline model is calibrated to produce a normal response. Each sensitivity parameter α_i is then varied independently within the range 10^{-4} to 10, until the first transition to a secondary instability or a non-excitable state is observed.

Figure 4.2 illustrates the procedure for the parameter α_{NaK}. One biomarker, the AP duration at 90% repolarization (A_{90}), is used to assess the model's response, as other biomarkers exhibit similar behavior. At $\alpha_{\text{NaK}} = 1$, a normal 1:1-response is recorded, as shown in Figure 4.2(d). As a side note: Figure 4.2(d) which also depicts a typical AP profile in this model. The normal response persists for α_{NaK} in the range $[10^{-4}, 1.07]$. Beyond $\alpha_{\text{NaK}} = 1.07$, an intermittent response emerges, where approximately 20 normal APs are followed by an equally long equilibrium phase, as illustrated in Figure 4.2(e). This behavior produces a two-valued curve in the $(\alpha_{\text{NaK}}, A_{90})$ plane, with $A_{90} \approx 0$ during equilibrium and finite values during the normal response sequence. For $\alpha_{\text{NaK}} > 2.1$, only the equilibrium response is observed, as shown in Figure 4.2(f). Table 4.3 summarizes these findings and defines the parameter subspace for the normal response region analyzed in this section. Approximately 0.8% of sampled parameter sets produced APs outside the desired 1:1 normal response region. To retain coverage of the parameter space while ensuring physiological behaviour, these parameter sets were adjusted using a small local perturbation of up to $\pm 4\%$ of their current parameter values until a normal 1:1 response was reproduced. Since only a small proportion of samples required modification and the perturbation range was narrow, the overall sampling distribution remained effectively unchanged while allowing all simulations to produce physiologically valid responses.

Parameter	Range	Parameter	Range	Parameter	Range
α_{NaK}	[0.0001, 1.07]	α_{Kr}	[0.0001, 3.2]	α_{tos}	[0.0001, 2.5]
α_{K1}	[0.03, 1.01]	α_{NaCa}	[0.6, 3]	α_{Clb}	[0.0001, 10]
α_{CaL}	[0.7, 1.6]	α_{Ks}	[0.0001, 10]	α_{Cab}	[0.34, 10]
α_{Cap}	[0.0001, 4.5]	α_{ClCa}	[0.0001, 10]	α_{Kp}	[0.0001, 10]
α_{Na}	[1, 10]	α_{Nab}	[0.0001, 10]	α_{tof}	[0.0001, 4]

Table 4.3: Parameter subspace of normal response. Sensitivity analysis is performed within this range of parameter values.

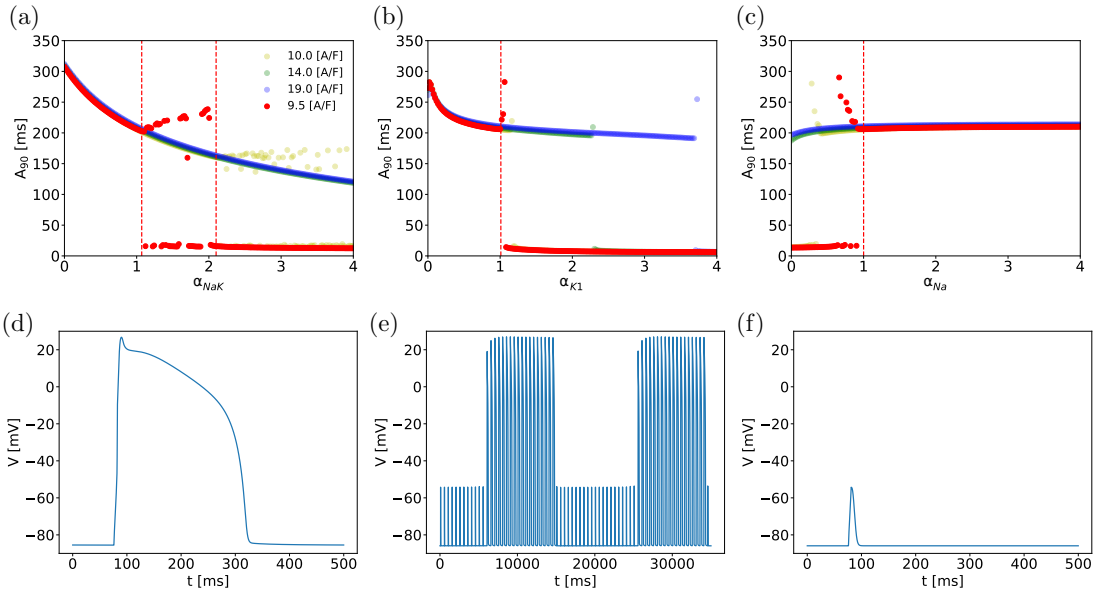

Figure 4.2: (Top row) Ranges of parameter values for normal response illustrated on a selection of parameters and for various stimulus amplitudes. Values of A_{90} as functions of α_{NaK}, α_{K1} and α_{Na} in (a), (b) and (c), respectively, and for four stimulus amplitudes as listed in the legend. The red dashed lines outline regime boundaries (for amplitude 9.5 A/F) as discussed in the text. (Bottom row) Types of response to stimuli observed for various values of the maximal density of the sodium-potassium pump current α_{NaK} for amplitude 9.5 A/F. (d): Normal response where each stimulus elicits a single 1:1 AP is observed for $\alpha_{\text{NaK}} < 1.07$; (e): An "intermittent" excitation pattern where Q successive stimuli elicit Q normal APs, while the next Q stimuli do not, observed for $\alpha_{\text{NaK}} \in (1.07, 2.1)$ (f): Stimuli do not elicit an AP response for $\alpha_{\text{NaK}} > 2.1$.

The threshold of excitation at baseline parameter values is approximately 9.4 A/F, so our standard setup uses a slightly supercritical stimulus amplitude. Increasing the amplitude of the stimulus current enlarges the region of normal response as shown in Figure 4.2(a,b,c) where results for amplitudes up to 2 times the threshold are also included. However, increasing the stimulus amplitude does not significantly alter the sensitivity ranking of parameters as will be shown further below.

4.3.2 Consistency and Bias of Sobol's Index Estimators

The Sobol sensitivity indices, as statistical estimators derived from random samples (Section 4.2.2), must exhibit key properties of good estimators, such as consistency

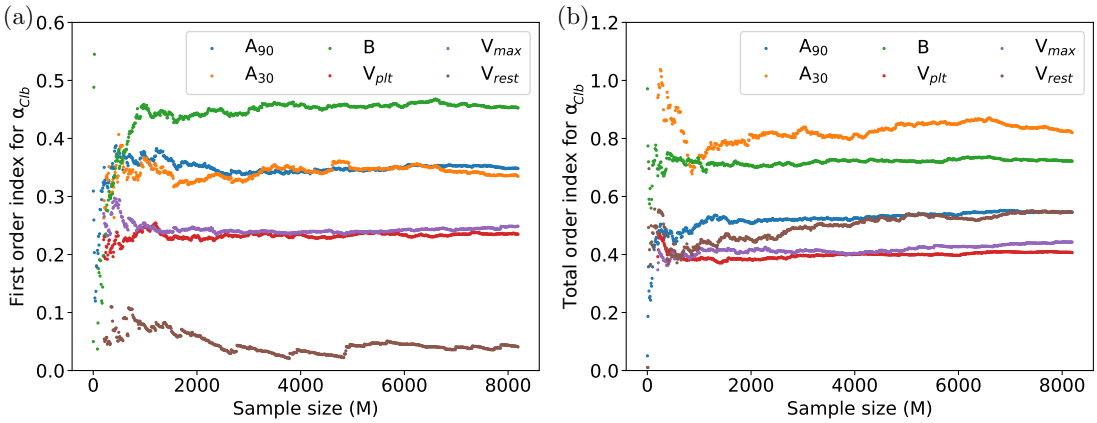

Figure 4.3: Consistency of Sobol sensitivity index estimation. Values of the first-order (a) and total-order (b) sensitivity indices of the background chloride current maximal density α_{Clb} for the six AP biomarkers of interest (as stated in the legend) when calculated with different numbers of samples.

(convergence to true values with larger sample sizes) and unbiasedness (no systematic deviation from true values). Here, I evaluate these properties to ensure the robustness of our Sobol sensitivity indices estimation.

Figure 4.3 demonstrates the consistency of first-order and total-order indices of the parameter α_{Clb} in the large-sample limit across the six AP biomarkers. Specifically, smaller sample sizes M show greater variability, particularly in the total-order indices which are sensitive to interaction effects. As the sample size M is increased, both first-order and total-order indices converge to specific values. The sensitivity indices of all other parameters behave similarly. Based on this consistency test I have fixed the sample size to $M = 8192$ in our subsequent analysis.

To assess the bias of the Sobol sensitivity indices, I compute bootstrap distributions of the first-order and total-order indices, revealing their variability and central tendency. Comparing the mean of the bootstrap estimates to the original Sobol indices allows detection of systematic deviations and bias if any. Figure 4.4 shows the bootstrap distributions for α_{Clb} with the AP feature A_{90}. Both first-order and total-order indices exhibit normal distributions, confirming unbiased estimates at $M = 8192$. Similar unbiased behavior is observed for all other parameters.

Bootstrap distributions, such as those in Figure 4.4, provide a basis for constructing confidence intervals for the Sobol sensitivity indices. Using the empirical "68–95–99.7" rule, approximately 95% of estimates lie within two standard deviations of the mean. Confidence interval lengths computed in this way are presented in Tables 4.4 and 4.5 for all Sobol sensitivity index estimates.

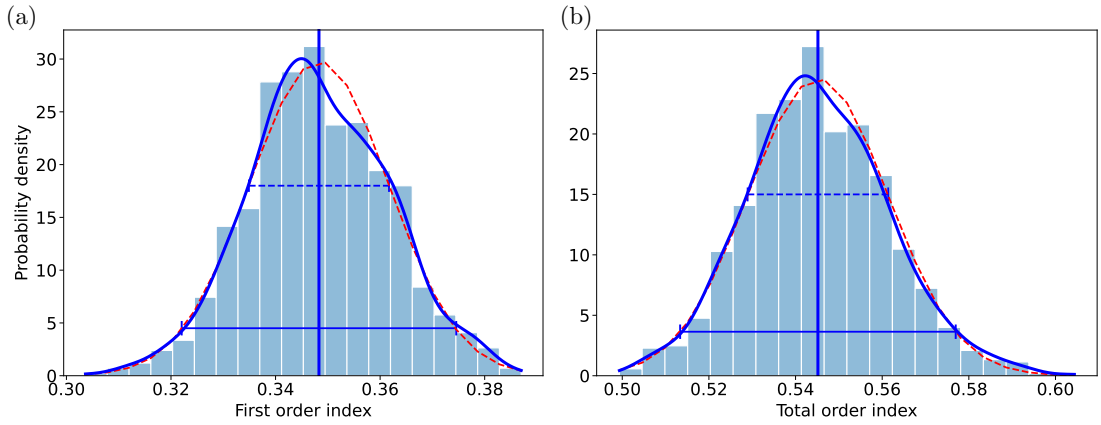

Figure 4.4: Bias of Sobol sensitivity index estimation. Histograms of the bootstrapping distributions of the first-order (a) and total-order (b) sensitivity indices of the background chloride current maximal density α_{Clb} for A_{90} constricted with a sample size of $M = 8192$ are shown in blue. The mean value and the standard deviation of the bootstrapping histograms are shown by the vertical blue line and the horizontal blue bar, respectively. The latter are used to plot a normal distribution (red dashed line) for comparison. The kernel density estimates (KDE) bootstrapping distributions are shown as blue lines. Horizontal blue bars show 1 (broken line) and 2 (solid) standard deviations from mean of the bootstraping distributions.

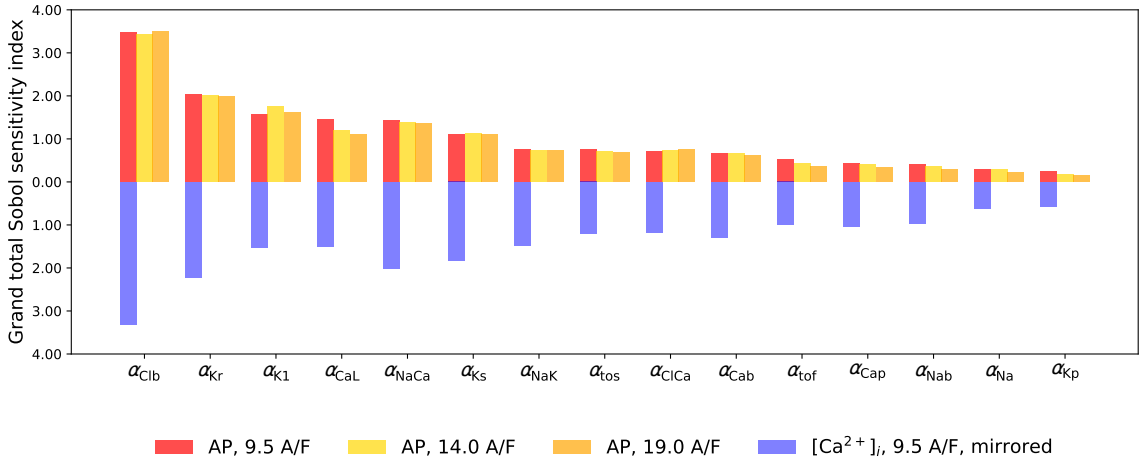

Figure 4.5: Global sensitivity ranking of the parameters considered in the analysis. Barplots of the grand total Sobol sensitivity index with respect to AP biomarkers for three different stimulus amplitudes, as well as with respect to $[\mathrm{Ca}^{2+}]_i$ biomarkers (for amplitude 9.5 A/F only) are included as indicated in the legend.

4.3.3 The Most and Least Important Ionic Currents

I am now ready to rank the relative strengths of ionic currents in the Shannon model based on their influence on the model output biomarkers. The relative strengths of ionic currents I_i, compared to their baseline values from [3], are represented by the factors α_i, while the output biomarkers are listed in Table 4.2. The importance of each current is quantified using the grand total Sobol sensitivity index, defined in equation (4.5c), which measures the combined effect of a single parameter α_i on all biomarkers. The grand total Sobol indices for all 15 currents are shown in Figure 4.5, ranked in decreasing order of their influence on model outputs. I find that, in the notation of equation (4.6) and for stimulus amplitude 9.5 A/F, the vector of ordered

y^k	parameter	S_i^k	95% CI	parameter	S_{Ti}^k	95% CI
A_{30}	α_{Clb}	0.33	0.032	α_{Clb}	0.82	0.065
	α_{NaCa}	0.063	0.019	α_{Kr}	0.49	0.056
	α_{ClCa}	0.036	0.012	α_{NaCa}	0.47	0.05
A_{90}	α_{Clb}	0.35	0.023	α_{Clb}	0.54	0.036
	α_{Kr}	0.14	0.019	α_{Kr}	0.34	0.023
	α_{NaCa}	0.14	0.016	α_{NaCa}	0.24	0.018
B	α_{Clb}	0.45	0.027	α_{Clb}	0.72	0.03
	α_{NaCa}	0.076	0.015	α_{Kr}	0.26	0.025
	α_{CaL}	0.031	0.011	α_{NaCa}	0.24	0.023
V_{plt}	α_{Clb}	0.23	0.021	α_{Clb}	0.41	0.022
	α_{K1}	0.17	0.020	α_{K1}	0.35	0.025
	α_{CaL}	0.15	0.017	α_{Kr}	0.26	0.025
V_{max}	α_{CaL}	0.32	0.024	α_{Clb}	0.44	0.030
	α_{Clb}	0.25	0.024	α_{CaL}	0.40	0.022
	α_{tos}	0.050	0.013	α_{K1}	0.14	0.0098
V_{rest}	α_{K1}	0.23	0.026	α_{Clb}	0.55	0.054
	α_{Kr}	0.068	0.028	α_{Kr}	0.54	0.052
	α_{Clb}	0.041	0.030	α_{K1}	0.47	0.042

Table 4.4: The top three first-order and total-order sensitivity indices with corresponding confidence intervals for the six AP biomarkers considered. S_i^k is the first Sobol index given by equation (4.5a) which measures the individual influence of the parameter α_i on a single AP biomarker y^k and S_{Ti}^k is the total Sobol index given by equation (4.5b) which measures the overall influence of the parameter α_i on a single AP biomarker y^k.

parameters is

$$\langle \alpha_{\text{Clb}}, \alpha_{\text{Kr}}, \alpha_{\text{K1}}, \alpha_{\text{CaL}}, \alpha_{\text{NaCa}}, \alpha_{\text{Ks}}, \alpha_{\text{NaK}}, \alpha_{\text{tos}}, \alpha_{\text{ClCa}}, \alpha_{\text{Cab}}, \alpha_{\text{tof}}, \alpha_{\text{Cap}}, \alpha_{\text{Nab}}, \alpha_{\text{Na}}, \alpha_{\text{Kp}} \rangle. \tag{4.9}$$

Increasing the stimulus amplitude up to 2 times the threshold value does not significantly affect the ranking as also shown in Figure 4.5. The relative strength of the background chloride current α_{Clb}, emerges as the most influential parameter in the Shannon model, followed by that of the potassium current α_{Kr}, the inward rectifier potassium current α_{K1}, the L-type calcium current α_{CaL}, the sodium-calcium exchanger current α_{NaCa}, and the slow delayed rectifier potassium current α_{Ks}. On the other hand, the relative strength of the background potassium current α_{Kp} is found to be the least influential parameter in the model. This rank list constitutes the central result of our analysis.

y^k	Parameter pair	S_{ij}^k	95% CI	y^k	Parameter pair	S_{ij}^k	95% CI
A_{90}	(α_{Kr},α_{Clb})	0.089	0.039	B	(α_{Kr},α_{Clb})	0.032	0.031
B	(α_{Kr},α_{Ks})	0.029	0.021	B	(α_{Ks},α_{Cap})	0.024	0.016
B	(α_{Ks},α_{ClCa})	0.019	0.018	B	(α_{Ks},α_{ClCa})	0.019	0.018
B	(α_{Ks},α_{Kp})	0.023	0.016	B	(α_{Ks},α_{Na})	0.023	0.017
B	(α_{Ks},α_{Nab})	0.022	0.017	B	(α_{Ks},α_{tof})	0.024	0.017
B	(α_{Kp},α_{Na})	0.0087	0.0066	B	(α_{Kp},α_{Nab})	0.0084	0.0063
B	(α_{Kp},α_{tof})	0.0098	0.0065	B	(α_{Na},α_{tof})	0.0055	0.0052
V_{rest}	(α_{Kr},α_{Clb})	0.11	0.059	V_{rest}	(α_{NaCa},α_{ClCa})	0.026	0.024
V_{rest}	(α_{NaCa},α_{Kp})	0.024	0.022	V_{max}	(α_{K1},α_{Clb})	0.028	0.019

Table 4.5: Selected second-order sensitivity indices of 18 parameter pairs for 4 AP biomarkers. S_{ij}^k is the second Sobol index given by equation (4.5a) which measures the pairwise interaction influence of the parameters α_i and α_j on a single AP biomarker y^k. Similar with the work by [94], only the parameter pairs with positive lower limit of the CI are included, showing their significant influences on AP biomarkers.

The results summarised in Figure 4.5 are in general agreement with published experimental findings in terms of identifying the major conductances that influence repolarization of the cardiac AP. A surprising observation emerged from the ranking of global sensitivity is that the highest sensitivity is attributed to the value of the conductance of the background chloride current (I_{Clb}). While this was not expected, a large sensitivity to I_{Clb} was also independently reported in the work of [73] for the Grandi human atrial AP model [95] which in turn is based on the Shannon model. One possible explanation may be that because the intracellular concentration of Cl is constant in the definition of the Shannon model the alteration of this current does not influence this concentration in simulations, but in reality this concentration could be significantly altered when varying I_{Clb}. Our sensitivity analysis reflects the behaviour of the model as currently formulated. The importance of I_{Clb} seems to be generally underappreciated as noted by [96] despite its importance in determining AP duration and the resting membrane potential, both key parameters determining the electrical stability of the heart [97]. In contrast, the next most influential current, the rapidly inactivating delayed rectifier potassium current (I_{Kr}), carried by the hERG channel, is considerably more intensively studied due to the linkage to the pro-arrhythmic condition associated with long QT. The activation of I_{Kr} current late in the repolarization phase ensures the rapid restoration of the resting membrane potential [98, 99] and reduced I_{Kr} prolonges the AP and therefore the QT duration.

The slowly inactivating delayed rectifier potassium current (I_{Ks}) contributes to the cardiac repolarization, particularly during increased heart rates, by preventing excessive prolongation of the AP [100]. The inwardly rectifying potassium current (I_{K1}) is important in determining the resting membrane potential, the initial depolarization and the final repolarization phases of the AP [101, 102]. Early repolarization (phase 1) is shaped by the transient outward potassium current (I_{tos}), which contributes to the characteristic notch in the AP [103]. The L-type calcium current (I_{CaL}), contributes to the initial depolarization (phase 0) initiated by the activation of inward sodium current by contributing to the maximum positive potential [104]. Sustained inward calcium current during the plateau of the AP (phase 2) helps to maintain depolarized potentials and therefore the overall AP duration [104]. The magnitude and direction of the sodium-calcium exchanger current (I_{NaCa}) is dependent on the intracellular sodium and calcium concentrations and the transmembrane voltage [105]. At peak systolic calcium, the high sub-sarcolemma calcium concentrations ensures that the I_{NaCa} is an inward current, causing net efflux of calcium from the cell and contributing to the plateau phase of the AP. On repolarization due to activation of delayed rectifier currents, I_{NaCa} remains an inward current and is one of the main calcium efflux mechanisms [106]. The sodium-potassium pump current (I_{NaK}) is a consequence of the electrogenic stoichiometry of the pump that actively extrudes sodium while importing potassium, maintaining intracellular ion homeostasis. The I_{NaK} magnitude is normally small compared to the other currents listed above and therefore the direct influence on the AP is small. But the activity of the sodium potassium pump maintains normal intracellular sodium levels and thereby indirectly influences intracellular calcium via the sodium calcium exchanger [105]. The indirect effects on calcium sensitive currents and the effects of altered intracellular potassium and sodium concentrations on ionic currents explain the significant indirect influence of the sodium potassium pump on the AP waveform [107].

To produce a secondary ranking of the ionic currents based on their influence on individual biomarkers, I analyze the corresponding total, first-order, and second-order indices. The total and first-order indices are shown in the left columns of Figure 4.6. The total-order index, defined in equation (4.5b), quantifies a parameter's con-

tribution to the variability of a single biomarker, accounting for both direct impacts and interactions with other parameters. The background chloride current relative strength parameter, α_{Clb}, is consistently the most influential for all action potential biomarkers. Following α_{Clb}, the rapid delayed rectifier potassium current parameter (α_{Kr}), the inward rectifier potassium current parameter (α_{K1}), the sodium-calcium exchange current parameter (α_{NaCa}), and the L-type calcium current parameter (α_{CaL}) exhibit significant total-order sensitivity.

To determine whether specific ionic currents influence a biomarker individually or through interactions with other currents, I analyze their first-order Sobol indices. Defined in equation (4.5), the first-order index quantifies the direct effect of a single parameter on a single biomarker, representing the proportion of variance caused solely by that parameter. The first-order indices for the relative strengths of ionic currents are shown in the left column of Figure 4.6. The background chloride current parameter (α_{Clb}) is consistently dominant, particularly for biomarkers such as action potential duration at 30% and 90% repolarization (A_{30} and A_{90}), plateau voltage, and AP bulk. For example, α_{Clb} contributes five times more to the variance of A_{30} than the second- and third-ranked parameters. The resting membrane potential (V_{rest}) is most sensitive to the potassium current parameters (α_{K1} and α_{Kr}), while the maximum AP upstroke (V_{max}) is strongly influenced by the L-type calcium current parameter (α_{CaL}) as it is the major depolarizing current during late upstroke. This effect of calcium current is through the effect on (V_{max}), not influencing the maximum upstroke velocity as (α_{Na}) is almost the sole determinant parameter [108]. The sodium-calcium exchange current parameter (α_{NaCa}) consistently ranks among the top three for several biomarkers, highlighting its importance in action potential dynamics. Conversely, the background potassium current parameter (α_{Kp}) and the slow delayed rectifier potassium current parameter (α_{Ks}) exhibit the lowest first-order indices across all biomarkers.

To assess the joint influence of two currents on biomarkers, we examine their second-order Sobol indices. Table 4.5 lists all second-order indices with a positive lower confidence interval limit. Notably, $S_{\text{Kr,Clb}}$ emerges as the highest second-order index for A_{90}, B, and V_{rest}, while $S_{\text{K1,Clb}}$ dominates for V_{max}. The strong interac-

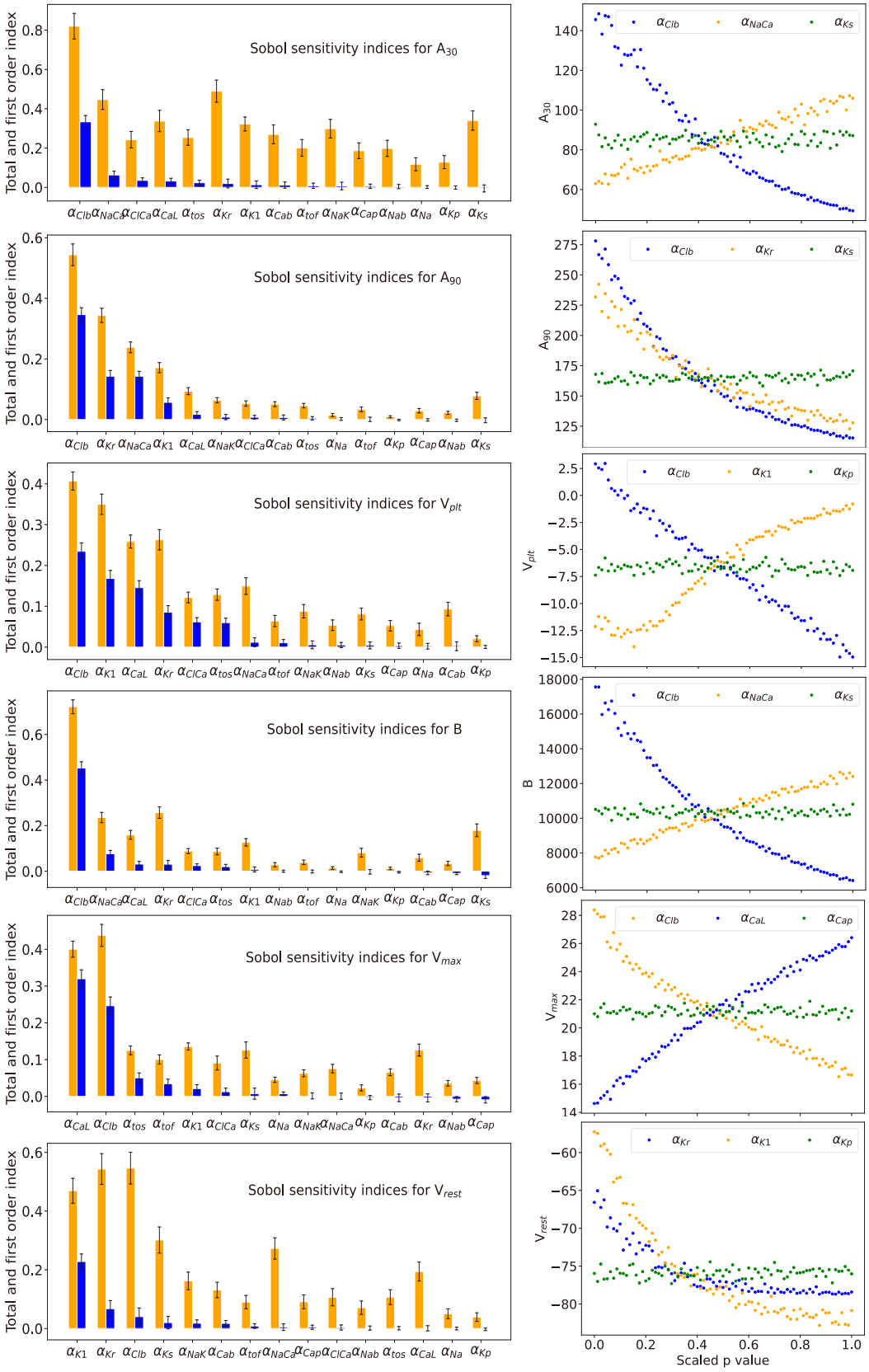

Figure 4.6: (left column) Total and first-order Sobol sensitivity indices for the six studied biomarkers sorted in descending order with respect to the first-order index. (right column) Conditional expectations for the parameters with the largest, the second-largest and the smallest values of the first-order Sobol sensitivity index. To aid visualisation parameter values p are scaled by $p_{\text{scaled}} = (p - p_{\min})/(p_{\max} - p_{\min})$ to $[0, 1]$ on the abscissa.

tion between Cl^- and K^+ conductances aligns with findings in [97], which suggest that the role of I_{Clb} in AP waveform variability depends on its interplay with other ion conductances, especially K^+. Reducing extracellular potassium concentration to suppress I_{Kr} and I_{K1} increases resting potential depolarization, amplifying the depolarizing action of I_{Clb} [97]. Additionally, the slow delayed rectifier potassium current parameter (α_{Ks}) shows significant second-order interaction effects on the AP bulk (B), particularly with parameter α_{Kr}. This supports findings by [109] that blocking I_{Ks} markedly prolongs AP duration when "repolarization reserve" is reduced by I_{Kr} block.

Having identified the parameters that most strongly influence the AP biomarkers, I next explore the explicit relationships between them. The second column of Figure 4.6 displays the conditional expectations of the biomarkers with respect to the parameters with the highest and lowest first-order Sobol indices. These plots show the expected value of a biomarker as a function of a parameter while all other parameters vary randomly. These conditional expectations provide insights into the general dependence of biomarkers on specific parameters and indicate how the biomarker is likely to vary as one parameter changes while the values of all others remain uncertain.

The work of [18] highlights the significant influence of repolarization currents, particularly α_{CaL}, α_{Kr}, α_{tos}, α_{NaK}, and α_{NaCa}, on AP waveform. Consistent with this, I find these parameters ranked within the top eight in Figure 4.5. Unlike the work of [18], our analysis reveals α_{Ks} as influential, likely due to differences in methodology. Their local sensitivity method varied selected parameters by only $\pm 15\%$ and $\pm 30\%$ from the Shannon model's baseline values [3], limiting the analysis to a narrow parameter neighborhood and ignoring interaction effects. In contrast, our global sensitivity method explores a wide parameter space, allowing all parameters to vary simultaneously. This broader approach captures interaction effects, as illustrated in Figure 4.6, where G_{Ks} exhibits low first-order indices for six AP biomarkers but high total-order indices, indicating strong higher-order interaction effects on the AP waveform.

The work of [7] systematically explored the effects of simultaneously varying the magnitude of six transmembrane current conductances in the Shannon model. Using clutter-based dimension reordering, they identified α_{CaL} as having the greatest

influence on AP variability at both 400 ms and 1000 ms, along with α_{K1} and α_{to} at 400 ms and 1000 ms, respectively. These findings align with our results, where these three parameters also ranked among the top eight in Figure 4.5, despite our analysis being conducted at a different basic cycle length.

In contrast to the findings of [12], α_{Na} is not the most influential parameter in this study. This discrepancy may stem from our focus on successfully excited cells, which for stimulus amplitude 9.5 A/F limits the range of α_{Na} to values > 1. If values of $\alpha_{\text{Na}} < 1$ were to be considered, the effects would have included the differences between normal and failing AP responses which are, of course, huge. The effects of α_{Na} on normal APs alone are far less significant.

4.3.4 Extension Sensitivity Analysis for Intracellular Calcium Biomarkers

A number of studies using populations of models use biomarkers of intracellular calcium concentration to calibrate them [110]. To facilitate this, I have extended the Sobol sensitivity analysis to include the following four intracellular calcium biomarkers: (a) ED: $[Ca^{2+}]_i$ at the end of diastole; (b) PSV: peak systolic value of $[Ca^{2+}]_i$; (c) T_{peak}: time from stimulus to peak $[Ca^{2+}]_i$; (d) D_{50}: period of time when $[Ca^{2+}]_i$ remains elevated above a threshold of 50% recovery from the peak value to the resting value, informally duration at 50% amplitude. The grand total Sobol indices based on these four biomarkers are shown in blue in Figure 4.5 for the standard setup of our study. The top seven most influential parameters remain the same as those found by analysis of AP biomarkers shown in red in Figure 4.5, with the relative strength of the background chloride current α_{Clb} still emerging as the most influential parameter, followed by $\alpha_{\text{Kr}}, \alpha_{\text{NaCa}}, \alpha_{\text{Ks}}$. On the other hand, the relative strength of the background potassium current α_{Kp} remains to be the least influential parameter in the model. The higher rank of α_{NaCa} reflects its large importance for intracellular calcium dynamics and this is because the rise in intracellular calcium concentration activates the Na+/Ca2+ exchanger cell membrane pump [111].

4.3.5 A Hierarchy of Reduced Shannon Models

Using the ranked Shannon model parameters based on their grand Sobol sensitivity indices (see Figure 4.5 and equation (4.9)), I now address the second main goal of our sensitivity analysis: constructing a hierarchy of reduced Shannon models. These reduced models are with respect to the sensitivity of six AP biomarkers shown in Table 4.2. This hierarchy is formed by successively fixing the least significant parameters to their baseline values, as follows:

$$\begin{aligned}
\mathbf{y} &= \mathbf{f}\big(\langle \alpha_{\mathrm{Clb}}, \alpha_{\mathrm{Kr}}, \alpha_{\mathrm{K1}}, \alpha_{\mathrm{CaL}}, \alpha_{\mathrm{NaCa}}, \alpha_{\mathrm{Ks}}, \alpha_{\mathrm{NaK}}, \alpha_{\mathrm{tos}}, \alpha_{\mathrm{ClCa}}, \alpha_{\mathrm{Cab}}, \alpha_{\mathrm{tof}}, \alpha_{\mathrm{Cap}}, \alpha_{\mathrm{Nab}}, \alpha_{\mathrm{Na}}, \alpha_{\mathrm{Kp}} \rangle\big), \\
\mathbf{y}^{\langle 14 \rangle} &= \mathbf{f}\big(\langle \alpha_{\mathrm{Clb}}, \alpha_{\mathrm{Kr}}, \alpha_{\mathrm{K1}}, \alpha_{\mathrm{CaL}}, \alpha_{\mathrm{NaCa}}, \alpha_{\mathrm{Ks}}, \alpha_{\mathrm{NaK}}, \alpha_{\mathrm{tos}}, \alpha_{\mathrm{ClCa}}, \alpha_{\mathrm{Cab}}, \alpha_{\mathrm{tof}}, \alpha_{\mathrm{Cap}}, \alpha_{\mathrm{Nab}}, \alpha_{\mathrm{Na}}, 1 \rangle\big), \\
\mathbf{y}^{\langle 13 \rangle} &= \mathbf{f}\big(\langle \alpha_{\mathrm{Clb}}, \alpha_{\mathrm{Kr}}, \alpha_{\mathrm{K1}}, \alpha_{\mathrm{CaL}}, \alpha_{\mathrm{NaCa}}, \alpha_{\mathrm{Ks}}, \alpha_{\mathrm{NaK}}, \alpha_{\mathrm{tos}}, \alpha_{\mathrm{ClCa}}, \alpha_{\mathrm{Cab}}, \alpha_{\mathrm{tof}}, \alpha_{\mathrm{Cap}}, \alpha_{\mathrm{Nab}}, 1, 1 \rangle\big), \\
&\cdots \\
\mathbf{y}^{\langle 1 \rangle} &= \mathbf{f}\big(\langle \alpha_{\mathrm{Clb}}, 1, 1, 1, 1, 1, 1, 1, 1, 1, 1, 1, 1, 1, 1 \rangle\big).
\end{aligned} \tag{4.10}$$

The original Shannon model [3] corresponds to

$$\mathbf{y}^{\langle 0 \rangle} = \mathbf{f}\big(\langle 1, 1, 1, 1, 1, 1, 1, 1, 1, 1, 1, 1, 1, 1, 1 \rangle\big), \tag{4.11}$$

representing the lowest hierarchical level where all parameters are fixed.

Figure 4.7 quantifies the global discrepancy between the full model ($\mathbf{y}$) and the reduced models ($\mathbf{y}^{\langle M \rangle}$) at hierarchical levels M over the parameter ranges of normal response. Two measures of discrepancy are presented: the mean relative error, defined by Equation (4.8) and plotted on the left-hand ordinate axis, and the coefficient of determination (R^2), shown on the right-hand ordinate axis, both as functions of M. For models $\mathbf{y}^{\langle 0 \rangle}$ to $\mathbf{y}^{\langle 5 \rangle}$, where fewer than the six most sensitive parameters are varied, the discrepancy is non-monotonic and remains too large. Consequently, these models do not approximate the full model well and are excluded from the plots in Figure 4.7, which only includes models from $\mathbf{y}^{\langle 6 \rangle}$ to $\mathbf{y}$. At higher hierarchical levels ($M \geq 6$), the discrepancy decreases monotonically with increasing M. The mean relative error approaches zero, while R^2 approaches unity, indicating improved accuracy. Figure

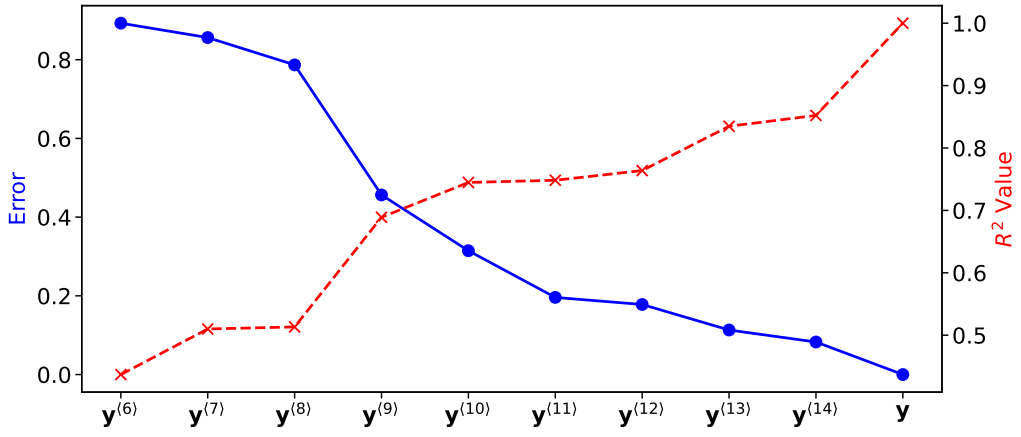

Figure 4.7: Deviation of reduced models $\mathbf{y}^{\langle M\rangle}$ from the full model $\mathbf{y}$ as measured by the mean relative error (blue dots; left ordinate axis) and the coefficient of determination R^2 (red crosses, right ordinate axis).

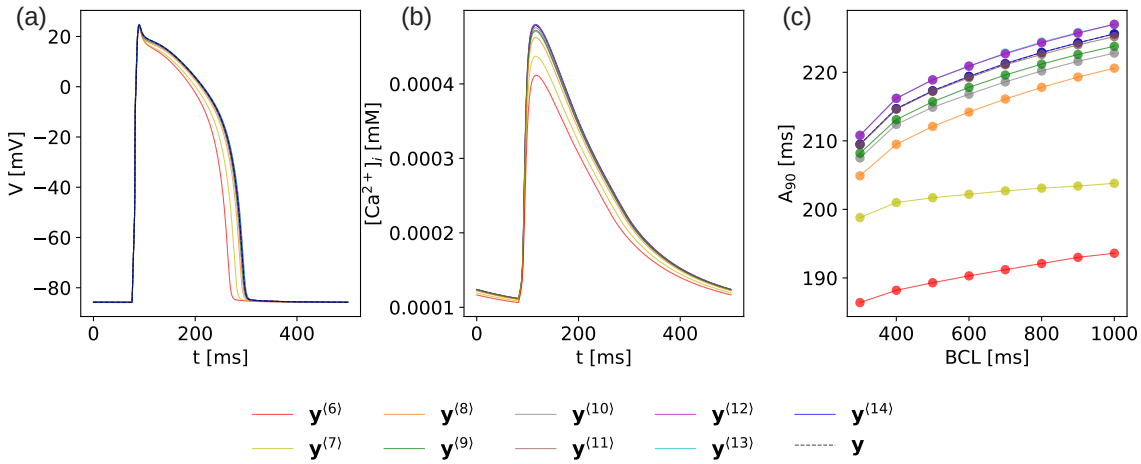

Figure 4.8: A local illustration of the accuracy of reduced models. Panel (a) and (b) show AP forms, and Calcuim transients $[\mathrm{Ca}]_i^{2+}$, while panel (c) shows A_{90} restitution curves (A_{90} for periodically excited waveforms as a function of basic cycle length) for reduced models $\mathbf{y}^{\langle 6\rangle}$ to $\mathbf{y}^{\langle 14\rangle}$ in comparison with the full model $\mathbf{y}$. The models are evaluated locally so that for the full model all parameters are set equal to 0.8, while for the models at hierarchical level M the M "variable" parameters are also set to 0.8 while the rest are kept at baseline value corresponding to 1.

4.8 provides a local comparison of the reduced and full models to offer an intuitive understanding of their accuracy.

While a hierarchy of models can be constructed by ranking parameters based on their grand total sensitivity index, more "economical" specialized reduced models can be obtained to capture individual biomarkers. For each biomarker of interest, this is achieved by ranking parameters based on their total sensitivity indices. To illustrate, Figure 4.9 presents scatter plots of A_{90} values obtained from the reduced model

$$\mathbf{y}^{\langle 6\rangle} = \mathbf{f}\big(\langle \alpha_{\mathrm{Clb}}, \alpha_{\mathrm{Kr}}, \alpha_{\mathrm{NaCa}}, \alpha_{\mathrm{K1}}, \alpha_{\mathrm{CaL}}, \alpha_{\mathrm{Ks}}, 1, 1, 1, 1, 1, 1, 1, 1, 1\rangle\big),$$

and its "complement" model

$$\overline{\mathbf{y}^{\langle 6\rangle}} = \mathbf{f}\big(\langle 1,1,1,1,1,1,\alpha_{\mathrm{NaK}},\alpha_{\mathrm{tos}},\alpha_{\mathrm{ClCa}},\alpha_{\mathrm{Cab}},\alpha_{\mathrm{tof}},\alpha_{\mathrm{Cap}},\alpha_{\mathrm{Nab}},\alpha_{\mathrm{Na}},\alpha_{\mathrm{Kp}}\rangle\big),$$

against the corresponding values from the full model in panels (a) and (b), respectively. The coefficient of determination (R^2) between the reduced model ($\mathbf{y}^{\langle 6\rangle}$) and the full model ($\mathbf{y}$) is 0.93, while R^2 for the complement model ($\overline{\mathbf{y}^{\langle 6\rangle}}$) and the full model is only 0.06. This demonstrates that the reduced model $\mathbf{y}^{\langle 6\rangle}$, while insufficient to capture all six biomarkers simultaneously, accurately reproduces the single biomarker A_{90}. A systematic trend is observed in the accuracy of the reduced models, where the agreement with the full model is higher for small values of A_{90}, while the discrepancy increases for larger A_{90}. Biophysically, this behaviour can be explained by reduced repolarisation reserve in prolonged APs, where the balance between inward and outward ionic currents becomes increasingly fragile and nonlinear [112]. Large values of A_{90} correspond to extended repolarisation phases, during which parameter perturbations can produce large changes in duration through nonlinear higher-order interaction effects among multiple ionic currents. In contrast, for shorter A_{90}, repolarisation is dominated by a smaller subset of strong currents, leading to a more robust and approximately linear dependence on the retained parameters, and therefore improved agreement with the reduced models. Figure 4.10 shows how R^2 changes with the reduced model of parameters labeled as "significant" following the decreasing order of total order index. The six curves turn out to be an increasing trend with slight fluctuation when the number of parameter is small. The two curves for A_{90} and B reach 90% with six and ten sensitive parameters respectively while the curve for A_{30} needs all fifteen parameters to go beyond 90%. One reason could be all parameters have higher order interaction effects on A_{30} so that evaluation for reduced model of A_{30} will become inaccurate with small number of least significant parameters. Table 4.6 lists other specialized reduced models that capture each of the six biomarkers with $R^2 \geq 0.9$, a threshold often considered sufficient to assess how well one variable replicates another.

The appropriate accuracy of a Shannon model reduction depends on the specific

AP biomakers	R^2 value	Parameters
A_{90}	0.93	$\alpha_{\text{Clb}}, \alpha_{\text{Kr}}, \alpha_{\text{NaCa}}, \alpha_{\text{K1}}, \alpha_{\text{CaL}}, \alpha_{\text{Ks}}$
A_{30}	1.0	$\alpha_{\text{Clb}}, \alpha_{\text{Kr}}, \alpha_{\text{NaCa}}, \alpha_{\text{Ks}}, \alpha_{\text{CaL}}, \alpha_{\text{K1}}, \alpha_{\text{NaK}}, \alpha_{\text{Cab}}, \alpha_{\text{tos}}, \alpha_{\text{ClCa}}$ $\alpha_{\text{tof}}, \alpha_{\text{Nab}}, \alpha_{\text{Cap}}, \alpha_{\text{Kp}}, \alpha_{\text{Na}}$
V_{max}	0.91	$\alpha_{\text{Clb}}, \alpha_{\text{CaL}}, \alpha_{\text{K1}}, \alpha_{\text{Ks}}, \alpha_{\text{Kr}}, \alpha_{\text{tos}}, \alpha_{\text{tof}}, \alpha_{\text{ClCa}}, \alpha_{\text{NaCa}}, \alpha_{\text{Cab}}, \alpha_{\text{NaK}}$
V_{rest}	0.92	$\alpha_{\text{Clb}}, \alpha_{\text{Kr}}, \alpha_{\text{K1}}, \alpha_{\text{Ks}}, \alpha_{\text{NaCa}}, \alpha_{\text{CaL}}, \alpha_{\text{NaK}}, \alpha_{\text{Cab}}, \alpha_{\text{tos}}, \alpha_{\text{ClCa}},$ $\alpha_{\text{Cap}}, \alpha_{\text{tof}}, \alpha_{\text{Nab}}, \alpha_{\text{Na}}$
B	0.91	$\alpha_{\text{Clb}}, \alpha_{\text{Kr}}, \alpha_{\text{NaCa}}, \alpha_{\text{Ks}}, \alpha_{\text{CaL}}, \alpha_{\text{K1}}, \alpha_{\text{ClCa}}, \alpha_{\text{tos}}$
V_{plt}	0.92	$\alpha_{\text{Clb}}, \alpha_{\text{K1}}, \alpha_{\text{Kr}}, \alpha_{\text{CaL}}, \alpha_{\text{NaCa}}, \alpha_{\text{tos}}, \alpha_{\text{ClCa}}, \alpha_{\text{Cab}}, \alpha_{\text{NaK}}, \alpha_{\text{Ks}}$

Table 4.6: Minimal sets of parameters for specialised reduced models that capture a specific biomarker with a coefficient of determination value R^2 of at least 0.9. Parameters are ranked by their total-order index from large to small. All 15 parameters are required for A_{30} to achieve high accuracy ($R^2 \geq 0.9$) because of their non-negligible high-order interaction effects.

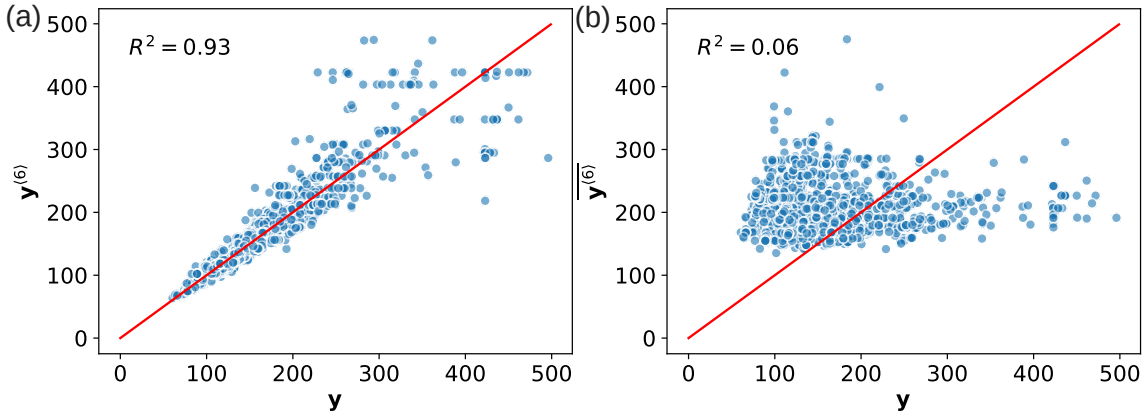

Figure 4.9: Scatter plots of A_{90} values obtained from the reduced model $\mathbf{y}^{\langle 6 \rangle}$ (a) and the reduced model $\overline{\mathbf{y}^{\langle 6 \rangle}}$ (b) compared to the full model $\mathbf{y}$.

application it is intended to investigate. The discrepancy analysis presented in this section provides a framework for selecting a hierarchical model that balances simplicity and accuracy to meet the requirements of the application.

4.4 Conclusion

This chapter presents a global sensitivity analysis of the Shannon model of rabbit ventricular myocyte electrophysiology, focusing on the influence of ionic current strength parameters on key AP biomarkers. By ranking parameters using Sobol sensitivity indices, I have identified the most influential ionic currents, including $\alpha_{\text{Clb}}, \alpha_{\text{Kr}}, \alpha_{\text{K1}}, \alpha_{\text{CaL}}, \alpha_{\text{NaCa}}$ and α_{Ks}, which dominate the model's variability.

Our analysis demonstrates the utility of a global sensitivity approach in capturing both direct effects and interaction effects among parameters, providing a deeper

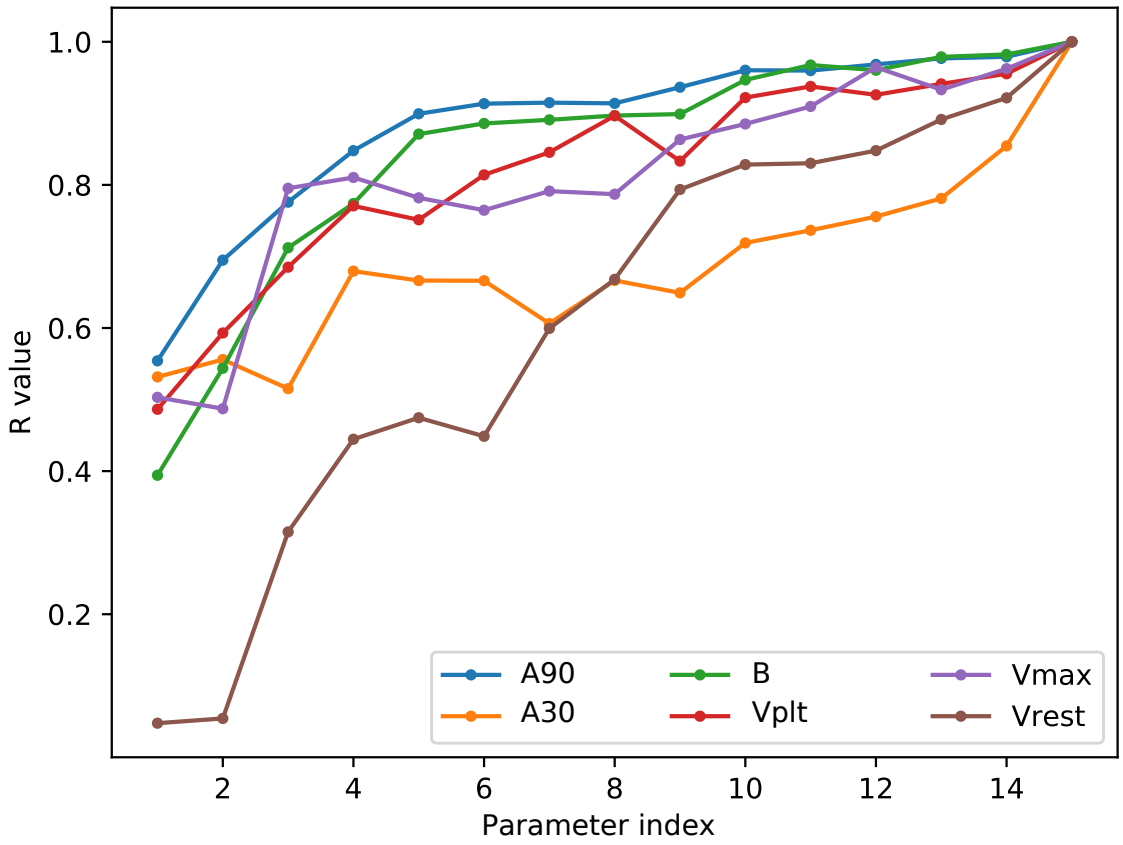

Figure 4.10: Deviation of specialised reduced models that capture six AP biomarkers with correspondent coefficients of determination value R^2. Black line is a line with R^2 value equal to 90%. The parameter selection for each AP biomarker is based on the descending rank of total order index.

understanding of their role in shaping AP dynamics. For instance, α_{Ks}, which exhibited low first-order indices but high total-order indices, was found to contribute significantly through interaction effects, highlighting the importance of considering higher-order sensitivity metrics.

The hierarchical model framework constructed in this section offers a practical approach to reducing model complexity while maintaining accuracy. Models that exclude less influential parameters ($M \geq 8$) were shown to adequately approximate the full model, as evidenced by monotonic reductions in mean relative error and increases in R^2. Additionally, specialized reduced models targeting individual biomarkers were developed, achieving high accuracy ($R^2 \geq 0.9$) while requiring fewer parameters. The findings provide a foundation for tailoring the Shannon model to other specific applications, balancing simplicity with accuracy. The insights gained into parameter importance and interaction effects can guide future investigations, including the development of reduced models for multi-scale simulations and the exploration of electrophysiological variability across different cell types and conditions. As an example,

in our prior work on inter-cell variability of rabbit ventricular electrophysiology [2, 6] parameter choices were made by educated guesses. The results of the current analysis complement these works and provide justification for their parameter choices.

A notable limitation of this chapter is its focus on sensitivity analysis at a fixed stimulation rate of 2 Hz, without systematically exploring AP dynamics at other pacing rates. This narrow scope may limit the generalizability of the findings across diverse physiological and pathological conditions where cellular pacing rates vary. Future studies should extend this analysis to include a broader range of stimulation frequencies to enhance applicability. Additionally, the choice and number of model parameters and biomarkers warrant further investigation. While this chapter focused on a subset of parameters, the Shannon model includes nearly 200 parameters, and incorporating biomarkers such as restitution properties or AP duration rate adaptation could provide a more comprehensive perspective. However, currently there are no experimental studies that assess the intracellular calcium, restitution, or other biomarkers in addition to AP biomarkers. Expanding the sensitivity analysis to alternative AP models, such as the Mahajan model [19] for rabbit ventricular myocytes, would also enhance the robustness of the findings. Our sensitivity analysis reflects the behavior of the Shannon model as currently formulated. However, the assumption of constant intracellular chloride concentration in the model is a simplification that may exaggerate the influence of α_{Clb}. Future extensions incorporating dynamic chloride ion homeostasis will be crucial to reassessing the physiological relevance of this finding. Nonetheless, the result highlights a potentially unappreciated role of chloride currents in AP dynamics, meriting further experimental and modelling investigation.

From a technical standpoint, alternative sensitivity analysis methods offer potential avenues for improving accuracy and efficiency. A limitation of the present Sobol analysis is that the sampling distribution was defined using a hyper-rectangular parameter space. Although this approach provides broad coverage of the admissible parameter ranges, it does not explicitly account for the physiologically valid "Busse Balloon" region within that space. Future work could consider rejection sampling strategies [113, 114], whereby samples falling outside the physiologically valid region are discarded and resampled. Another possibility would be to use the population of

cell-specific AP models developed in Chapter 5 to estimate a physiologically informed parameter distribution. Since all models within this population exhibit normal electrophysiological behaviour, sampling directly from this distribution may provide a more realistic basis for global sensitivity analysis and could yield sensitivity indices that are more representative of experimentally observed cellular variability. Additionally, comparative studies could evaluate whether these methods yield better insights or computational benefits. The parameter space dimension reduction proposed in this chapter provides valuable guidance for selecting fitting parameters in sample-specific electrophysiological modelling, enabling the study of specific cellular states and predictions of cellular behavior under varied external conditions.

Finally, the results of the global sensitivity analysis presented in this chapter provide a principled basis for subsequent parameter estimation. Specifically, the eight most influential parameters identified through grand total Sobol sensitivity indices are selected as the core parameters in the parameter estimation studies presented in Chapter 5. By restricting the optimisation to this reduced parameter set, the computational cost of parameter estimation is substantially reduced while preserving the model's ability to reproduce key electrophysiological features. This sensitivity-informed parameter selection enables a more efficient and interpretable estimation process and forms a central component of the modelling workflow developed in the remainder of this thesis.

Chapter 5

A Large Population of Cell-specific Action Potential Models Replicating Fluorescence Recordings of Voltage in Rabbit Ventricular Myocytes

In this chapter, the sensitivity analysis framework developed earlier is applied to fluorescence based voltage recordings from a large number of rabbit ventricular myocytes. By estimating a subset of eight most influential model parameters for each cell, a large population of cell-specific AP models is constructed. This population-level approach enables the simultaneous reproduction of experimentally observed biomarker distributions and accurate fits to AP waveforms on a cell-by-cell basis, thereby providing a quantitative description of healthy rabbit ventricular electrophysiological variability.

5.1 Introduction

Electrophysiological variability is a fundamental characteristic of cardiac myocytes, even within healthy tissue. Experimental studies have demonstrated that uncoupled

ventricular myocytes exhibit substantial differences in action potential morphology, duration, and repolarization dynamics when measured under identical conditions. Understanding the origins and implications of this variability is crucial for interpreting experimental data, developing robust cardiac models, and improving predictions of tissue- and organ-scale behaviour.

Traditional cardiac electrophysiology models are typically calibrated to population-averaged experimental data, resulting in a single representative parameter set. While such models can reproduce mean electrophysiological behaviour, they fail to capture the breadth of observed inter-cell variability and may obscure important relationships between ionic properties and emergent cellular dynamics. In recent years, population-based modelling approaches have emerged as a powerful alternative, in which variability is represented through ensembles of model variants rather than a single nominal model.

In this chapter, a population of cell-specific AP models is constructed by fitting a well-established rabbit ventricular myocyte model to fluorescence voltage recordings from a large number of individual cells, as introduced in Section 1.1. Parameter estimation is performed for a subset of influential ionic current parameters identified through global sensitivity analysis, enabling efficient and accurate fitting of full action potential waveforms. The resulting population comprises nearly 1200 calibrated model variants that collectively reproduce experimentally observed ranges and distributions of electrophysiological biomarkers, while also matching measurements at the single-cell level.

This population of calibrated models may represent a random sample from the phenotype of healthy rabbit ventricular myocytes. Analysis of the estimated parameters allows the characterization of marginal and joint parameter distributions, the assessment of parameter correlations, and the investigation of how commonly used biomarkers depend on underlying electrophysiological properties. Together, these results demonstrate the feasibility of large-scale, cell-specific parameter estimation and provide new insights into the structure of electrophysiological variability in healthy ventricular myocardium. The work presented in this chapter is published in [2]:
Simitev, R. , Gilchrist, R., Yang, Z., Myles, R. , Burton, F. and Smith, G. (2025)

A large population of cell-specific action potential models replicating fluorescence recordings of voltage in rabbit ventricular myocytes. Royal Society Open Science, 12(3): 241539, 2025. doi.org/10.1098/rsos.241539.

5.2 Method and Model

5.2.1 Parameter Estimation in Dynamical Systems

The estimation of electrophysiological model parameters is formulated within the framework of deterministic dynamical systems. Each isolated cardiomyocyte is represented as a spatially lumped system governed by a set of ordinary differential equations,

$$\frac{d\mathbf{x}}{dt} = \mathbf{f}(t, \mathbf{x}; \boldsymbol{\theta}), \qquad \mathbf{x}(0) = \mathbf{x}_0, \tag{5.1}$$

where $t \in \mathbb{R}$ denotes time, $\mathbf{x}(t) \in \mathbb{R}^d$ is the vector of state variables, $\boldsymbol{\theta} \in \mathbb{R}^k$ is a vector of model parameters, and $\mathbf{x}_0$ denotes the initial conditions. Observable quantities, such as the transmembrane potential, are obtained through a mapping

$$\mathbf{y}(t) = \mathbf{s}(\mathbf{x}(t)). \tag{5.2}$$

Experimental data consist of discrete observations $\{(t_j, \mathbf{Y}_j)\}_{j=1}^{K}$, where $\mathbf{Y}_j \in \mathbb{R}^n$ denotes measurements of the observable outputs at time t_j.

Experimental recordings are subject to measurement noise and intrinsic biological fluctuations. Accordingly, the observed data are modeled as random variables,

$$\mathbf{Y}_j = \mathbf{y}(t_j; \boldsymbol{\theta}, \mathbf{x}_0) + \boldsymbol{\varepsilon}_j, \tag{5.3}$$

where the noise terms $\boldsymbol{\varepsilon}_j$ are assumed to be independent and identically distributed Gaussian random variables with zero mean and common variance σ^2. Under this assumption, each observation follows a normal distribution centered at the model prediction. The unknown variance σ^2 is treated on equal footing with the model parameters and initial conditions and is incorporated into an augmented parameter vector $\boldsymbol{\Theta} \in (\boldsymbol{\theta}, \mathbf{x}_0, \sigma) \in \mathbb{R}^l$ with $l \leq d + k + 1$.

Parameter estimation is performed using the maximum likelihood principle. Under the Gaussian noise model, the likelihood of the observed data given the parameters is expressed as

$$\mathcal{L}(\mathbf{Y}, \boldsymbol{\Theta}) = P(\mathbf{Y}|\boldsymbol{\Theta}) = \prod_{j=1}^{K} \frac{1}{\sqrt{2\pi\sigma^2}} \exp\left(-\frac{1}{2\sigma^2} \left\|\mathbf{Y}_j - \mathbf{y}(t_j; \boldsymbol{\theta}, \mathbf{x}_0)\right\|^2\right). \tag{5.4}$$

Maximising this likelihood is equivalent to minimising a weighted sum of squared residuals between model predictions and experimental observations. The resulting maximum likelihood estimate (MLE),

$$\hat{\boldsymbol{\Theta}} = \arg\max_{\boldsymbol{\Theta} \in \Omega} \mathcal{L}(\mathbf{Y}, \boldsymbol{\Theta}), \tag{5.5}$$

provides a point estimate of the parameters, where Ω denotes a suitably constrained parameter domain. In practice, this optimisation problem is solved using global, derivative-free optimisation methods.

Errors in the estimated parameters are assumed to be negligible from numerical optimisation compared with that caused by experimental measurement noise. Consequently, the accuracy of the parameter estimates is characterised by their standard errors, defined as the square roots of the variances $\mathrm{Var}[\hat{\boldsymbol{\Theta}}(\mathbf{Y})]$. These variances are directly related to the estimated noise variance $\hat{\sigma}^2$ of the voltage measurements, which is obtained as part of the maximum likelihood estimation procedure.

To derive an expression for the standard errors, the observed data $\mathbf{Y}$ are approximated by the model output $\mathbf{y}$, and the relationship between the estimated parameters $\hat{\boldsymbol{\Theta}}$ and the model output is linearised using a first-order Taylor expansion about the expected value $\mathbb{E}[\mathbf{y}]$. Under this linear approximation, the standard errors of the parameter estimates are given by

$$\boldsymbol{\sigma}_{\hat{\boldsymbol{\Theta}}} = \hat{\sigma}\sqrt{\mathrm{diag}[(J^\top J)^{-1}]}, \tag{5.6}$$

where J denotes the Jacobian matrix of partial derivatives of the model outputs with respect to the parameters, evaluated at the maximum likelihood estimate.

The quality of a parameter fit is assessed using a goodness-of-fit test based on the

distribution of the residual errors. Under the assumptions that the observations are normally distributed and that the model output is locally linear with respect to the parameters in the vicinity of the maximum likelihood estimate, the normalised sum of squared residuals,

$$\hat{\chi}^2(\hat{\mathbf{\Theta}}) = \sum_{j=1}^{K} \frac{\left\| \mathbf{Y}_j - \mathbf{y}(t_j; \hat{\boldsymbol{\theta}}, \hat{\mathbf{x}}_0) \right\|^2}{\hat{\sigma}^2}, \tag{5.7}$$

follows a chi-squared distribution with

$$\nu = K - l \tag{5.8}$$

degrees of freedom, where l denotes the number of estimated parameters.

Let H_0 denote the null hypothesis that the model assumptions are valid and that the fitted model provides an adequate description of the data. The corresponding p value under H_0 of obtaining a value of the test statistic χ^2_ν that exceeds the observed value $\hat{\chi}^2_\nu(\hat{\mathbf{\Theta}})$ measured at the maximum-likelihood estimates is computed as

$$p = \mathbb{P}\left(\chi^2_\nu \geq \hat{\chi}^2(\hat{\mathbf{\Theta}}) \;\middle|\; H_0\right) = \int_{\hat{\chi}^2(\hat{\mathbf{\Theta}})}^{\infty} P(\chi^2_\nu)\, d\chi^2_\nu, \tag{5.9}$$

where $P(\chi^2_\nu)$ denotes the probability density function of the chi-squared distribution with ν degrees of freedom. The null hypothesis is rejected at significance level α if $p < \alpha$.

Although the electrophysiological models considered here are nonlinear, the application of this goodness-of-fit test remains appropriate in practice and is commonly adopted in nonlinear regression settings [115].

When data are available from a population of N isolated cardiomyocytes, parameter estimation and goodness-of-fit testing are performed independently for each cell. I consider a collection of N isolated cardiomyocytes,

$$\mathcal{C} = \{C_i\}_{i=1}^{N}, \tag{5.10}$$

each associated with an experimentally recorded dataset,

$$\mathcal{D} = \{D_i\}_{i=1}^{N}, \tag{5.11}$$

Then the population of calibrated models is defined as the set of all accepted cell-specific parameter estimates,

$$\mathcal{M} = \left\{\hat{\boldsymbol{\Theta}}_i \pm \boldsymbol{\sigma}_i\right\}_{i=1}^{N}, \qquad \text{such that } p_i > \alpha, \tag{5.12}$$

where p_i denotes the goodness-of-fit p value for cell i. This population represents a statistical sample of electrophysiological phenotypes consistent with the experimental observations and model assumptions.

5.2.2 Fluorescence Recordings of AP Waveforms

This work was done by the team of Professor Godfrey Smith from University of Glasgow. AP waveforms were obtained from a newly acquired dataset consisting of fluorescence-based voltage recordings from 1228 isolated rabbit ventricular cardiomyocytes. Cells were enzymatically isolated from the hearts of eight male New Zealand White rabbits using established protocols, and optical measurements of transmembrane voltage were performed as described previously [6]. All cardiomyocytes were harvested from the free wall of the left ventricle.

Following isolation, cells were incubated at room temperature for 16 minutes with the voltage-sensitive dye FluoVolt (Thermo Fisher Scientific) at a final concentration of 0.08 $\mu\mathrm{l\,ml^{-1}}$. During recordings, cardiomyocytes were superfused with a Krebs–Henseleit solution containing (in mM): 120 NaCl, 1.8 $CaCl_2$, 20 HEPES, 5.4 KCl, 0.52 NaH_2PO_4, 3.5 $MgCl_2{\cdot}6H_2O$, 20 taurine, 10 creatine, and 11 glucose, adjusted to pH 7.4 at 37°C.

Electrical stimulation was applied using field pulses of 40 V amplitude and 2 ms duration at a pacing frequency of 2 Hz. Prior to data acquisition, cells were paced for five minutes to ensure steady-state electrophysiological behaviour. Fluorescence signals were subsequently recorded at a sampling frequency of 10 kHz over a duration

of 2.5 s, corresponding to five consecutive APs per cell. For each cardiomyocyte, these five beats were temporally aligned and averaged to produce a single representative AP waveform.

Beat-to-beat variability was quantified and verified to be minimal, with variations below 2% for all included recordings, consistent with previous analyses [6]. All experiments were conducted at physiological temperature (37°C). While the dataset allows subdivision of cells based on anatomical location (apical versus basal, endocardial, mid-myocardial, or epicardial regions) and animal origin, no such stratification is applied here. Instead, all recorded cardiomyocytes are treated as members of a single large population.

Accordingly, the experimental dataset is represented as a collection of cell-specific fluorescence time series,

$$\mathcal{D} = \left\{ D_i = \{(t_j, V_{i,j})\}_{j=1}^{K} \right\}_{i=1}^{N}, \qquad t_j = j\,\Delta t, \tag{5.13}$$

where $\Delta t = 10^{-4}$ s is the sampling interval, $V_{i,j}$ denotes the fluorescence-derived voltage signal of cell i at time t_j, $K = 5000$ is the number of time points per recording, and $N = 1228$ is the total number of recorded cardiomyocytes. Representative examples of averaged AP waveforms are shown in Figure 5.1.

5.2.3 Baseline AP Model

The rabbit ventricular myocyte model developed by Shannon et al. [3] is adopted as the baseline electrophysiological model for fitting the experimental dataset $\mathcal{D}$. All model equations, parameter definitions, and simulation settings are identical to those specified in equation (4.1). The only modification introduced concerns the sodium reversal potential across the sarcolemma. Specifically, the Nernst formulation for sodium was replaced by a fixed value, $E_{\mathrm{Na,SL}} = -15$ mV, in order to better reproduce the experimentally observed waveforms $\mathcal{D}_i$, in which the peak upstroke amplitudes are consistently smaller than those generated by the original Shannon model. This adjustment reflects uncertainty regarding the precise electrical conditions that initiate the AP under field stimulation and the model's capacity to accurately capture the

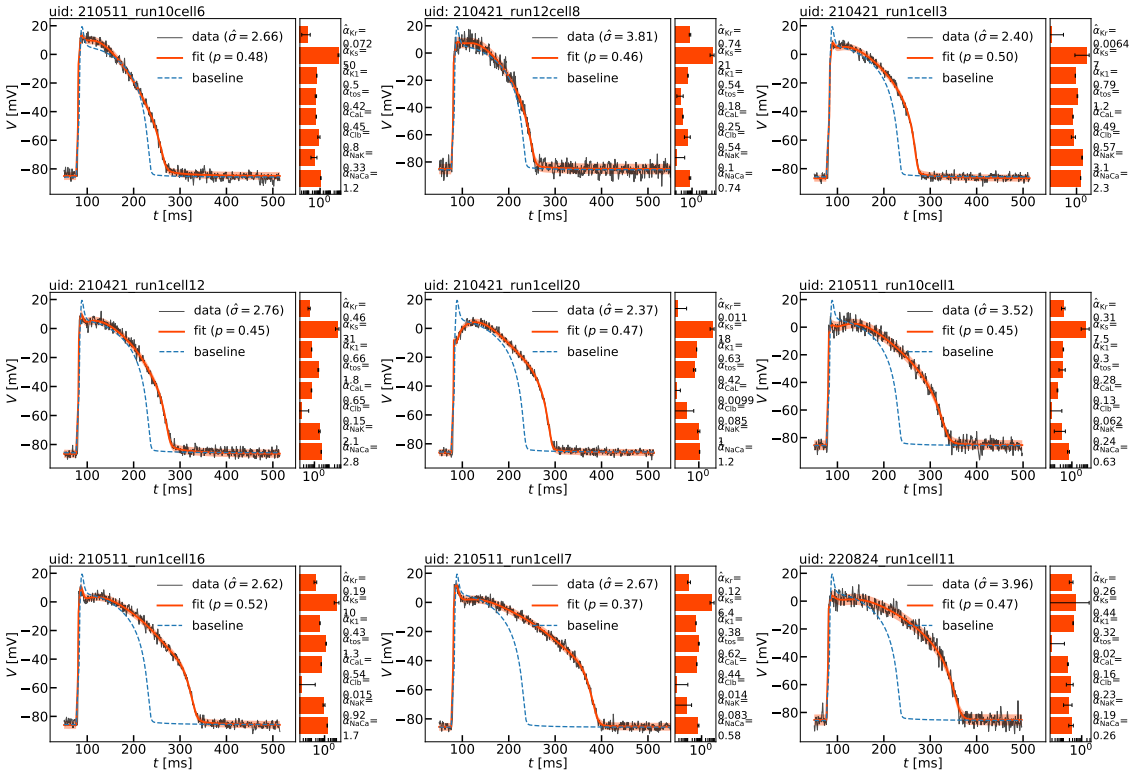

Figure 5.1: Parameter estimation results for nine representative rabbit ventricular myocytes. Each cell is labelled by a unique identifier (uid). The experimentally recorded fluorescence-based AP traces $(t_j, V_j), j = 1, .., 5000$ are displayed as thin black curves. The corresponding APs $\hat{V}(t)$ generated by the calibrated Shannon model (equation (4.1)) are shown as thick orange–red curves. The estimated standard deviation of the measurement noise, $\hat{\sigma}$, is reported in the legend and visualised by the width of the semi-transparent orange–red bands centred on $\hat{V}(t)$. For each cell, the inferred parameter values $\hat{\boldsymbol{\alpha}}$ and their associated standard errors $\boldsymbol{\sigma}_{\hat{\boldsymbol{\alpha}}}$, obtained from equations (5.5) and (5.6), are presented in accompanying bar charts. Goodness-of-fit p values computed using equation (5.9) are listed in the legends. For reference, the AP waveform of the baseline Shannon model, $\hat{V}(t)$, is included as a blue dashed curve.

stimulus-induced depolarisation. Consequently, the present study focuses on fitting the secondary repolarisation phase of the AP. Numerical solution of Shannon model is obtained by the same procedure stated in Section 4.2.1.

5.2.4 Estimands and Optimization Details

Due to the high dimensionality of the parameter space, it is computationally infeasible to include all 179 parameters of the Shannon model in the parameter estimation problem (equation (5.5)). In this work, the majority of model parameters are held fixed at their baseline values, and parameter estimation is restricted to a reduced subset comprising eight most influential parameters based on the ranking in 4.9, together with the standard deviation of the measurement noise. Specifically, the parameter vector is defined as

$$\boldsymbol{\Theta} = [\alpha_{\text{Clb}}, \alpha_{\text{Kr}}, \alpha_{\text{K1}}, \alpha_{\text{CaL}}, \alpha_{\text{NaCa}}, \alpha_{\text{Ks}}, \alpha_{\text{NaK}}, \alpha_{\text{tos}}, \sigma]^{\text{T}} \in \mathbb{R}^9. \tag{5.14}$$

These parameters were selected based on a previously published sensitivity analysis of the Shannon model stated in Chapter 4, which identified them as having the greatest influence on AP characteristics [1].

The maximisation of the log-likelihood function defined in equation (5.4), corresponding to the optimisation problem in equation (5.5), is carried out using the covariance matrix adaptation evolution strategy (CMA-ES) [83] introduced in Section 3.4. The algorithm is employed via its implementation in the Python package `PINTS` [85].

The algorithm operates by iteratively evolving a population of candidate parameter vectors drawn from a multivariate Gaussian distribution characterised by a mean vector and a covariance matrix. Starting from an initial guess, the likelihood of each candidate is evaluated by simulating the Shannon model and comparing the resulting AP waveform with the experimentally recorded voltage trace through the likelihood function. A subset of the most likely candidates is then selected, and the distribution parameters are updated to shift the sampling towards regions of higher likelihood in parameter space.

This process of sampling, selection, and distribution update is repeated until convergence criteria are satisfied. In this study, the initial population consists of 96 candidate solutions, with initial means set to unity, corresponding to the baseline parameter values of the Shannon model, and diagonal covariance matrices with variances of 16.66. These variance values correspond to one-sixth of the prescribed parameter search ranges, which were uniformly defined as $[10^{-4}, 10^{2}]$ for all parameters. Optimisation is terminated when the relative change in the parameter estimates remains below 10^{-6} over the final 100 iterations.

5.3 Results and Discussion: Parameter Estimation on Rabbit Ventricular Myocytes

In this section I will describe the resulting population of cell-specific AP models obtained by calibrating the Shannon et al. [3] ventricular myocyte model to voltage-sensitive fluorescence recordings from rabbit ventricular myocytes.

5.3.1 Demonstration for Parameter Estimation Procedure

To demonstrate the parameter inference procedure on representative examples, I first consider a subset of nine rabbit ventricular myocytes. Figure 5.1 presents a comprehensive visualization comprising: (i) the experimentally recorded AP waveforms for individual cells, (ii) the corresponding accepted model fits together with their goodness-of-fit values, (iii) the inferred parameter estimates and associated standard errors, and (iv) a direct comparison between the fitted models and the baseline Shannon model for each of these representative myocytes.

5.3.1.1 Features of Experimental Waveforms

As with all excitable cells, ventricular myocytes generate APs characterized by large, transient deviations from the electrochemical equilibrium maintained across the sarcolemma [4]. A representative example of the canonical ventricular AP morphology is provided by the voltage trace $\check{V}(t)$ obtained from the baseline Shannon model, shown in Figure 5.1. While the experimentally recorded waveforms $V_j(t)$ exhibit qualitatively similar dynamics, several notable differences are evident.

Most prominently, the experimentally measured APs are systematically prolonged relative to the baseline model, as quantified by the AP duration measured at 90% repolarization A_{90}. This trend is observed not only in the illustrative examples shown in Figure 5.1, but across the majority of the 1180 recorded biological cells. The metric A_{90} is defined as the time interval between the depolarization upstroke and the subsequent repolarization downstroke at 90% of the AP amplitude, with alternative durations A_x defined analogously.

A further distinguishing feature of the experimental traces $V_j(t)$ is the absence of pronounced initial voltage spikes and the presence of only weak post-upstroke notches. In some cases, such as the waveform recorded from cell `uid:210421_run1cell20`, an initial spike is entirely absent. This behaviour can be interpreted as a rapid subthreshold but comparatively slow suprathreshold response to the applied excitation stimulus [116]. For such cells, the stimulus current may be insufficient in amplitude or duration to fully activate the fast sarcolemmal sodium current $I_{\mathrm{Na,SL}}$, while remaining

adequate to engage slower inward currents. As a consequence, the membrane voltage approaches the quasi-stable plateau manifold from below rather than via a classical overshooting upstroke.

The systematic lack of spikes in the experimental APs motivated a reduction of the baseline value of the sodium reversal potential $E_{\mathrm{Na,SL}}$ to -15 mV, as discussed in Section 5.2.3. This modification enables improved agreement between simulated and measured waveforms while having negligible impact on other electrophysiological properties of the baseline model, as demonstrated in Figure 5.2. Figure 5.2 illustrates that reducing the sarcolemmal sodium reversal potential $E_{\mathrm{Na,SL}}$ primarily alters the early depolarization phase of the AP by reducing the fast sodium current I_{Na}, thereby suppressing the pronounced voltage spike present in the original Shannon model. This adjustment improves qualitative agreement with experimentally recorded fluorescence waveforms, which typically lack sharp upstroke spikes. Importantly, the modification has minimal impact on the plateau and repolarization phases of the AP and induces only negligible changes in the eight ionic currents, the conductance parameters of which are selected for calibration. As demonstrated in panels (b) and (c), the relative magnitudes of these currents are largely preserved. This supports the interpretation that the change in $E_{\mathrm{Na,SL}}$ functions as a phenomenological correction for uncertainties in effective stimulation conditions, without materially affecting the electrophysiological mechanisms governing ventricular repolarization or the subsequent parameter estimation results.

5.3.1.2 Effect of Noise

The level of noise varies substantially across individual cells, as illustrated by the representative examples in Figure 5.1. Noise fluctuates much faster than the slow dynamics of the AP trajectory, such as those governing the plateau phase and resting potential, yet comparable to the rapid time scale of the depolarisation upstroke. As a consequence, noise acts predominantly transverse to the slow manifold of the AP, complicating the accuracy of membrane voltage during the plateau and near resting equilibrium without the use of extended temporal averaging. Similarly, waveform features whose temporal scales and amplitudes are similar to those of the noise cannot

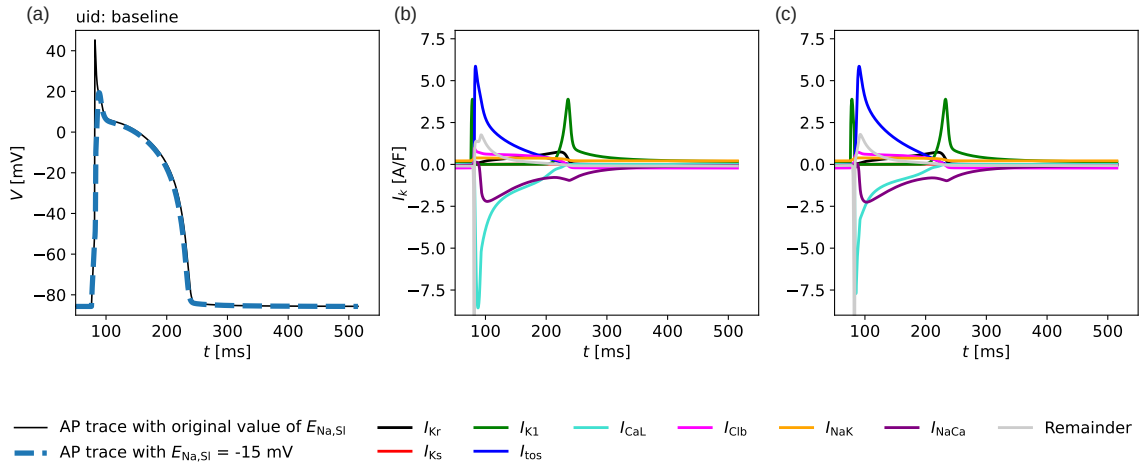

Figure 5.2: Effects of reducing the reversal potential $E_{\mathrm{Na,SL}}$ of the sarcolemmal sodium current from its original value reported by Shannon [3] to -15 mV. Panel (a) compares the AP waveforms generated by the baseline Shannon model using the original value of $E_{\mathrm{Na,SL}}$ (thin black line) and the modified value $E_{\mathrm{Na,SL}} = -15$ mV (thick blue dashed line). Panels (b) and (c) display the corresponding ionic current components $I_k(t)$ for the original and modified models, respectively, with colours defined in the figure legend. At peak activation, the aggregate "remainder" current is dominated by the fast sodium current I_{Na}, reaching amplitudes of -338.7 A/F in panel (b) and -73.5 A/F in panel (c). These peak values lie outside the plotted ordinate ranges and are therefore omitted for visual clarity.

be reliably extracted, since time-averaging is not feasible in these regions. AP spikes, along with post-spike notches, leads to considerable uncertainty in the estimation of peak voltage. Conversely, processes that evolve on faster time scales and exhibit amplitudes well above the noise level, such as the depolarisation upstroke and A_{90}, are comparatively robust and can be estimated with greater accuracy.

Additional characteristics of the experimental noise are illustrated in Figure 5.3. Panel (a) displays the distribution of residuals between the experimentally measured voltage and the model predicted voltage across all time points $\{e_j = \mathcal{V}_j - \hat{V}(t_j),\ j = 1, \ldots, 5000\}$. The sample mean deviates only marginally from zero, an effect due to the finite number of observations ($K = 5000$). The sample standard deviation coincides with the voltage noise standard deviation estimated during the optimisation procedure. A Gaussian distribution with these values provides an excellent fit to the observed histogram, supporting the assumption of normally distributed measurement errors.

Panel (b) shows the autocorrelation of the voltage residuals, quantified by Pearson's correlation coefficient computed between residual values at time t and t+Lag Δt. Noticeable correlations are observed over approximately 10-13 consecutive time steps, indicating that the assumptions of independence and identical distribution of errors are not well satisfied. A more general autoregressive (integrated) moving-average

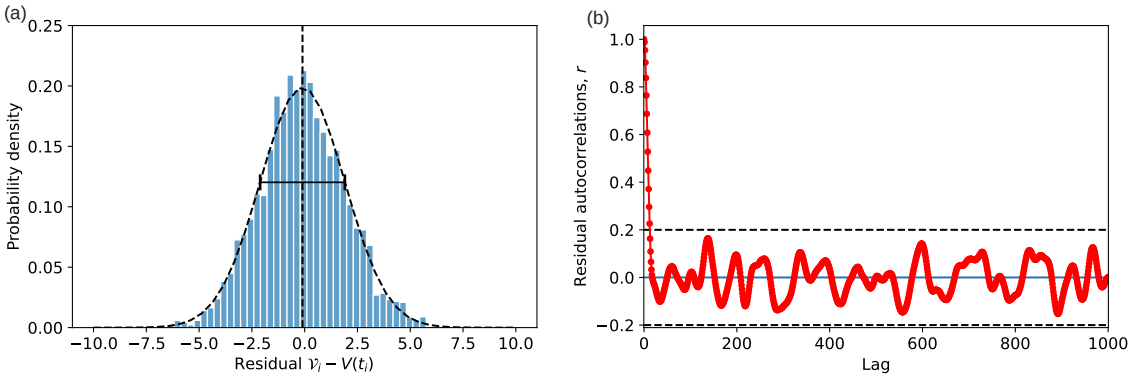

Figure 5.3: Assessment of noise assumptions: normality, independence, and identical distribution. Panel (a) shows the empirical distribution of voltage residuals defined as $e_j = V_j - \hat{V}(t_j)$, for $j = 1, \ldots, 5000$, representing the difference between experimentally measured and model-predicted membrane potentials at each sampling time. The sample mean (0.0021) is indicated by a vertical dashed line, while the sample standard deviation (2.62) is illustrated by a horizontal error bar. A Gaussian probability density function $\mathcal{N}(0.0021, 2.62^2)$, fitted to the residuals, is overlaid as a dashed black curve. Panel (b) presents the temporal autocorrelation of the residuals, quantified using Pearson's correlation coefficient r, computed between residual values at time t and $t + \text{Lag}\,\Delta t$. The reference time point is chosen during the plateau phase of the AP. Data shown in both panels correspond to the representative cell with identifier `uid:210511_run1cell16`.

noise model such as AR(1) may have been more accurate to use potentially to provide a more accurate description of the data. However, such an approach would require the estimation of additional parameters and is therefore left for future work.

5.3.1.3 Fluorescence to Voltage Mapping

Voltage-sensitive fluorescence measurements do not provide absolute values of the transmembrane potential. To convert fluorescence intensity into voltage, a linear mapping was applied in which the time-averaged fluorescence intensity during the plateau phase was mapped to $\check{V}_{\text{plateau}} = 0$ mV, and the time-averaged fluorescence intensity at rest was mapped to $\check{V}_{\text{rest}} = -86$ mV. These values correspond to the plateau and resting membrane potentials of the baseline Shannon model, respectively, as defined earlier.

The plateau phase was chosen for calibration rather than the AP peak, since experimental noise prevents reliable identification of spike amplitudes, as discussed above. The examples shown in Figure 5.1 demonstrate that this procedure produces physiologically consistent AP waveforms suitable for model calibration.

Formally, the fluorescence-to-voltage transformation is given by

$$x(t) = \check{V}_{\text{rest}} + \frac{\check{V}_{\text{plateau}} - \check{V}_{\text{rest}}}{d - c}\big(z(t) - c\big), \tag{5.15}$$

where $z(t)$ denotes the measured fluorescence trace and $x(t)$ is the corresponding calibrated voltage signal. Here, c and d represent the time-averaged fluorescence intensities measured during the resting and plateau phases of the experimental trace, respectively. This linear rescaling preserves waveform morphology while transferring the signal to physiologically meaningful voltage levels.

5.3.1.4 Model Fits

The accepted fits obtained for the nine representative myocytes are presented in figure 5.1. For each cell, the parameter vector $\hat{\boldsymbol{\Theta}}$ was estimated by maximizing the likelihood function defined in equation (5.4). The inferred parameters are reported as $\hat{\boldsymbol{\alpha}}$ and are visualized using cell-specific bar charts.

Uncertainty in the inferred parameters is quantified by the standard errors $\hat{\boldsymbol{\sigma}}_\alpha$, computed using equation (5.6). These values are shown as error bars superimposed on the bar charts in figure 5.1. Under the assumption that numerical optimization errors are negligible, the reported standard errors reflect uncertainty arising from experimental noise or from modelling choices. The latter includes, in particular, the selection of a limited subset of parameters for estimation within the fixed Shannon baseline model [3]. Encouragingly, for the illustrative subset of cells, six or seven of the eight estimated parameters exhibit consistently small uncertainties on average. Nevertheless, several parameters display comparatively large standard errors across all cells, with the magnitude of uncertainty varying between estimands and between individual myocytes. This behaviour is investigated further in the following Section 5.3.4.

AP waveforms generated by the Shannon model using the inferred cell-specific parameters are overlaid on the corresponding experimental recordings in figure 5.1. The resulting synthetic traces closely reproduce the measured waveforms across all phases of the AP. This qualitative agreement is supported by a formal goodness-of-fit assessment using the statistic defined in equation (5.9). The associated p values, reported in figure 5.1, are close to 0.5 for all nine cells. Since the fitting objective is to minimize the normalized weighted sum of squared residuals χ^2_ν, larger p values will indicate better fits between model and data [115].

The estimated standard deviation $\hat{\sigma}$ of the voltage measurements provides a quantitative measure of experimental noise and is inferred simultaneously with the electrophysiological parameters during likelihood maximization. For each cell, the corresponding noise level is illustrated in figure 5.1 by semi-transparent bands of width $2\hat{\sigma}$ centred on the model-predicted waveform. When compared to the experimental recordings, these bands accurately reflect the observed amplitude of stochastic fluctuations.

5.3.1.5 Model Prediction for Ionic Currents

The primary role of a mathematical model is to provide a mechanistic representation of a biological system that enables formal analysis and forward prediction beyond what is directly observable experimentally. To illustrate this principle, I examine the time courses of the individual ionic currents predicted by the cell-specific Shannon models for the nine representative myocytes shown in Figure 5.1. These currents, already denoted I_k in Table 4.1, correspond to the full set of transmembrane ionic fluxes included in the Shannon model, including potassium, sodium, calcium, and chloride currents. In this study, I only foucus on the eight currents related with calibrated parameters while the sum of other currents are labelled as 'Remainder' current.

Notably, several ionic currents that were not included among the calibrated parameters nevertheless contribute to the overall electrophysiological behaviour. However, their net contribution remains small compared with that of the eight conductances selected for estimation, as confirmed by direct inspection of the predicted current traces in Figure 5.4. I note that I_{CaL} and I_{NaCa} can be very low or very high at the AP upstroke stage and this reveals substantial cell-to-cell variability in the relative contributions of different ionic mechanisms. At resting potential, the total transmembrane current remains close to zero in all fitted models.

Because ionic currents cannot be measured directly in the present experimental setting, these predictions constitute authentic forward modelling results. More generally, the cell-specific models provide a flexible framework for computing additional physiological quantities that are experimentally inaccessible, including intracellular

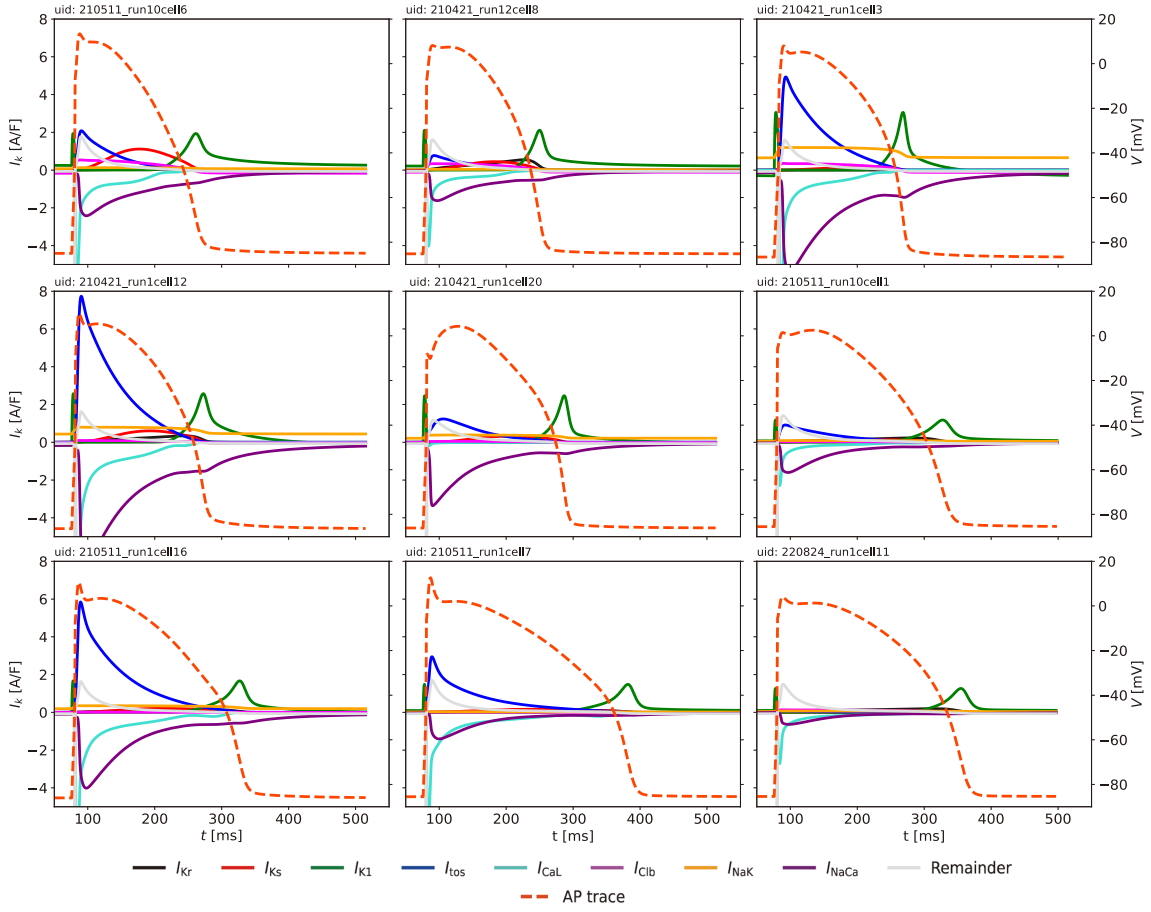

Figure 5.4: Actual currents I_k as functions of time computed from the cell-specific models of the nine myocytes shown in Figure 5.1. Currents are coloured as specified in the figure legend. The corresponding model AP traces are plotted with scales shown on the far ordinate axes..

ion concentration dynamics and responses to altered pacing or pharmacological interventions. Such applications further highlight the value of population-based, cell-resolved modelling approaches and will be explored in future work.

5.3.2 Bayesian Inference Test

To further assess the robustness of the parameter estimation framework described in Section 5.2.1, I performed Bayesian inference on one of of cells presented in Figure 5.1. In contrast to global optimisation, Bayesian inference provides a probabilistic description of parameter uncertainty and offers additional insight into parameter identifiability and uniqueness. Comparable applications combining global optimisation and Bayesian approaches in cardiac electrophysiology modelling have been reported previously in [20].

5.3.2.1 Bayesian Inference Formula and Sampling Settings

Within the Bayesian framework, model parameters are treated as random variables whose probability distributions are updated in light of experimental data according to Bayes' theorem,

$$P(\mathbf{\Theta}|\mathbf{Y}) = \frac{P(\mathbf{Y}|\mathbf{\Theta})\,P(\mathbf{\Theta})}{P(\mathbf{Y})}, \tag{5.16}$$

where a 'prior' probability distribution on the parameters $P(\mathbf{\Theta})$ is assumed from pre-experiment considerations, then modified by the likelihood function $P(\mathbf{Y}|\mathbf{\Theta})$ of equation (5.4) and normalized by the available experimental 'evidence' distribution $P(\mathbf{Y})$ to obtain the 'posterior' probability distribution $P(\mathbf{\Theta}|\mathbf{Y})$. The latter fully describes the estimands and can be used to evaluate any requited moments. In particular, the maximum a posteriori (MAP) estimate and the standard deviation of the posterior can be compared to the 'best' estimate (equation (5.5)) and standard error of estimation (equation (5.6)), respectively.

The posterior is hardly available in closed form, but it can be sampled numerically. I used the Haario-Bardenet adaptive covariance Markov chain Monte Carlo method developed in [117] and implemented in [85] and this is an algorithm for sampling involved high-dimensional distributions. For each cell, five Markov chains were initialized at the best values found by global optimization with addition of a small amount of independent zero-mean Gaussian noise. Chains were run for 10000 steps converging to an average scale reduction factor of 1.08 and producing 50000 samples for each parameter as illustrated in Figure 5.5.

5.3.2.2 Bayesian Sampling Rest Results

Figure 5.6 presents the marginal and joint posterior probability distributions of the inferred parameters for the representative cell (uid:210511_run1cell16). The maximum a posteriori (MAP) estimates obtained from Bayesian sampling, $\hat{\alpha}_k^{\mathrm{bs}}$, are in close agreement with the corresponding point estimates derived from global maximization of the likelihood, $\hat{\alpha}_k^{\mathrm{lm}}$, for all estimands. The largest relative discrepancy is

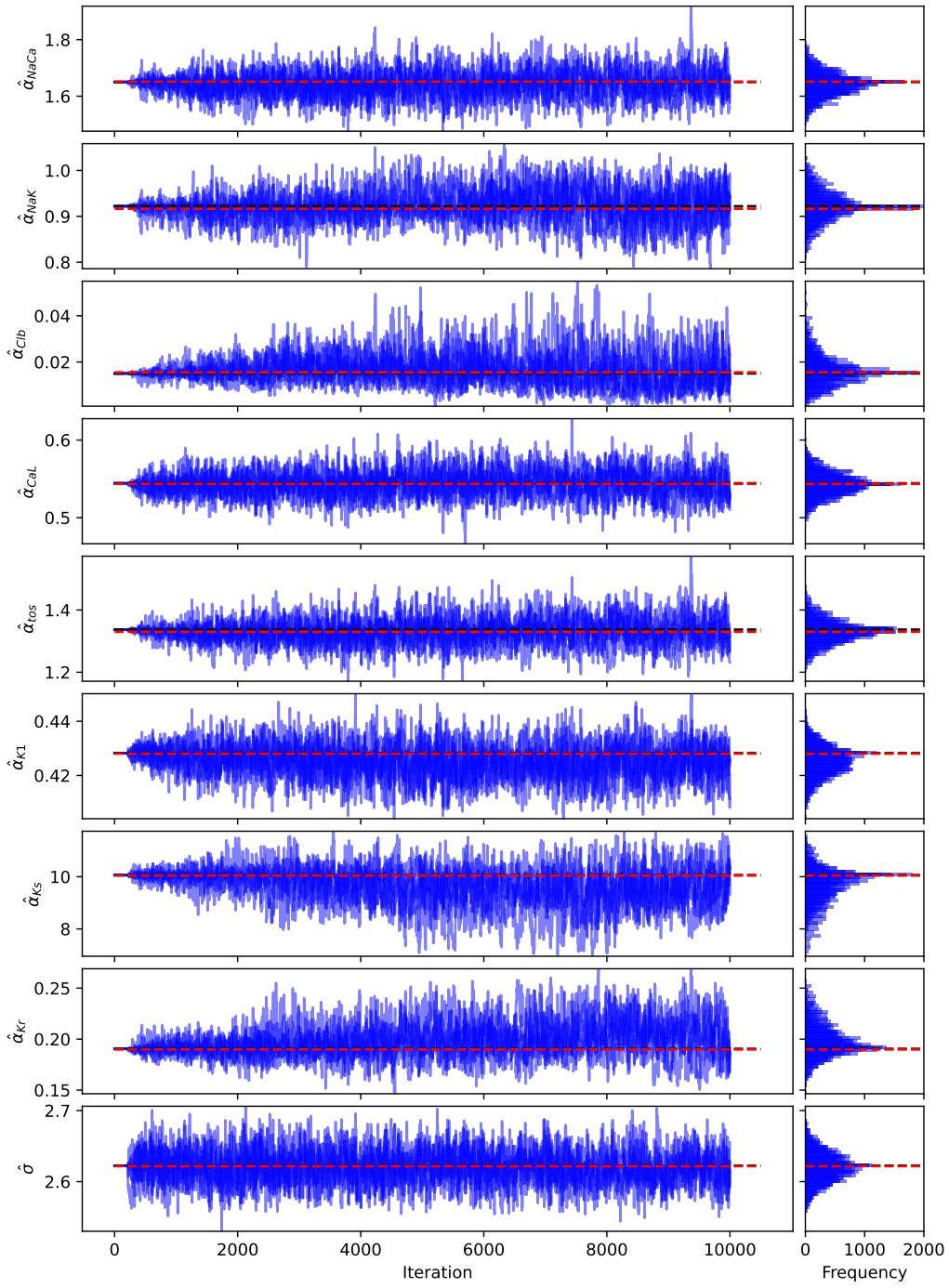

Figure 5.5: Five independent Haario–Bardenet adaptive covariance Markov chain Monte Carlo (MCMC) chains sampling the nine estimands for the representative cell `uid:210511_run1cell16`. Red lines indicate the maximum a posteriori (MAP) parameter estimates, denoted by $\hat{\boldsymbol{\alpha}}_k^{\mathrm{bs}}$, obtained from Bayesian sampling. Black lines indicate the corresponding global maximum-likelihood estimates $\hat{\boldsymbol{\alpha}}^{\mathrm{lm}}$.

uid	$\tilde{\Delta}\hat{\alpha}_{\text{NaCa}}$	$\tilde{\Delta}\hat{\alpha}_{\text{NaK}}$	$\tilde{\Delta}\hat{\alpha}_{\text{Clb}}$	$\tilde{\Delta}\hat{\alpha}_{\text{CaL}}$	$\tilde{\Delta}\hat{\alpha}_{\text{tos}}$	$\tilde{\Delta}\hat{\alpha}_{\text{K1}}$	$\tilde{\Delta}\hat{\alpha}_{\text{Ks}}$	$\tilde{\Delta}\hat{\alpha}_{\text{Kr}}$	$\tilde{\Delta}\hat{\sigma}$
210511run10cell6	-1.36×10^{-3}	1.42×10^{-2}	-7.05×10^{-3}	-2.65×10^{-3}	-9.20×10^{-3}	8.78×10^{-4}	4.70×10^{-3}	1.14×10^{-2}	1.23×10^{-3}
210421run12cell8	-9.12×10^{-3}	-2.74×10^{-2}	6.71×10^{-3}	-1.21×10^{-3}	2.01×10^{-2}	-7.96×10^{-4}	2.10×10^{-3}	8.93×10^{-3}	1.61×10^{-4}
210421run1cell3	1.52×10^{-3}	2.81×10^{-3}	-8.08×10^{-3}	-1.56×10^{-3}	1.72×10^{-3}	-8.54×10^{-4}	-1.05×10^{-2}	1.15×10^{-2}	5.30×10^{-4}
210421run1cell12	-2.12×10^{-3}	-2.75×10^{-3}	1.02×10^{-2}	3.08×10^{-4}	1.36×10^{-3}	-7.93×10^{-4}	-1.22×10^{-3}	6.07×10^{-3}	4.66×10^{-4}
210421run1cell20	-5.51×10^{-4}	7.55×10^{-4}	-3.08×10^{-2}	-3.86×10^{-2}	3.46×10^{-3}	-1.63×10^{-3}	-3.01×10^{-3}	-4.14×10^{-2}	-7.93×10^{-4}
210511run10cell1	-3.26×10^{-4}	1.67×10^{-2}	-3.14×10^{-2}	-2.82×10^{-3}	-1.44×10^{-2}	2.00×10^{-3}	-1.08×10^{-3}	1.65×10^{-3}	6.79×10^{-4}
210511run1cell16	6.06×10^{-4}	6.00×10^{-3}	3.28×10^{-2}	-1.22×10^{-3}	-5.08×10^{-3}	-3.89×10^{-4}	-1.34×10^{-3}	-3.25×10^{-3}	-2.41×10^{-4}
210511run1cell7	-3.96×10^{-3}	2.49×10^{-3}	-7.36×10^{-3}	1.66×10^{-3}	1.21×10^{-3}	-4.53×10^{-4}	1.31×10^{-3}	4.24×10^{-4}	-1.09×10^{-5}
220824run1cell11	-3.91×10^{-3}	1.30×10^{-2}	9.59×10^{-3}	3.15×10^{-3}	3.10×10^{-2}	-1.57×10^{-3}	-1.90×10^{-2}	-5.02×10^{-3}	-1.54×10^{-4}

Table 5.1: Relative differences $\tilde{\Delta}\hat{\alpha}_k = (\hat{\alpha}_k^{\text{bs}} - \hat{\alpha}_k^{\text{lm}})/\hat{\alpha}_k^{\text{lm}}$ between parameter estimates obtained by Bayesian sampling (superscript "bs") and likelihood maximisation (superscript "lm"). The highlighted row corresponds to the cell illustrated in Figure 5.1.

observed for the chloride background conductance,

$$\tilde{\hat{\alpha}}_{\text{Clb}} = \frac{\hat{\alpha}_{\text{Clb}}^{\text{bs}} - \hat{\alpha}_{\text{Clb}}^{\text{lm}}}{\hat{\alpha}_{\text{Clb}}^{\text{lm}}} = 3.2 \times 10^{-2}.$$

The posterior standard deviations are consistently smaller and in many cases substantially smaller than the standard errors of estimation obtained from equation (5.6), as illustrated by their comparison in the diagonal panels of Figure 5.6. This indicates that the actual uncertainty associated with the inferred parameters is lower than the conservative error estimates reported throughout this study.

This discrepancy arises because equation (5.6) is based on an asymptotic linear approximation that is strictly valid only in the limit of infinitely large datasets $\{V_j\}$. Examination of the pairwise marginal posterior distributions reveals negligible correlations for the majority of parameters, providing strong evidence for practical identifiability and uniqueness of the inferred estimates. Moderate correlations are observed between the estimands $\hat{\alpha}_{\text{tos}}$ and $\hat{\alpha}_{\text{NaCa}}$, whose joint posterior distribution exhibits a ridge-like structure, indicating that parameter combinations along this ridge are nearly equally probable. Importantly, even in this case, the MAP estimates $\hat{\alpha}_k^{\text{bs}}$ remain in close agreement with the maximum-likelihood estimates $\hat{\alpha}_k^{\text{lm}}$.

The Bayesian sampling results for the rest of the cells from Figure 5.1 are very similar as shown in Table 5.1 and the largest relative difference is given by $|\tilde{\Delta}\hat{\alpha}_{\text{Kr}}| = 4.14 \times 10^{-2}$ from cell uid:210421_run1cell20. In summary, Bayesian inference confirms the practical uniqueness of the parameter estimates, indicates a smaller parameter uncertainty than that suggested by equation (5.6), and demonstrates excellent consistency with likelihood-based optimisation. Owing to the substantially higher computational cost of Bayesian sampling, this analysis was restricted to a representative

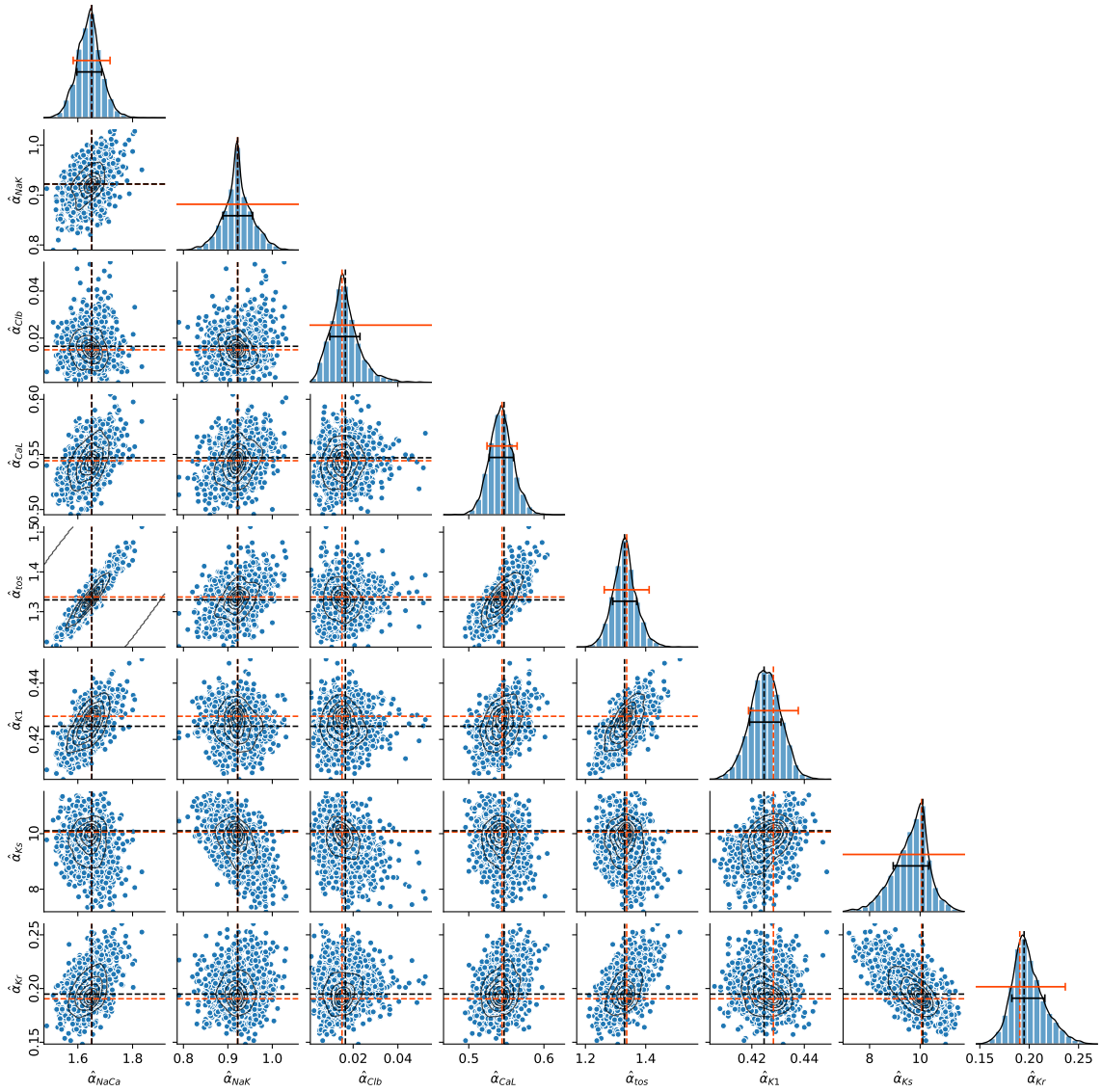

Figure 5.6: Univariate (main diagonal) and pairwise bivariate (lower triangular) marginal posterior distributions of the estimated parameters for the representative cell `uid:210511_run1cell16`. Black dashed lines indicate the maximum a posteriori (MAP) estimates obtained from Bayesian sampling, while orange–red dashed lines denote the corresponding global maximum-likelihood estimates. In the diagonal panels, black error bars represent the posterior standard deviations, and orange–red error bars indicate the standard errors estimated using equation (5.6). Kernel density estimation (KDE) contours are shown throughout to visualise the marginal and joint posterior densities.

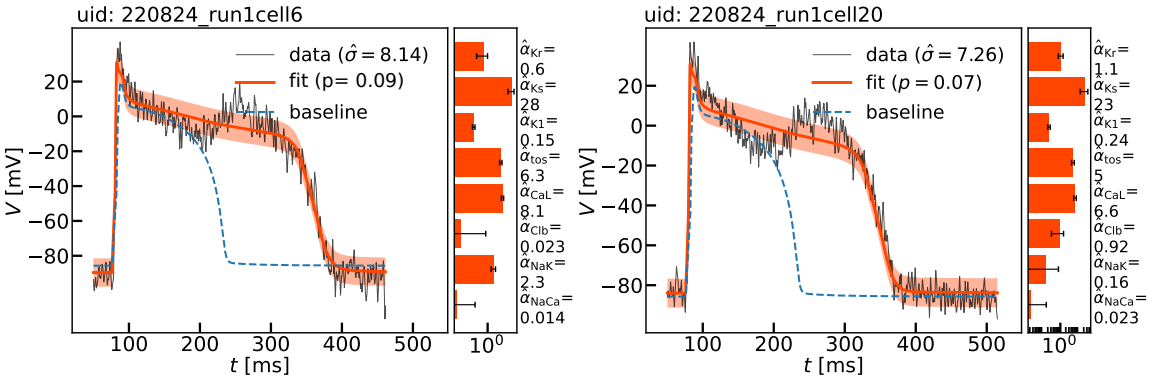

Figure 5.7: Rejected parameter estimation results for two representative rabbit ventricular myocytes with comparatively poor goodness-of-fit values. These AP waveforms exhibit atypical morphologies, particularly during the plateau phase.

subset of myocytes.

5.3.3 Cell-specific Model Population as a Random Sample of a "Healthy Myocyte" Phenotype

AP waveforms recorded from a total of 1228 rabbit ventricular myocytes were subjected to parameter estimation using the Shannon ventricular cell model. Of these, 1180 fitted models satisfied the goodness-of-fit criterion $p > 0.3$ and were therefore retained for further analysis. The threshold value $p = 0.3$ was selected based on visual inspection and comparison with representative high-quality fits illustrated in Figure 5.1, which I consider to reflect acceptable agreement between model and data. The rejected fits were approximately 4% of the population size. The experimental AP traces of the rejected fits featured more pronounced versions of the waveforms of cell uid: 220824_run1cell6 and uid: 220824_run1cell20 from the Figure 5.7 with comparatively poor goodness-of-fit values and were not captured well by the fitting procedure. Notably, these experimental AP traces exhibited atypical morphologies, particularly during the plateau phase, where the waveform shapes differed substantially from the canonical ventricular AP morphology. The full set of accepted parameter estimates defines a population of cell-specific models,

$$\mathcal{M} = \left\{\hat{\boldsymbol{\alpha}}^{(i)}\right\}_{i=1}^{1180},$$

where each parameter vector $\hat{\boldsymbol{\alpha}}^{(i)} \in \mathbb{R}^8$ corresponds to a distinct biological myocyte. Owing to the dimensionality of this parameter space, direct visualization and interpretation of the population as a whole is non-trivial. To formalize this viewpoint, I regard individual cardiomyocytes C_i as realizations of an underlying random variable defined on a sample space Σ representing the phenotype of healthy rabbit ventricular myocytes. The associated fitted model parameters $\hat{\boldsymbol{\alpha}}$ are then treated as realizations of a random variable taking values in a measurable parameter space Ω. Now I can then use $\mathcal{M}$ to represent a random sample from the probability distribution of the random variable $\Sigma : \mathcal{F} \to \Omega$, while ourparameter estimation process plays the role of the map $\mathcal{M}$.

5.3.3.1 The Cell-specific Model Population

The ensemble of accepted parameter vectors $\mathcal{M}$ provides a finite sample from which statistical properties of the underlying parameter distribution $P(\boldsymbol{\Theta})$ may be inferred. Estimates of this distribution are presented in Figure 5.8 which summarise the data in one and two dimensions respectively. A striking feature of the inferred population is the extent of parameter variability: several parameters span multiple orders of magnitude across the population, with $\hat{\alpha}_{\mathrm{Ks}}$ in particular varying over approximately four orders of magnitude. This level of heterogeneity contrasts sharply with the comparatively narrow parameter ranges typically assumed in many modelling studies, where conductances are often varied only around baseline values [6].

To reveal specific features of the inferred distributions, univariate marginal distributions of all fitted parameters are shown along the main diagonal of Figure 5.8. These are displayed as histograms supplemented with Gaussian kernel density estimates. With the exception of $\hat{\alpha}_{\mathrm{K1}}$, $\hat{\alpha}_{\mathrm{CaL}}$, and $\hat{\alpha}_{\mathrm{NaCa}}$, which exhibit extended lower tails indicative of outlier behaviour at small values, most parameter distributions display clear bimodal structure. This bimodality suggests the presence of distinct subgroups within the population and motivates further investigation of joint parameter dependencies and their electrophysiological implications.

Next in order to examine potential dependencies and clustering among inferred parameters, bivariate joint marginal distributions are visualised in Figure 5.8. These

are presented as scatter plot histograms overlaid with contours obtained from two-dimensional Gaussian kernel density estimation. The plots are organised in a matrix layout in which each row and column corresponds to one of the eight Shannon model parameters, with individual parameters appearing on the vertical axes across rows and on the horizontal axes across columns. Such a representation, commonly referred to as a pairwise plot or correlogram, provides a compact and systematic two-dimensional summary of the multidimensional dataset $\mathcal{M}$.

The distributions shown are marginal in nature, in the sense that all remaining parameters are allowed to vary randomly. Inspection of the pairwise relationships reveals generally weak, if any, linear correlations between the parameter estimands. Direct visualisation of higher-dimensional joint distributions is not feasible. However, the pairplot representation offers an informative projection of the underlying structure of the parameter space. Owing to the symmetry of the pairplot about the main diagonal, the upper triangular portion of Figure 5.8 is used to display complementary information. Specifically, I plot the bivariate joint distributions of the standard errors of parameter estimation $\{\hat{\sigma}_k^{(j)}\}$ for each parameter k and cell j, shown in magenta. Univariate distributions of these standard errors are omitted for clarity.

In contrast to the parameter estimates themselves, the standard errors exhibit pronounced positive linear correlations across parameters, such $(\hat{\sigma}_{\mathrm{Clb}}, \hat{\sigma}_{\mathrm{NaK}})$. This indicates that uncertainty in parameter estimation is shared across parameters, likely reflecting common sources of experimental noise and model sensitivity rather than intrinsic biophysical coupling.

5.3.3.2 Stratification of Parameter Distributions by Rabbit

To investigate whether the estimated parameter distributions reported in Figure 5.8 reflect genuine biological variability or are instead dominated by systematic between-rabbit differences, we stratified the uni-variate marginal distributions of all eight parameter estimands by individual rabbit. Figure 5.9 shows marginal distributions of the eight parameter estimands stratified by rabbit. Overall, the principal qualitative features observed in the pooled population are reproduced within individual rabbits, indicating that the inferred parameter variability is not primarily driven by systematic

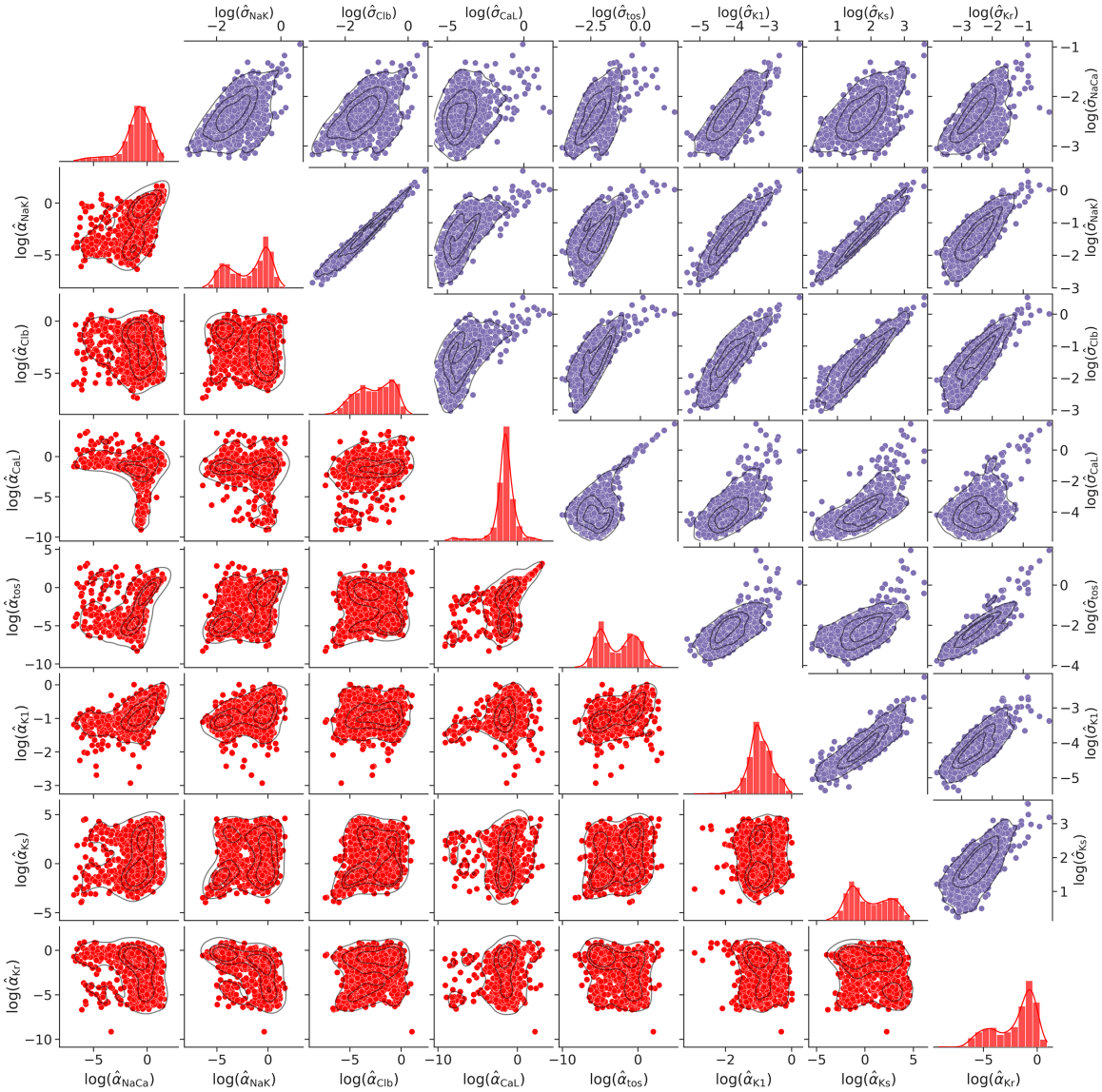

Figure 5.8: Marginal probability distributions of parameter estimands $\hat{\boldsymbol{\alpha}}$ and their estimation errors $\hat{\boldsymbol{\sigma}}$. Pairwise scatter plots of the estimates $\hat{\boldsymbol{\alpha}}$ and of their standard errors $\hat{\boldsymbol{\sigma}}$ are plotted below and above the grid diagonal in red and magenta, respectively, for all 1180 accepted myocyte fits. Single parameter histograms are shown on the grid diagonal in red. Associated marginal kernel density estimations are included throughout. Logarithmic scales are used and log means ln here.

differences between rabbits. At the same time, several notable rabbit-specific patterns emerge.

The most striking observation is the high degree of consistency exhibited by $\hat{\alpha}_{\mathrm{K1}}$. Across all eight rabbits, the distributions occupy a similar range on the log scale and possess comparable widths and modal locations. A similarly high level of conservation is observed for $\hat{\alpha}_{\mathrm{CaL}}$ and $\hat{\alpha}_{\mathrm{NaCa}}$, whose distributions remain broadly aligned across animals despite being somewhat wider than those of $\hat{\alpha}_{\mathrm{K1}}$. These findings suggest that the conductances associated with I_{K1} , I_{CaL} and I_{NaCa} are tightly constrained within healthy rabbit ventricular myocytes and exhibit relatively limited variability.

In contrast, several estimands display pronounced bimodality within individual

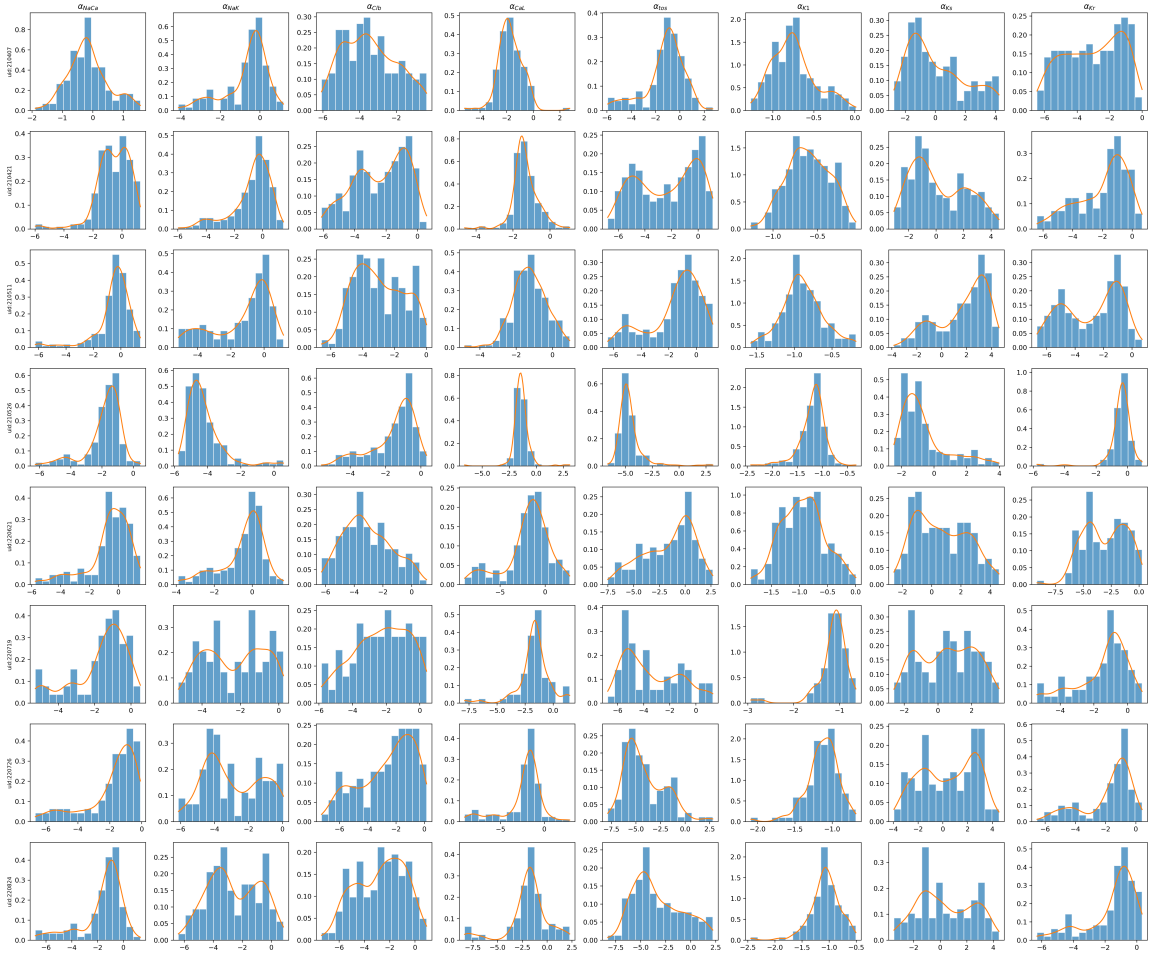

Figure 5.9: Uni-variate marginal distributions of parameter estimands $\hat{\alpha}_k$ stratified by individual rabbit. Each row corresponds to one of the eight rabbits identified by their recording identifier (left margin), and each column corresponds to one of the eight Shannon model parameter estimands $\hat{\alpha}_k$ as labelled across the top. Within each panel, the blue histogram shows the normalised frequency of $\log(\hat{\alpha}_k)$ values and the orange curve is the associated kernel density estimate. Logarithmic scales are used and log means ln here.

rabbits. This behaviour is most evident for $\hat{\alpha}_{\mathrm{NaK}}$, $\hat{\alpha}_{\mathrm{Clb}}$, $\hat{\alpha}_{\mathrm{Ks}}$ and $\hat{\alpha}_{\mathrm{Kr}}$, for which two distinct modes are visible in many rabbits. Importantly, the bimodal structure persists after stratification and is therefore not an artefact of pooling data from multiple rabbits. Rather, the results suggest that the underlying myocyte population within a single heart may itself be heterogeneous. Such heterogeneity could arise from differences in cellular phenotype, transmural location, or calcium-handling state, all of which are known to influence ventricular electrophysiology.

Despite this general pattern, one rabbit, uid:210526, appears qualitatively distinct from the remainder of the cohort. For this rabbit, several parameter distributions that are bimodal in other rabbits become strongly concentrated and approximately unimodal. This effect is particularly evident for $\hat{\alpha}_{\mathrm{NaK}}$, $\hat{\alpha}_{\mathrm{CaL}}$, $\hat{\alpha}_{\mathrm{tos}}$ and $\hat{\alpha}_{\mathrm{Kr}}$, whose distributions are considerably narrower than those observed elsewhere. The data therefore suggest a comparatively homogeneous myocyte population and the presence

of this rabbit demonstrates that the extent of within-heart heterogeneity can itself vary between rabbits.

The largest inter-rabbit differences are observed for $\hat{\alpha}_{\text{tos}}$ and $\hat{\alpha}_{\text{Ks}}$. For $\hat{\alpha}_{\text{tos}}$, several rabbits exhibit broad or bimodal distributions, whereas others show a dominant peak at small values with only a weak secondary component. The parameter $\hat{\alpha}_{\text{Ks}}$ remains highly dispersed in every rabbit, spanning multiple orders of magnitude and displaying appreciable shifts in modal position between rabbits. This broad spread is consistent with the weak identifiability of I_{Ks} inferred elsewhere in the study.

Taken together, the stratified distributions support two main conclusions. First, the principal features of the inferred parameter distributions, including the widespread bimodality of several estimands, are present within individual rabbits and therefore represent genuine structure within the ventricular myocyte population rather than an artefact of pooling data across hearts. Second, although rabbit-specific differences are clearly detectable, particularly for $\hat{\alpha}_{\text{tos}}$ and $\hat{\alpha}_{\text{Ks}}$, these differences are generally modest relative to the substantial variability observed within each rabbit. Consequently, the pooled population-level distributions provide a representative description of healthy rabbit ventricular myocytes, while the stratified analysis reveals an additional layer of biologically meaningful rabbit-to-rabbit variability.

5.3.3.3 Multivariate Linear Regression Models of AP Biomarkers as a Function of Eight Estimands

Mathematical models provide an explicit mapping between internal model parameters and physiological observables. At the population level, this relationship can be explored by examining how commonly reported AP biomarkers depend on the inferred model parameters. Among the many quantities that can be evaluated using the constructed cell-specific Shannon models, I focus here on the AP durations at 90% , 50% and 30% repolarization, A_{90} , A_{50} and A_{30}, respectively, which are widely used metrics in cardiac electrophysiology.

To facilitate comparison between biomarkers with different absolute scales, AP

biomarkers were standardized using the z-score transformation

$$z(b) = \frac{b - \mu}{\sigma},$$

where μ and σ denote the mean and standard deviation of the biomarker values across the cell population. As with the high-dimensional parameter space itself, direct visualization of the dependence of AP biomarkers on all eight estimands simultaneously is not feasible. Consequently, any relationships examined must be interpreted as marginal dependencies, in the sense that while one or two parameters are explicitly represented, all remaining estimands vary simultaneously across the population. Inspection of the marginal relationships reveals no simple functional form and, in particular, no strong linear dependence between either biomarker and any single parameter, as shown in Figure 7 of [2].

Motivated by this observation, and by earlier studies in related cardiac electrophysiology models, I constructed multivariate linear regression models expressing AP biomarkers as functions of all eight inferred parameters. The results of these regressions, together with the corresponding univariate fits, coefficients of determination, and statistical significance measures, are provided in Figure 5.10 and Table 5.2. While the multivariate linear models substantially outperform univariate regressions, achieving coefficients of determination of approximately $R^2 \approx 0.6$ compared with $R^2 \approx 0.1$ for univariate fits, the quality of these fits remains only moderate.

These results indicate that linear regression models, even when multivariate, are unable to fully capture the complex and nonlinear dependence of AP biomarkers on the underlying electrophysiological parameters. In contrast, the cell-specific Shannon models provide near-exact reproduction of experimentally measured biomarker values on a cell-by-cell basis. This highlights the key advantage of the present modelling framework that rather than relying on low-dimensional statistical surrogates, the calibrated mechanistic models retain the full nonlinear structure required for accurate prediction of individual cellular behaviour.

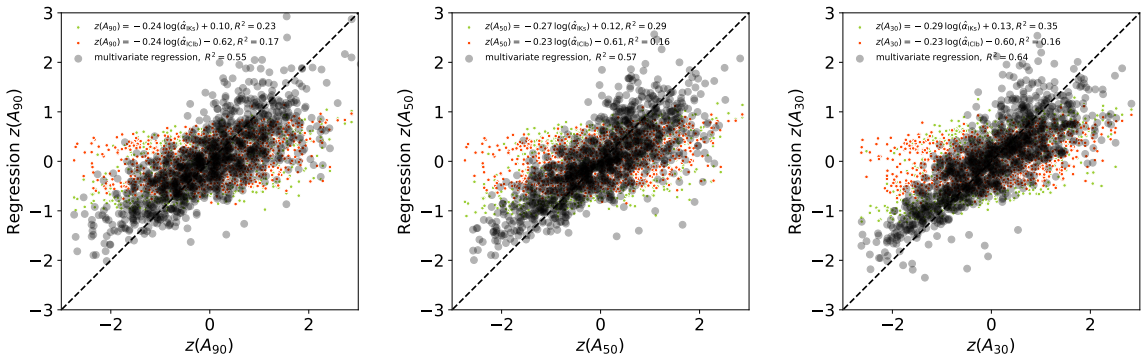

(a) Biomarker A_{90} **(b)** Biomarker A_{50} **(c)** Biomarker A_{30}

Figure 5.10: Comparison of multivariate and uni-variate regression fits of selected biomarkers (on ordinates) with their experimental values (on abscissas). Multivariate regressions are plotted with large scatter points, uni-variate regressions with small scatter points, further specified in the legends. The $y = x$ dashed line denotes perfect agreement. The type of fit and the specific biomarkers are indicated in the legends and as axes labels. Values for the coefficient of determination R^2 of the fits are also stated in the legends. Regression coefficients for the multivariate fits are given in Table 5.2. The p values for statistical significance of the linear relationships, computed from t-tests (uni-variate cases) or f-tests (multivariate cases), are less than 0.001 in all cases. The uni-variate linear regressions are a subset of those plotted in Figure 7 of [2].

	β_{NaCa}	β_{NaK}	β_{Clb}	β_{CaL}	β_{tos}	β_{K1}	β_{Ks}	β_{Kr}	c
$z(A_{90})$	-6.87e-2	3.07e-2	-9.68e-2	-1.86e-1	1.46e-1	-4.47e-1	-2.72e-1	-1.32e-1	-7.40e-1
$z(A_{50})$	-8.02e-2	4.68e-2	-9.68e-2	-2.07e-1	1.19e-1	9.60e-2	-2.93e-1	-9.76e-2	-2.40e-1
$z(A_{30})$	2.24e-2	4.27e-2	-9.74e-2	-2.48e-1	2.11e-2	3.10e-1	-2.94e-1	-6.25e-2	-2.00e-1

Table 5.2: Coefficients β_k and intercepts c for multivariate linear regression models $z(A) = c + \sum_k \beta_k \log(\hat{\alpha}_k)$ of the standard z-scores of biomarkers $z(A_{90})$, $z(A_{50})$, and $z(A_{30})$, plotted in Figure 5.10.

5.3.3.4 Prediction of Intracellular Calcium Biomarkers

Cardiac myocyte contraction is initiated by a transient elevation of intracellular calcium concentration. Using these models, I computed four intracellular calcium biomarkers for each accepted cell-specific model. Summary statistics and population ranges of predicted values for all 1180 cells are presented in Table 5.3.

The predicted end diastolic and peak systolic intracellular calcium concentrations fall within experimentally reported physiological ranges [118, 119, 120]. Moreover, all calcium biomarkers exhibit values comparable to those obtained from the baseline Shannon model, which itself represents a synthesis of experimental observations across multiple studies [3]. Example intracellular calcium dynamics corresponding to inferred AP waveforms are illustrated in the accompanying Figure 5.3, demonstrating that the calibrated models produce physiologically reasonable calcium dynamics despite calcium not being used as a fitting target.

Together, these results highlight the ability of cell-specific models, calibrated solely to voltage recordings, to generate meaningful predictions of unobserved intracellular

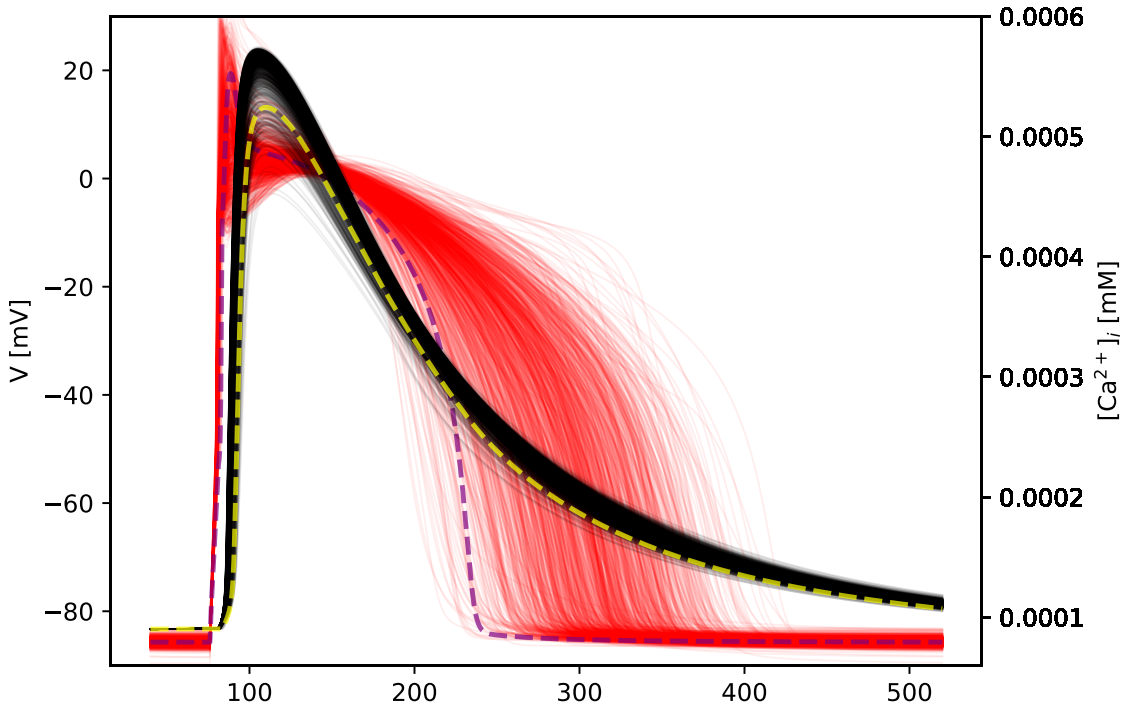

Figure 5.11: Forward prediction of APs and intracellular calcium dynamics using cell-specific inferred parameters. For each example cell, AP waveform simulated using inferred parameters is shown in red, with the corresponding predicted intracellular calcium concentration $[Ca^{2+}]_i$ shown in black. For comparison, simulations obtained using the Shannon baseline model are overlaid, with the baseline AP shown in purple and the baseline intracellular calcium trace in yellow.

processes. Additional model-derived quantities may be readily evaluated within this framework as required.

Marker	Count	Mean	Std	Min	25%	50%	75%	Max	Baseline	Exp. range	References
ED (mM)	1180	1.14e-4	6.00e-6	1.00e-4	1.12e-4	1.15e-4	1.17e-4	1.52e-4	1.02e-4	(8e-5, 2.5e-4)	[118, 119]
PSV (mM)	1180	5.56e-4	1.90e-5	4.52e-4	5.50e-4	5.62e-4	5.69e-4	5.75e-4	5.24e-4	(4.4e-4, 1.6e-3)	[118, 119, 120]
t_{peak} (ms)	1180	3.06e1	1.29	2.81e1	2.98e1	3.04e1	3.10e1	3.76e1	3.41e1	—	—
D_{50} (ms)	1180	1.15e2	1.46	1.03e2	1.15e2	1.15e2	1.16e2	1.19e2	1.15e2	—	—

Table 5.3: Sample statistics for selected $[Ca^{2+}]_i$ biomarkers. (The corresponding values for the baseline Shannon model and ranges derived from experimental data with associated references are listed in the last two columns for comparison.) The following abbreviations are used: ED, $[Ca^{2+}]_i$ at the end of diastole; PSV, peak systolic value of $[Ca^{2+}]_i$; t_{peak}, time from stimulus to peak $[Ca^{2+}]_i$; D_{50}, period of time when $[Ca^{2+}]_i$ remains elevated above a threshold of 50% recovery from the peak value to the resting value, informally "duration at 50% amplitude". Percentages in the column headings denote quartiles of the data.

5.3.4 Uncertainty on Estimates

Within the limitations of the present study, each constructed cell-specific model reproduces its corresponding experimental AP with high fidelity, as demonstrated comprehensively in Figure 5.1. However, it is important to acknowledge that the resulting parameter estimates are subject to additional sources of uncertainty beyond observational noise. These include, but are not limited to, structural model uncertainty, uncertainty in initial conditions, and uncertainties arising from numerical implemen-

tation and experimental protocols [20]. In this section, I will illustrate and attempt to quantify some of these uncertainties.

5.3.4.1 Initial Conditions Uncertainty

A limitation of our study is that parameter estimation is performed using single AP waveforms without explicit prepacing. Prepacing is a procedure by which equation (5.1) is driven into a stable limit cycle through a periodic stimulus, most often in the form of a train of short rectangular current impulses. Prepacing mimics experimental and physiological conditions and serves to reduce uncertainty associated with the choice of initial conditions in problem (5.1).

While the experimental data analysed here were obtained after prepacing by 600 AP trains, it is computationally prohibitive to include such prepacing during the parameter optimisation procedure for all cells. To assess the effect of this discrepancy, I re-fitted nine representative cells while explicitly including prepacing by 600 AP trains.

Figure 5.12 illustrates the effect of prepacing on the simulated AP traces. The black trace corresponds to the experimental waveform, the red trace shows the simulation using parameter estimates inferred without prepacing ($\hat{\alpha}_i$), and the green trace shows the simulation using estimates inferred with prepacing ($\hat{\alpha}_i^{\text{prep}}$). After 600 prepacing APs, the red trace no longer aligns with the experimental data, demonstrating that parameter estimates obtained without prepacing cannot be used to refit the trace. In contrast, the green trace closely follows the experimental waveform, highlighting the differences between $\hat{\alpha}_i$ and $\hat{\alpha}_i^{\text{prep}}$.

For each parameter $\hat{\alpha}_i$, I computed the ratio

$$\lambda_i = \frac{\hat{\alpha}_i^{\text{prep}}}{\hat{\alpha}_i},$$

where $\hat{\alpha}_i^{\text{prep}}$ denotes the estimate obtained with prepacing and $\hat{\alpha}_i$ the estimate obtained without prepacing. These ratios are reported for each of the nine cells in Table 5.4. The selected cells span a wide range of AP morphologies, from relatively short to relatively long durations, and are therefore assumed to provide representative

coverage of the parameter space.

The mean ratios across the nine cells are

$$\begin{aligned} \lambda_{\text{NaCa}} &= 1.07\text{e+}00, \quad \lambda_{\text{tos}} = 3.20\text{e+}00, \quad \lambda_{\text{NaK}} = 2.48\text{e}{-}01, \quad \lambda_{\text{K1}} = 1.07\text{e+}00, \\ \lambda_{\text{Clb}} &= 5.19\text{e}{-}01, \quad \lambda_{\text{Ks}} = 2.00\text{e}{-}01, \quad \lambda_{\text{CaL}} = 8.22\text{e}{-}01, \quad \lambda_{\text{Kr}} = 2.87\text{e+}00. \end{aligned} \tag{5.17}$$

As a first-order approximation, parameter estimates obtained without prepacing may be converted to corresponding prepaced estimates by multiplying each estimate $\hat{\alpha}_i$ by the appropriate factor λ_i from equation (5.17), for $i \in \{\text{NaCa}, \text{NaK}, \ldots, \text{Kr}\}$. The variability of the ratios λ_i differs substantially between parameters. For example, λ_{K1} and λ_{NaCa} remain relatively close to unity across all cells, whereas parameters such as λ_{Clb}, λ_{Kr}, and λ_{tos} exhibit much larger deviations and variability. A possible biophysical explanation is that the sensitivity of each parameter to prepacing depends on which AP biomarkers it predominantly controls and how strongly those biomarkers are altered after prepacing.

The inward rectifier potassium current I_{K1} primarily regulates the resting membrane potential and terminal repolarisation phase. Since prepacing produces relatively small changes in resting potential, only minor adjustments to α_{K1} are required during optimisation, resulting in values of λ_{K1} close to one. Similarly, α_{NaCa} is most influential on A_{90} according to the sensitivity analysis in Table 4.4. Because prepacing does not substantially alter the overall duration of the AP in these cells, the corresponding values of λ_{NaCa} also remain relatively close to unity.

In contrast, α_{Kr} has a large total-order sensitivity index for V_{plt}, while α_{tos} strongly influences V_{max}, and α_{Clb} influences multiple AP biomarkers. These AP features change more substantially after prepacing. Consequently, larger compensatory changes in α_{Kr}, α_{tos}, and α_{Clb} are required after prepacing, leading to values of λ_i further from unity.

In a word, this limitation is due to the computational cost of optimisation. A large number of wrong "candidate" models must be evaluated in the search for the best fit. For a single cell the CMAES algorithm "evolves" 96 candidate models over approx 800 generations to convergence. This requires 96 x 800 = 76,800 model evaluations. Each evaluation consists of a high-fidelity numerical time integration of an initial

value problem for a set of 39 coupled stiff ordinary differential equations given by the Shannon model. Now, if I attempt to reach a steady state and simulate a train of 600 APs, I will need 600 × 76,800 = 46,080,000 model evaluations per single cell, which is prohibitively expensive.

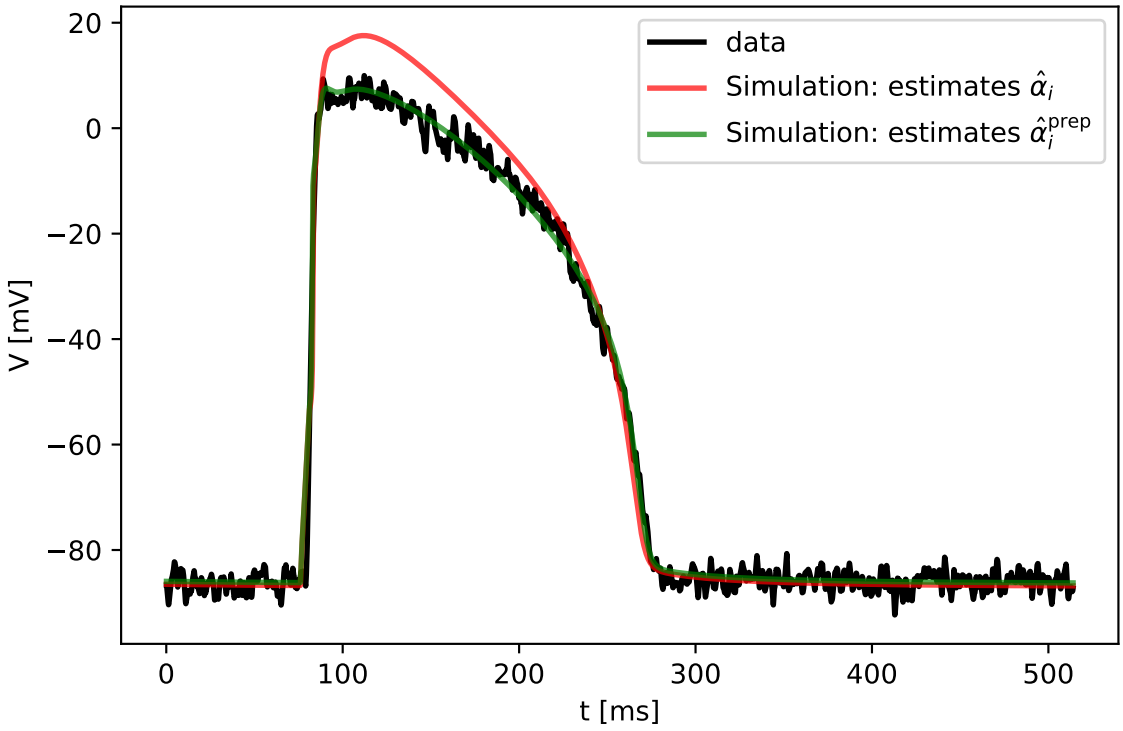

Figure 5.12: Experimental AP trace (black) compared with simulations after 600 prepacing APs. The red trace shows the simulation using parameters inferred without prepacing ($\hat{\alpha}_i$), which no longer fits the experimental trace. The green trace shows the simulation using parameters inferred with prepacing ($\hat{\alpha}_i^{\text{prep}}$), which closely follows the experimental trace, highlighting the differences between $\hat{\alpha}_i$ and $\hat{\alpha}_i^{\text{prep}}$.

uid	λ_{NaCa}	λ_{NaK}	λ_{Clb}	λ_{CaL}	λ_{tos}	λ_{K1}	λ_{Ks}	λ_{Kr}	λ_{σ}
210511run10cell6	1.37e+00	6.44e-02	5.68e-01	1.00e+00	4.98e+00	1.04e+00	5.72e-01	6.86e+00	1.00e+00
210421run12cell8	1.37e+00	1.63e-01	5.05e-01	8.75e-01	5.50e+00	9.69e-01	1.21e-01	1.55e+00	9.99e-01
210421run1cell3	1.09e+00	3.62e-01	1.13e-02	8.77e-01	3.46e+00	1.16e+00	3.38e-02	2.47e+00	9.79e-01
210511run10cell1	8.25e-01	3.54e-01	2.76e-01	7.22e-01	1.38e+00	9.80e-01	3.35e-01	1.11e+00	1.00e+00
210511run1cell16	9.41e-01	1.27e-01	2.32e-01	7.21e-01	2.50e+00	1.17e+00	1.75e-02	9.16e-01	1.04e+00
210511run1cell7	1.01e+00	1.54e-01	3.54e-01	8.75e-01	2.87e+00	1.04e+00	3.80e-02	6.63e-01	1.01e+00
210511run12cell9	3.54e-01	7.61e-02	6.60e-01	4.19e-01	3.59e-01	9.16e-01	5.99e-01	8.93e-01	1.02e+00
210511run16cell23	1.28e+00	1.96e-01	3.78e-02	8.50e-01	4.16e+00	1.10e+00	4.26e-02	2.27e+00	9.89e-01
210511run1cell23	1.40e+00	7.40e-01	2.03e+00	1.06e+00	3.61e+00	1.24e+00	4.21e-02	9.08e+00	9.57e-01
mean $\overline{\lambda}$	**1.07e+00**	**2.48e-01**	**5.19e-01**	**8.22e-01**	**3.20e+00**	**1.07e+00**	**2.00e-01**	**2.87e+00**	**1.02e+00**

Table 5.4: Ratios $\lambda_i = \hat{\alpha}_i^{\text{prep}}/\hat{\alpha}_i$ between parameter estimates obtained with prepacing by 600 APs and those obtained without prepacing, for the nine representative cells shown in Figure 5.1. The final row reports the mean ratios across the nine cells.

5.3.4.2 Procedural Uncertainty

The mapping of fluorescence measurements in Section 5.3.1.3 to membrane potential values is physically motivated but not uniquely defined. To assess the sensitivity of

Estimand	Count	Mean	Std. dev.	$\hat{\alpha}_i$
$\hat{\alpha}_{\mathrm{NaCa}}$	125	1.71e+0	2.69e−1	1.65e+0
$\hat{\alpha}_{\mathrm{NaK}}$	125	7.67e−1	6.01e−1	9.22e−1
$\hat{\alpha}_{\mathrm{Clb}}$	125	9.18e−2	2.38e−1	1.50e−2
$\hat{\alpha}_{\mathrm{CaL}}$	125	5.59e−1	5.78e−2	5.44e−1
$\hat{\alpha}_{\mathrm{tos}}$	125	1.37e+0	2.59e−1	1.34e+0
$\hat{\alpha}_{\mathrm{K1}}$	125	4.43e−1	6.33e−2	4.28e−1
$\hat{\alpha}_{\mathrm{Ks}}$	125	1.02e+1	4.98e+0	1.01e+1
$\hat{\alpha}_{\mathrm{Kr}}$	125	2.41e−1	1.87e−1	1.90e−1

Table 5.5: Uncertainty due to fluorescence-to-voltage mapping. The mapping was varied randomly as described in the text, and cell `uid: 210511_run1cell16` was refitted 125 times. Columns three and four report the mean and standard deviation of the inferred parameters across these refits. The final column lists the reference estimates obtained using the nominal mapping of $V_{\mathrm{rest}} = -86\,\mathrm{mV}$ and $V_{\mathrm{plateau}} = 0\,\mathrm{mV}$.

the inferred parameters to this modelling choice, I repeated the parameter estimation procedure for cell `uid: 210511_run1cell16` a total of 125 times. In each repetition, the reference values of V_{rest} and V_{plateau} were randomly sampled from normal distributions with means of $-86\,\mathrm{mV}$ and $0\,\mathrm{mV}$, respectively, and standard deviations of $1\,\mathrm{mV}$. Sample statistics of the resulting parameter estimates are reported in Table 5.5. The mean values of the inferred parameters remain close to those obtained using the nominal mapping of $-86\,\mathrm{mV}$ and $0\,\mathrm{mV}$, indicating that the estimation procedure is robust to small perturbations in the voltage calibration.

5.3.5 Validation by Predicting Drug Response to 3 nM Dofetilide

In the research work above, the estimation of ion channel conductances from AP recordings is inherently subject to several well-known limitations of nonlinear inverse problems in biophysical models. In particular, the non-uniqueness of the parameterisation of detailed ionic models, dependence on fixed model assumptions such as initial conditions and ionic concentrations, sensitivity to the chosen electrophysiological model, and structural simplifications of channel kinetics may all influence the inferred conductance values. Consequently, achieving accurate waveform fits alone does not guarantee that the estimated parameters are physiologically meaningful or

predictive beyond the calibration setting. For this reason, I validate the inferred parameters using an independent pharmacological perturbation, assessing whether the fitted models can correctly predict the AP duration response to selective I_{Kr} block by dofetilide. This will provide a stringent and mechanistically relevant test of the inferred conductances, particularly α_{Kr}, and helps establish the predictive value of the modelling framework.

Dofetilide can only be administered using an organic solvent vehicle. In this test, dimethyl sulfoxide (DMSO) was used at a concentration of 0.05% in conjunction with dofetilide. DMSO is not expected to exert selective effects on individual ion channels and therefore cannot be explicitly represented within the Shannon electrophysiological model. Nevertheless, non-selective effects of DMSO on cellular electrophysiology cannot be excluded. As a strong solvent, DMSO may compromise membrane integrity, leading to increased leak currents. In addition, electrophysiological properties may be influenced by the incubation periods separating baseline and post-treatment measurements.

To account for these potential confounding effects, control experiments were performed in which cardiomyocytes were exposed to DMSO alone (0.05%) without drug. Cells treated with DMSO-only and those treated with dofetilide plus DMSO were necessarily distinct, since dofetilide binding is effectively irreversible and each cell could therefore be measured at most twice.

I model the observed change in AP duration as a superposition of drug-specific and non-specific contributions,

$$\Delta A_{d+v} = \Delta A_d + \Delta A_v, \tag{5.18}$$

where ΔA_{d+v} denotes the AP duration change relative to baseline following exposure to drug and vehicle, ΔA_v represents the change due to vehicle effects, incubation and other non-specific or random influences, and ΔA_d denotes the drug-induced effect alone. Both ΔA_{d+v} and ΔA_v are experimentally measurable quantities, albeit in different cell populations, whereas ΔA_d cannot be directly isolated experimentally but can be predicted using the Shannon model. The quantity ΔA_v is treated as a

random variable, and consequently ΔA_{d+v} also exhibits stochastic variability.

For each cell j, paired experimental and modelling quantities $\Delta A_{d+v}^{\text{expr}}(j)$ and $\Delta A_{d}^{\text{mod}}(j)$ are available, whereas measurements of $\Delta A_{v}^{\text{expr}}(q)$ are obtained from an unpaired control population of cells $q \neq j$. Under the assumption that both paired and control populations exhibit comparable responses to DMSO and other random influences, the following approximate relationship is expected to hold:

$$f\left(\Delta A_{d+v}^{\text{expr}}(j) - \Delta A_{d}^{\text{mod}}(j)\right) \approx f(\Delta A_{v}^{\text{expr}}(q)), \tag{5.19}$$

where $f[\cdot]$ denotes the probability density function and the superscripts "expr" and "mod" indicate experimental measurements and model predictions, respectively.

Once the pre-drug values of $\hat{\alpha}_{\text{Kr}}$ have been estimated as described previously, the effect of 3 nM dofetilide is modelled as a 15% inhibition of $\hat{\alpha}_{\text{Kr}}$, following earlier studies shown in [55]. The choice of a 15% I_{Kr} block was initially based on the estimate reported by [55], which was therefore adopted as the primary value in this study. However, given the variability in reported levels of I_{Kr} inhibition at 3 nM dofetilide in the literature (Table 1.3), I also explored alternative values within the published range. Among the values examined, a 15% block produced the highest coefficient of determination in the comparison between model-predicted and experimentally measured A_{90} values shown in Figure 5.14.

Figure 5.13 presents a direct comparison between the histograms of $\Delta A_{d+v}^{\text{expr}}(j) - \Delta A_{d}^{\text{mod}}(j)$ and $\Delta A_{v}^{\text{expr}}(q)$. The mean values of the two distributions differ by approximately 2.3%, normalised with respect to a representative A_{90} of 250 ms, while their standard deviations exhibit modest discrepancies. These differences may arise from the fact that ΔA_{d+v} and ΔA_{v} are measured in distinct cell populations, or from intrinsic cell-to-cell variability in drug responsiveness, analogous to variability observed under baseline conditions. Figure 5.14 shows the scatterplot of these same data showing individual cell predictions versus the same individual cell's experimental response. The coefficient of determination is $R^2 = 0.588$, indicating a moderate level of agreement and suggesting that the inferred conductance parameters capture a substantial component of the inter-cell variability in post-drug A_{90} values. To further

assess the predictive capability of the inferred parameters, Figure 5.15 compares the A_{90} prolongation induced by dofetilide relative to each cell's baseline A_{90}. In contrast to Figure 5.14, which considers post-drug A_{90} values, the agreement between simulated and experimental A_{90} prolongation is poor ($R^2 = -0.725$). This discrepancy arises because the model predicts positive A_{90} prolongation for all cells following a 15% reduction in $\hat{\alpha}_{\text{Kr}}$, whereas the experimental data exhibit substantial variability, including several cells that show little change or even a reduction in A_{90} following drug exposure.

Taken together, these results suggest that the inferred parameters capture a significant component of the variability in post-drug A_{90} values but do not fully explain the cell-to-cell variability in the A_{90} prolongation of the drug response. Additional sources of variability, including experimental noise, uncertainty in the degree of I_{Kr} block produced by 3 nM dofetilide, inter-cell differences in drug sensitivity, and electrophysiological mechanisms not represented in the current model formulation, may contribute to the observed differences. Nevertheless, the agreement observed in Figure 5.14 supports the predictive value of the inferred parameters, while the results of Figure 5.15 highlight important limitations that warrant further investigation. Finally, although the assumed degree of block and specificity of dofetilide action are informed by prior work [55], these properties remain incompletely characterised and require further investigation. Refinement of these assumptions is expected to improve quantitative agreement between model predictions and experimental observations, but such analyses lie beyond the scope of the present study.

5.4 Conclusion

Recent advances in voltage-sensitive fluorescence imaging have enabled high-throughput measurements of APs from large numbers of uncoupled cardiac myocytes [37], revealing substantial electrophysiological variability even among healthy cells. While experimental evidence for such heterogeneity is now well established in [6], mathematical models of cardiac electrophysiology have largely remained focused on generic cell representations and therefore fail to capture inter-cell variability. This mismatch

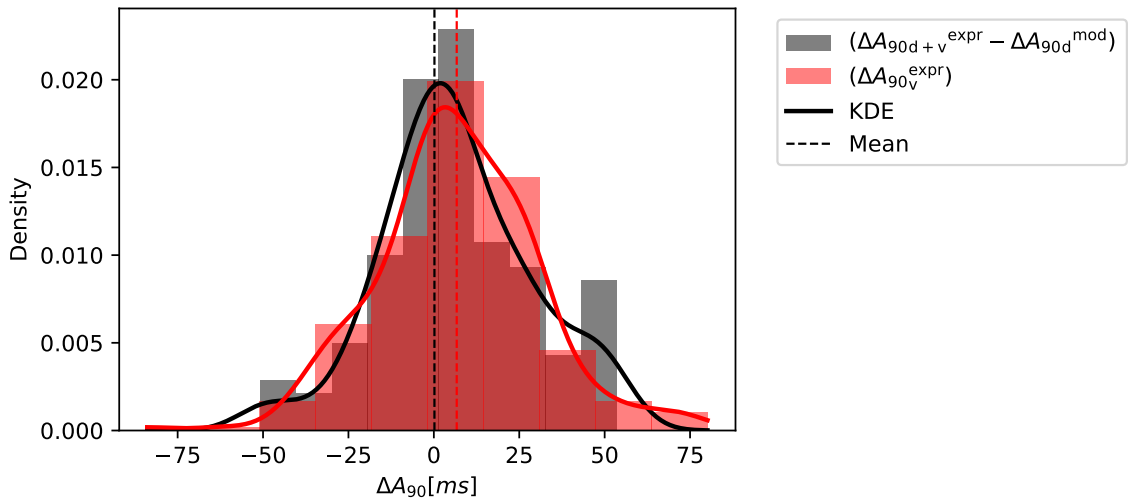

Figure 5.13: Comparison of the probability density functions of $f\left(\Delta A_{d+v}^{\text{expr}} - \Delta A_{d}^{\text{mod}}\right)$ (shown in black) and $f\left(\Delta A_{v}^{\text{expr}}\right)$ (shown in red) for the A_{90} biomarker following exposure to 3 nM dofetilide dissolved in 0.05% DMSO. Kernel density estimates (KDEs) are displayed along with the corresponding sample means, indicated by vertical dashed lines. Notation follows that introduced in the main text.

limits the predictive value of existing models in applications such as digital twinning, safety pharmacology, and drug-induced arrhythmia risk assessment.

In this chapter, I addressed this gap by developing a population of cell-specific mathematical models of rabbit ventricular myocytes that accurately reproduce experimentally measured AP waveforms. Starting from the detailed Shannon model, eight ionic conductance related parameters were selected based on prior sensitivity analysis in Chapter 4 and estimated individually for each cell using voltage-sensitive fluorescence recordings from 1228 myocytes. Parameter estimation was formulated within a maximum-likelihood framework assuming normally distributed measurement noise and was solved using a global, gradient-free optimization algorithm (CMA-ES). Model fits were assessed using formal measured standard errors of estimands and quantified goodness-of-fit criteria, resulting in a population of 1180 accepted cell-specific models.

The resulting ensemble was interpreted as a random sample from the phenotype of healthy rabbit ventricular myocytes. Statistical characterization of this population revealed broad parameter variability spanning multiple orders of magnitude and only weak inter-parameter correlations. Consequently, commonly used AP biomarkers, such as A_{90}, were shown to be more likely depend on combinations of parameters rather than on any single dominant conductance. Bayesian inference performed on representative cells confirmed near-uniqueness of the parameter estimates and demon-

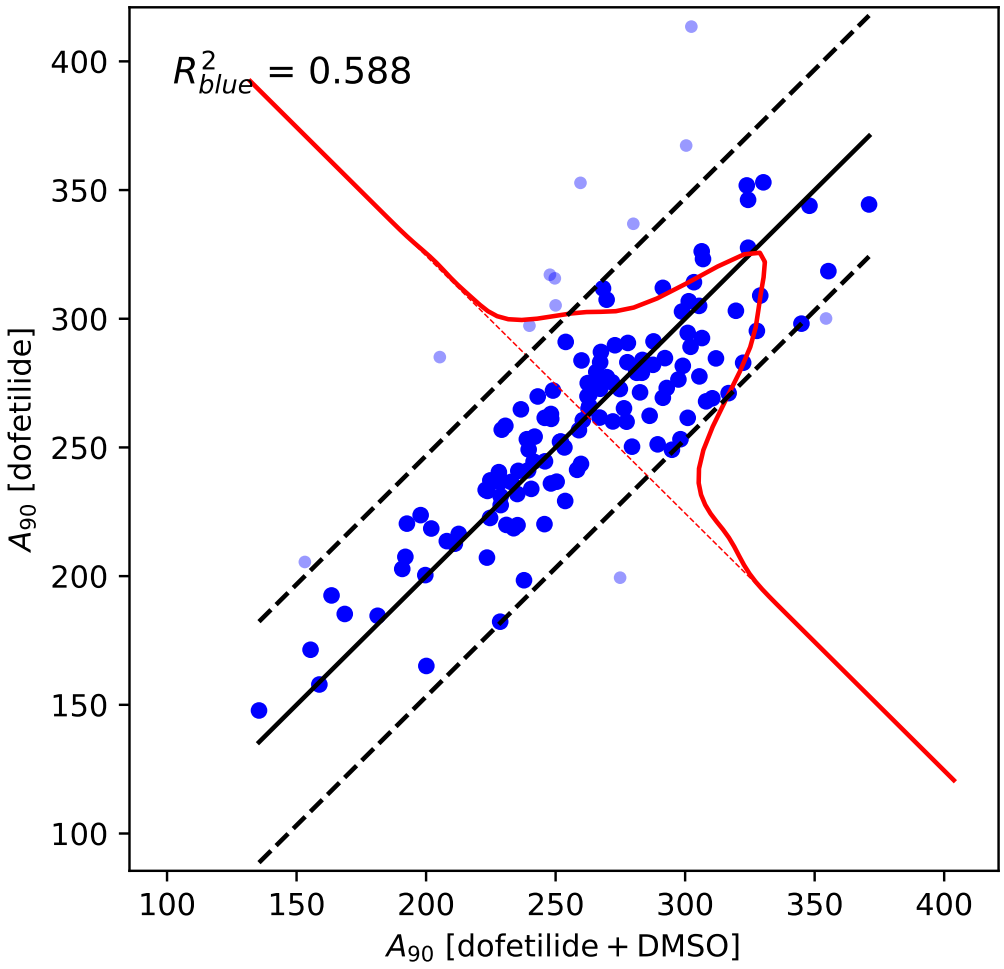

Figure 5.14: Scatter plot comparing model-predicted A_{90} values following simulated dofetilide application with experimentally measured A_{90} values obtained after exposure to 3 nM dofetilide dissolved in 0.05% DMSO. The identity line $y = x$ is shown as a solid black line. The kernel density estimate (KDE) of the DMSO-induced effect is displayed transversely to the $y = x$ line, illustrating the intrinsic random discrepancy between the abscissa and ordinate values. Black dashed lines denote ± 2 standard deviations from the mean of the DMSO KDE, corresponding to a 95% confidence interval. The coefficient of determination for the data points is $R^2 = 0.588$.

strated that classical standard errors were overestimated.

Beyond reproducing AP waveforms, the cell-specific models enabled forward prediction of unmeasured physiological quantities, including intracellular calcium dynamics and ionic current contributions. Predicted calcium biomarkers were consistent with experimental ranges reported in the literature, further supporting the physiological plausibility of the inferred models.

Crucially, the predictive value of the inferred parameters was validated using an independent pharmacological perturbation. Model predictions of AP duration changes in response to selective I_{Kr} block by dofetilide were shown to agree well with experimentally observed drug responses at the level of individual cells. This validation demonstrates that the inferred conductances capture meaningful physiological properties rather than merely enabling waveform fitting.

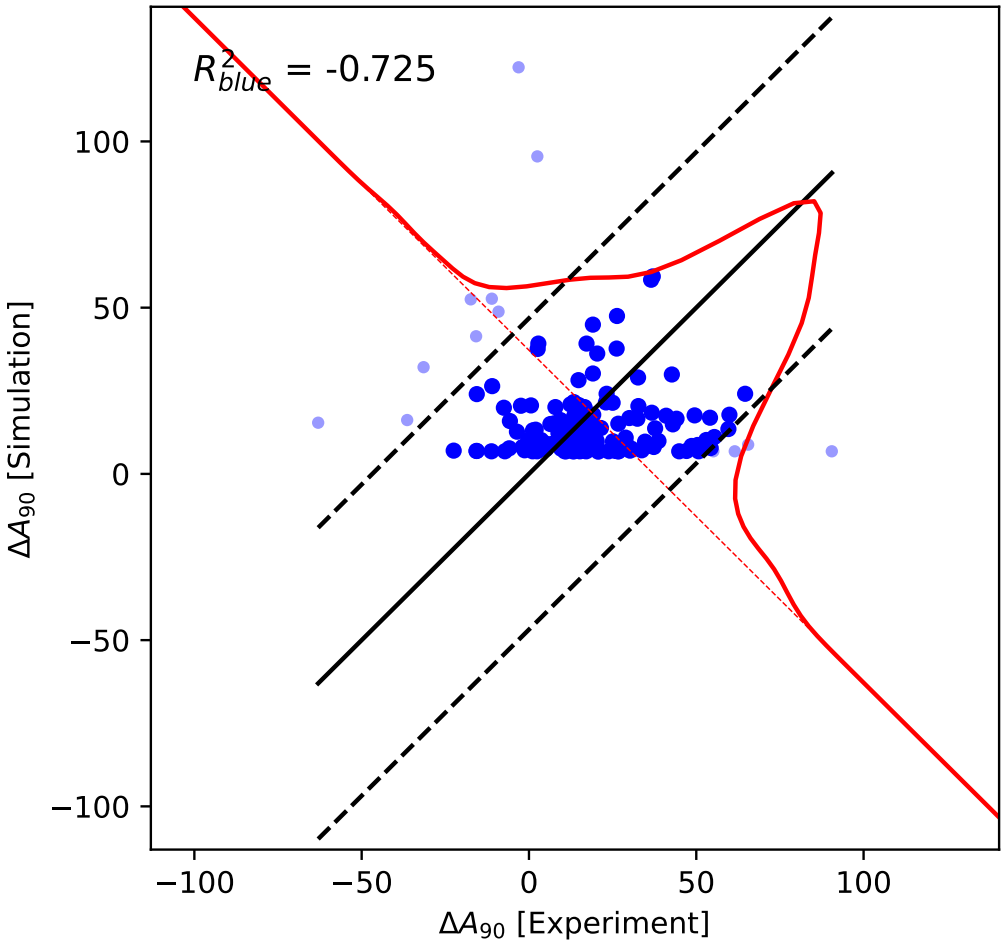

Figure 5.15: Scatter plot comparing model-predicted A_{90} prolongation (Δ A_{90}) following a simulated 15% reduction in $\hat{\alpha}_{\mathrm{Kr}}$ with experimentally measured A_{90} prolongation following exposure to 3 nM dofetilide. A_{90} prolongation was computed relative to each cell's baseline A_{90} value. The dashed line denotes the line of identity. The agreement in the magnitude of A_{90} prolongation is poor ($R^2 = -0.725$), reflecting substantial variability in the experimental drug response that is not captured by the current model formulation.

Overall, this chapter establishes a scalable and robust framework for constructing large populations of cell-specific cardiac electrophysiology models directly from experimental data. The resulting models bridge the gap between high-throughput electrophysiological measurements and mechanistic mathematical descriptions, providing a foundation for future studies of electrophysiological variability, drug response prediction, and personalized in silico cardiomyocyte modelling.

Chapter 6

Mechanistic Modelling of Anti-Arrhythmic Drug Action from Paired Cardiac Cell Recordings

The work presented in Chapter 5 demonstrated that detailed ionic models can be fitted efficiently to individual AP recordings at scale. A pilot version of the associated software [121] has been released, providing a prototype for an open and reproducible workflow for parameter estimation in these settings. In this chapter I will extend this approach to paired datasets, where recordings are available from the same cells before and after drug exposure. This will enable us to directly assess and predict drug-induced changes in ionic currents, creating a foundation for high-throughput tools in pre-clinical pharmacology.

6.1 Introduction

Cardiac AP morphology arises from the coordinated activity of multiple ionic currents, and its modulation by pharmacological agents provides critical insight into drug safety and efficacy. Dofetilide, a class III anti-arrhythmic, selectively inhibits

the rapid delayed rectifier potassium current (I_{Kr}), prolonging repolarization in a dose-dependent manner. Despite extensive study, quantitative estimates of the drug's effect on I_{Kr} remain variable across experiments, highlighting the challenge of capturing drug action in heterogeneous cellular populations.

During the pilot study in Chapter 5, it was demonstrated that detailed ionic models can be efficiently fitted to individual AP recordings at large scale. Building on this foundation, the present work extends the framework to paired datasets, where AP recordings are available from the same cells before and after drug exposure. This extension allows for direct inference of both baseline and the drug-induced modulation of ionic currents, reducing uncertainty associated with cell-to-cell variability and model simplifications. By using paired recordings, I can more reliably quantify pharmacodynamic effects and create predictive models of drug response that are grounded in individual cell physiology.

To achieve these goals, I employ a parameter estimation framework that simultaneously fits paired AP waveforms, enabling the direct inference of the cell-specific unblocked fraction of I_{Kr}. In addition, I explore predictive modelling under fixed pharmacodynamic assumptions, where the drug effect is prescribed based on literature or first-stage estimates. This allows assessment of whether parameters inferred at one concentration can generalize to other drug levels, offering a practical test of model transferability. By combining inference and prediction in a unified workflow, this study provides a robust, data-driven approach to quantify drug effects, capture population-level heterogeneity, and predict AP prolongation across a continuum of dofetilide concentrations. The resulting framework lays the groundwork for high-throughput, mechanistic tools in preclinical pharmacology, supporting early-stage drug evaluation and facilitating reproducible, scalable modelling of electrophysiological responses.

6.2 Method and Model

Note that the settings of fluorescence recordings of AP waveforms before and after drug are the same as Section 5.2.2, I will not repeat these in this section.

6.2.1 Modelling Drug-induced Inhibition of K^+ Channels

For the AP model of rabbit ventricular myocytes, I use the same Shannon model [3] as chapters 4 and 5. As typical for models of myocyte electrophysiology, the Shannon model can be expressed as a system of ordinary differential equations shown by equation (4.1). The numerical solution for the model has already been introduced in Section 4.2.1.

In this study, dofetilide is assumed to be a singular blocker of the rapid delayed rectifier potassium ionic current (I_{Kr}) suggested by the former study [53]. Rather than explicitly modelling drug action at the level of individual ionic current formulations, I represent the electrophysiological effects of dofetilide through modulation of estimated ionic current parameters. To be more specific, the voltage- and time-independent block by dofetilide is modelled by simply reducing the ionic current parameter by a drug action matrix $\boldsymbol{\beta}$. Let $\boldsymbol{\Theta}_{\mathrm{baseline}}$ denote the vector of estimated parameters before the drug under baseline conditions. The parameters under drug exposure, denoted by $\boldsymbol{\Theta}_{\mathrm{drug}}$, are obtained via a linear drug-action transformation:

$$\boldsymbol{\Theta}_{\mathrm{drug}} = \boldsymbol{\beta}\,\boldsymbol{\Theta}_{\mathrm{baseline}}, \tag{6.1}$$

where $\boldsymbol{\beta}$ is a diagonal drug-action matrix encoding the effect of the drug on specific ionic current parameter α_{Kr}. For illustration, consider a system with three ionic current parameters,

$$\boldsymbol{\Theta}_{\mathrm{baseline}} = \begin{bmatrix} \alpha_i \\ \alpha_{\mathrm{Kr}} \\ \alpha_j \end{bmatrix}, \quad \boldsymbol{\beta} = \begin{bmatrix} 1 & 0 & 0 \\ 0 & \varphi & 0 \\ 0 & 0 & 1 \end{bmatrix},$$

such that

$$\boldsymbol{\Theta}_{\mathrm{drug}} = \begin{bmatrix} \alpha_i \\ \varphi\alpha_{\mathrm{Kr}} \\ \alpha_j \end{bmatrix}.$$

Here the parameter φ represents the fraction of I_{Kr} that is not blocked by the drug of dofetilide, while all other parameters such as α_i, α_j remain unchanged.

6.2.2 Parameter Estimation for Drug Response to Dofetilide

In this approach, I directly incorporate drug response into the parameter estimation framework by extending the methodology introduced in Section 5.2.1. Rather than fitting a single AP trace per cell, I now perform simultaneous parameter estimation on two AP traces from the same biological cell: one recorded before dofetilide administration (baseline), and the other one recorded after drug exposure.

I use the same eight parameters as shown in 5.14 for model simulation. Assuming independent, normally distributed observational noise with standard deviation σ, the AP waveform before drug is modeled using:

$$\boldsymbol{\Theta}_{\text{baseline}} = \left[\alpha_{\text{NaCa}}, \alpha_{\text{NaK}}, \alpha_{\text{Clb}}, \alpha_{\text{CaL}}, \alpha_{\text{tos}}, \alpha_{\text{K1}}, \alpha_{\text{Ks}}, \alpha_{\text{Kr}}\right]^\top$$

and the AP waveform after drug is generated using:

$$\boldsymbol{\Theta}_{\text{drug}} = \boldsymbol{\beta}\,\boldsymbol{\Theta}_{\text{baseline}} = \left[\alpha_{\text{NaCa}}, \alpha_{\text{NaK}}, \alpha_{\text{Clb}}, \alpha_{\text{CaL}}, \alpha_{\text{tos}}, \alpha_{\text{K1}}, \alpha_{\text{Ks}}, \varphi\alpha_{\text{Kr}}\right]^\top$$

Here the drug action matrix for this case would be a diagonal matrix

$$\boldsymbol{\beta} = \text{diag}\,(1,\ 1,\ 1,\ 1,\ 1,\ 1,\ 1,\ \varphi) \tag{6.2}$$

The assumption of normality of errors is well satisfied and has already been testified by the autocorrelation and histogram of residual differences in Figure 5.3. This formulation enables us to perform multi-output optimization, fitting both AP waveforms simultaneously by maximizing the likelihood over the combined dataset.

I denote the two observed experimental AP waveforms from a given cell as

$$\mathcal{D}^{(1)} = \{(t_j, V_j^{(1)})\}_{j=1}^{K_1} \quad \text{and} \quad \mathcal{D}^{(2)} = \{(t_j, V_j^{(2)})\}_{j=1}^{K_2},$$

corresponding to the recordings before and after dofetilide administration, respectively. The model outputs are denoted by

$$\mathcal{M}^{(1)}(\mathbf{\Theta}_{\text{baseline}}) = \{V^{(1)}_{\text{mod}}(t_j; \mathbf{\Theta}_{\text{baseline}})\}_{j=1}^{K_1} \quad \text{and} \quad \mathcal{M}^{(2)}(\mathbf{\Theta}_{\text{drug}}) = \{V^{(2)}_{\text{mod}}(t_j; \mathbf{\Theta}_{\text{drug}})\}_{j=1}^{K_2},$$

Now consider

$$\mathbf{\Theta} = [\alpha_{\text{NaCa}}, \alpha_{\text{NaK}}, \alpha_{\text{Clb}}, \alpha_{\text{CaL}}, \alpha_{\text{tos}}, \alpha_{\text{K1}}, \alpha_{\text{Ks}}, \alpha_{\text{Kr}}, \sigma, \varphi]^\top$$

consists of all eight parameters, drug action parameter and the standard deviation parameter. The log-likelihood is a modified version of equation (5.4), which is given by:

$$\begin{aligned} \log L(\mathcal{D}^{(1)}, \mathcal{D}^{(2)}; \mathbf{\Theta}) = &-\frac{1}{2\sigma^2} \sum_{j=1}^{K_1} \left(V_j^{(1)} - V^{(1)}_{\text{mod}}(t_j; \mathbf{\Theta}_{\text{baseline}}) \right)^2 \\ &- \frac{1}{2\sigma^2} \sum_{j=1}^{K_2} \left(V_j^{(2)} - V^{(2)}_{\text{mod}}(t_j; \mathbf{\Theta}_{\text{drug}}) \right)^2 \\ &- (K_1 + K_2) \log(\sigma\sqrt{2\pi}). \end{aligned} \tag{6.3}$$

The optimal parameter vector $\hat{\mathbf{\Theta}}$ is then obtained by maximizing this likelihood:

$$\hat{\mathbf{\Theta}} = \arg\max_{\mathbf{\Theta} \in \Omega} \log L(\mathcal{D}^{(1)}, \mathcal{D}^{(2)}; \mathbf{\Theta}) \tag{6.4}$$

with

$$\hat{\mathbf{\Theta}} = [\hat{\alpha}_{\text{NaCa}}, \hat{\alpha}_{\text{NaK}}, \hat{\alpha}_{\text{Clb}}, \hat{\alpha}_{\text{CaL}}, \hat{\alpha}_{\text{tos}}, \hat{\alpha}_{\text{K1}}, \hat{\alpha}_{\text{Ks}}, \hat{\alpha}_{\text{Kr}}, \hat{\sigma}, \phi]^\top$$

where $\Omega \in R^{10}$ is an appropriately constrained region of the parameter space.

In order to measure the errors of parameter estimation ($\sigma_{\hat{\Theta}}$) and access the goodness of fit (p), I use the same equations (5.6) and (5.9) respectively, which have been tested to be useful on 1228 cells.

The global maximization (equation 6.4) of the logarithm of the likelihood function (equation 6.3) is performed using the Exponential Natural Evolution Strategy (xNES) algorithm [84], as implemented in the Python module PINTS [85]. The xNES algorithm is a stochastic, derivative-free optimization method designed for non-linear, high-dimensional, and non-convex problems. Instead of computing gradients of the

likelihood function, xNES maintains and iteratively updates a multivariate Gaussian search distribution, defined by its mean vector and covariance matrix. Candidate parameter sets are sampled from this Gaussian distribution, evaluated by simulating the Shannon model, and ranked according to their likelihood values (equation 6.3). The algorithm then updates the mean and covariance of the Gaussian using a natural gradient computed in the distribution space, which ensures invariance under linear transformations of the parameter space. The initial settings of xNES are identical to those used for CMA-ES in Section 5.2.4.

6.2.3 Predictive Modelling under Known Drug Effects

Following the estimation of drug effects directly from paired baseline and post-drug recordings above, I next considered a complementary predictive modelling framework in which the pharmacodynamic effect of dofetilide is assumed to be known. This formulation addresses a distinct but practically important question: whether inferred parameters at one drug concentration can generalize to other concentrations, and whether reliable predictions of drug response can be generated when experimental recordings are limited or unavailable.

6.2.3.1 Fixed Pharmacodynamic Formulation

For each dofetilide concentration, the unblocked fraction of the rapid delayed rectifier potassium current I_{Kr} was fixed to literature values reported by [42]:

$$\varphi_{\mathrm{Li}}(3\,\mathrm{nM}) = 0.61, \qquad \varphi_{\mathrm{Li}}(30\,\mathrm{nM}) = 0.16, \qquad \varphi_{\mathrm{Li}}(100\,\mathrm{nM}) = 0.06, \qquad \varphi_{\mathrm{Li}}(300\,\mathrm{nM}) = 0.02.$$

In this formulation, φ is no longer treated as an estimand. Instead, the Shannon model is modified by scaling the relative strength of I_{Kr} according to equation (6.1) with the correspondent drug action matrix

$$\boldsymbol{\beta} = \mathrm{diag}\,(1,\ 1,\ 1,\ 1,\ 1,\ 1,\ 1,\ \varphi_{\mathrm{Li}}(c)) \tag{6.5}$$

while all other parameters α and the observational noise parameter σ are constrained to be identical between baseline and post-drug conditions. This isolates the drug effect to a single, physiologically interpretable intervention on I_{Kr}.

6.2.3.2 Simultaneous Parameter Estimation at Fixed Concentration

Using the fixed pharmacodynamic formulation, simultaneous parameter estimation was performed independently for each of the four experimental drug concentrations. For a given training concentration c_{train}, paired AP recordings $(\mathcal{D}^{(1)}, \mathcal{D}^{(2)})$ from baseline and post-drug conditions were fitted simultaneously by maximizing the Gaussian log-likelihood defined in equation 6.3.

The free parameter estimands consisted of eight ionic current scaling factors and the observational noise parameter:

$$\hat{\boldsymbol{\Theta}} = \left[\hat{\alpha}_{\text{NaCa}},\, \hat{\alpha}_{\text{NaK}},\, \hat{\alpha}_{\text{Clb}},\, \hat{\alpha}_{\text{CaL}},\, \hat{\alpha}_{\text{tos}},\, \hat{\alpha}_{\text{K1}},\, \hat{\alpha}_{\text{Ks}},\, \hat{\alpha}_{\text{Kr}},\, \hat{\sigma}\right]^{\top}.$$

Optimisation was carried out using the same xNES algorithm implemented in PINTS, employing the same initialization strategies and parameter bounds as described in Section 6.2.2. This procedure yielded four distinct populations of fitted parameter sets, one corresponding to each drug concentration.

6.2.3.3 Cross-concentration Prediction Protocol

To assess predictive generalizability, I conducted a systematic cross-concentration prediction analysis. For a given training concentration c_{train}, each fitted parameter set $\hat{\boldsymbol{\Theta}}(c_{\text{train}})$ was used to generate post-drug predictions at a different target concentration c_{target}. This was achieved by rescaling only the I_{Kr} parameter according to the pharmacodynamic factor for the target concentration:

$$\hat{\alpha}_{\text{Kr}}(c_{\text{target}}) = \varphi_{\text{Li}}(c_{\text{target}})\hat{\alpha}_{\text{Kr}}(c_{\text{train}}) \tag{6.6}$$

All other parameters were held fixed. The model was then simulated to produce a predicted post-drug AP waveform at c_{target}.

This procedure was repeated for all ordered concentration pairs:

$$(3 \to 30, 100, 300), \qquad (30 \to 3, 100, 300), \qquad (100 \to 3, 30, 300), \qquad (300 \to 3, 30, 100).$$

6.2.3.4 Biomarker Extraction and Statistical Comparison

For each predicted waveform, the AP duration at 90% repolarization A_{90} was computed. Predicted values were aggregated across cells to form a distribution for each $(c_{\text{train}} \to c_{\text{target}})$ pair.

Predictive accuracy was quantified by comparing predicted and experimentally observed A_{90} distributions at the target concentration using three complementary statistical tests: the Mann–Whitney U test (difference in medians), Welch's two-sample t-test (difference in means), and the Kolmogorov–Smirnov (KS) test (difference between full distributions). These tests probe distinct aspects of distributional agreement and were therefore used jointly. A prediction was considered statistically consistent with experimental data when none of the tests rejected the null hypothesis at the 0.05 significance level.

6.3 Results and Discussion: Inferred Dofetilide Pharmacodynamics and Predictive Modelling Under Known Drug Effects

In this section, I present and interpret the results of mechanistic inference and predictive modelling of dofetilide action based on paired baseline and post-drug cardiac cell recordings. The analysis is structured to progressively address both inference and prediction: first, by quantifying the concentration-dependent pharmacodynamic effects of dofetilide on I_{Kr}, and subsequently, by evaluating the extent to which inferred parameters under certain concentration group can support robust prediction across drug concentrations and under uncertainty.

6.3.1 Dofetilide Pharmacodynamics: Inferring Effects at Different Concentrations

The accepted model fits for the nine pairs of cells before and after induced dofetilide of our illustrative subset are shown in Fig 6.1. A detailed interpretation of such model fits for single cell AP traces has been previously demonstrated in Section 5.3.1.4, "model fits" of our prior, and will not be repeated here.

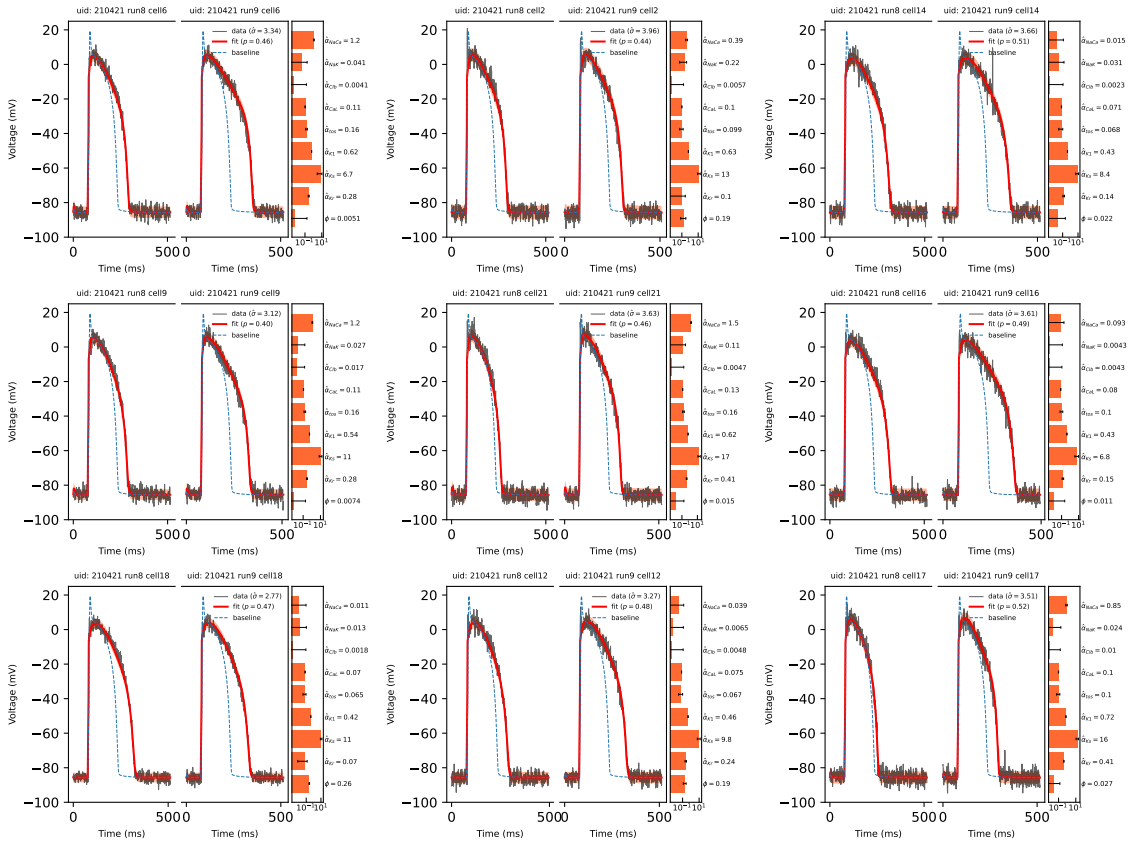

Figure 6.1: Examples of AP prediction for nine typical biological myocytes before and after drug. Cells are identified by unique identifiers (see the title for each plot). The experimentally-measured AP waveforms are shown by thin black lines. AP waveforms $V(t)$ computed from the accepted fits of the Shannon model are shown by thick orange-red lines. Estimates of the standard deviation of noise in voltage measurements are quoted in the legends and are illustrated by the width of the semi-transparent orange-red strips centred on $V(t)$. The corresponding point estimates of the parameter values and their standard errors are quoted and illustrated in a separate bar chart for each cell. The goodness-of-fit values p are listed in the legends. The AP waveform $V(t)$ of the baseline Shannon model is shown by blue dashed lines for comparison.

Table 6.1 summarizes the distribution of ϕ, the unblocked fraction of I_{Kr}, across 594 cells totally under four different concentration of dofetilide. The statistics are presented in non-logarithmic space, which allows a direct physiological interpretation in terms of block percentages. Fig 6.2 illustrates the dose response curve by comparing the statistical measures of the inferred unblocked fraction (ϕ) from our cell population with previously published literature values and provides a population-level

view of the inferred pharmacodynamic response to dofetilide across concentrations ranging from 3 to 300 nM. First, the central tendency of ϕ decreases monotonically with increasing drug concentration, in agreement with the expected dose dependent inhibition of I_{Kr}. This broad trend aligns well with literature values reported in [52], [55], [54], [41], and [42], providing external validation of our estimation framework. Notably, however, the mode and median of the inferred distribution consistently lie closer to the literature reported unblocked fractions in [54] and [42] than the mean, particularly at 100 and 300 nM. This observation reflects the strong positive skew in the distribution of ϕ at higher concentrations in Table 6.1 that most cells exhibit very strong block with small ϕ, while a minority retain substantially larger unblocked fractions, inflating the mean value. Although the median and mode provide robust indicators of the predominant high concentration drug effect within the population, the behaviour of the mean unblocked fraction offers an additional and biologically informative perspective. The mean value of ϕ follows a monotonic decline from 3 to 100 nM and remains broadly consistent with the literature values reported in [42] over this range. This agreement suggests that, at low and intermediate concentrations, the average level of block inferred from our population is compatible with single channel pharmacology measurements. However, at 300 nM the mean displays a striking deviation from this downward trend instead of approaching a small value together with the mode and median, it increases and lies closer to the value reported in [55]. This deviation is not reflected in the median or the mode, both of which remain tightly clustered near zero, indicating that almost all cells experience nearly complete I_{Kr} block. The elevated mean at 300 nM arises from the long right tail of the ϕ distribution, where a small subgroup of cells retains unexpectedly large unblocked fractions despite the high nominal drug concentration. This behaviour is physiologically interesting and meaningful. At very strong I_{Kr} inhibition, heterogeneity in repolarization reserve becomes amplified and cells with comparatively dominant secondary repolarizing currents such as I_{CaL} can sustain repolarization even when I_{Kr} is severely suppressed, producing APs that are well fitted with a larger apparent ϕ.

Second, the spread of the inferred ϕ values increases substantially at intermediate and high concentrations. This widening visible as a divergence between the statistics

statistic	3 nM	30 nM	100 nM	300 nM
Count	105	226	155	108
Mean	0.5747	0.1859	0.0399	0.1180
Std	0.3185	0.3022	0.1626	0.2320
Min	0.0034	0.0009	0.0004	0.0007
25%	0.3381	0.0085	0.0028	0.0036
Median	0.6031	0.0221	0.0050	0.0109
75%	0.8321	0.2270	0.0101	0.1061
Max	1.0000	0.9999	0.9943	0.9999
Skewness	-0.2119	1.6228	5.2839	2.5545
Kurtosis	-1.1723	1.1916	26.5989	5.8087

Table 6.1: Summary statistics for estimated drug action parameter ϕ at different drug-induced concentrations.

suggests that cell-to-cell heterogeneity becomes more pronounced as I_{Kr} availability is reduced. Biophysically, this is due to that once I_{Kr} is strongly inhibited, secondary repolarizing currents (I_{Ks}, I_{to}, I_{CaL}) vary more strongly in their relative contribution across cells, exposing intrinsic electrophysiological diversity that is masked at low level block. The right tail outliers observed at 300 nM meaning cells with unexpectedly large ϕ likely correspond to myocytes in which alternative repolarizing pathways can partially compensate for I_{Kr} block, or to cells whose AP biomakers are dominated by currents with weaker sensitivity to dofetilide. This interpretation is supported by our uncertainty analyses in Section 6.3.4, which show that multiple ionic current parameter configurations can generate similar APs. The discussion for 300 nM can be explored into a complementary insight from the log-transformed histogram (Figure 6.3). In log-space, the density peak also is revealing that most cells cluster tightly around very small ϕ values. Interestingly, the kernel density estimate (KDE) also suggests a secondary, less pronounced peak around $\log_{10}(\phi) \approx -0.85$ ($\phi \approx 0.141$), which is less obvious in linear space due to compression near zero. This value may illustrate the findings in [41], which point out the value of ϕ should be close to 0.159. This highlights the advantage of log-scaling for visualizing multiplicative heterogeneity, while retaining non-logarithmic summary values for physiological interpretation. To further investigate these observations, Figure 6.4 presents scatter plots of the inferred drug-response parameter ϕ against the experimentally measured control A_{90} (panel (a)), and against the inferred I_{Kr} scaling parameter, $\hat{\alpha}_{\mathrm{Kr}}$ (panel (b)).

Figure 6.4(a) examines the relationship between the inferred drug-response parameter ϕ and the experimentally measured control A_{90}. If large inferred values of ϕ were primarily a consequence of intrinsically reduced baseline I_{Kr}, then cells with large ϕ might be expected to exhibit systematically prolonged control APs. However, no clear relationship is observed. Relatively large values of ϕ occur across a broad range of control A_{90} values and are not concentrated among cells with the longest baseline action potentials. Conversely, cells with prolonged control A_{90} are frequently associated with $\phi \approx 0$. The dominant population of cells exhibiting near-complete block is observed throughout the full range of control A_{90} values. These observations suggest that the right tail of the inferred ϕ distribution cannot be explained solely by differences in baseline AP duration.

Figure 6.4(b) examines the relationship between ϕ and the inferred parameter $\hat{\alpha}_{\mathrm{Kr}}$. If elevated values of ϕ were primarily produced through compensatory interactions within the inference procedure, a systematic dependence between these parameters might be expected. However, no clear trend is observed across the population. Cells with similar values of $\hat{\alpha}_{\mathrm{Kr}}$ exhibit a broad range of inferred ϕ, while the majority of cells remain clustered near $\phi \approx 0$ throughout the full range of inferred conductances. Furthermore, the relatively large-ϕ values are distributed across a wide range of $\hat{\alpha}_{\mathrm{Kr}}$ values rather than being concentrated at either low or high conductance levels. These observations provide little evidence for a dominant compensatory relationship between ϕ and $\hat{\alpha}_{\mathrm{Kr}}$.

Third, the dose response profile inferred from our population indicates stronger block at intermediate concentrations than several literature datasets, particularly around 30 nM. Whereas [41] reported relatively weak block at 30 nM ($\phi \approx 0.75$), these mode and median values suggest substantially greater I_{Kr} suppression. Conversely, at 3 nM these estimates are broadly consistent with these literatures. These discrepancies underscore the sensitivity of dofetilide pharmacodynamics to experimental conditions, cellular species, and measurement methodologies. The simultaneous estimation framework used here leverages paired AP traces from the same biological cell, which may capture subtle compensatory electrophysiological changes not observable in isolated channel experiments.

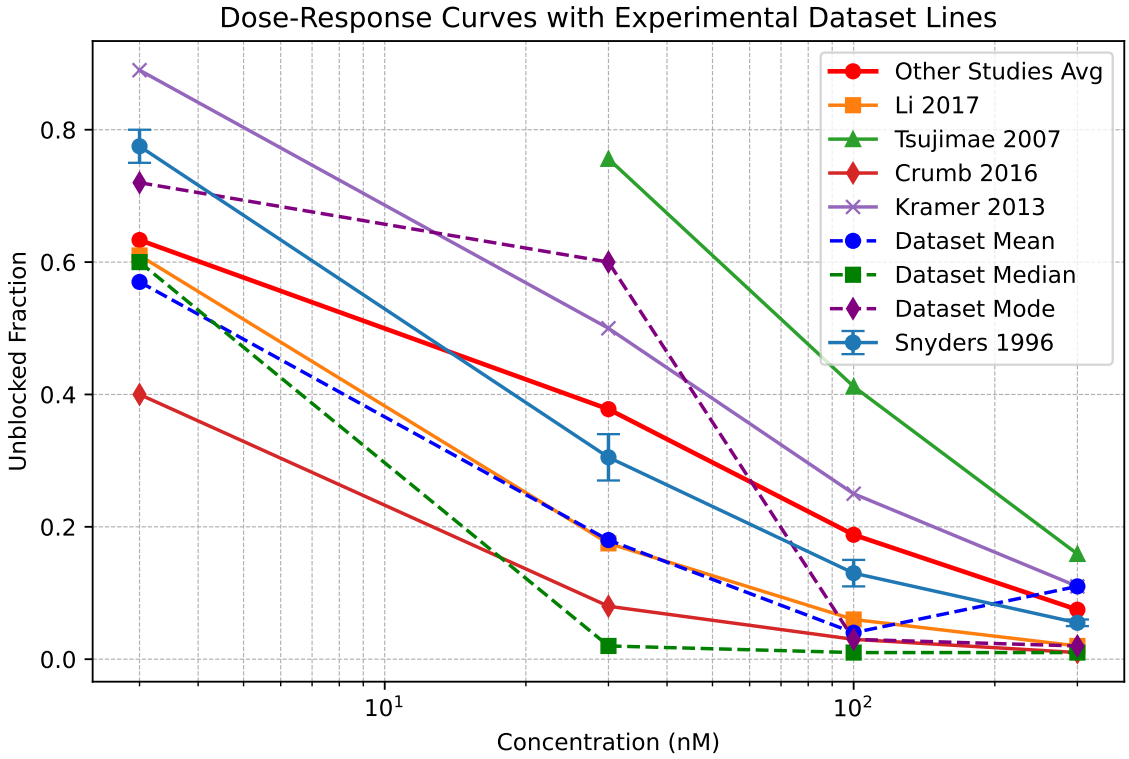

Figure 6.2: Population dose-response curve for the I_{Kr} unblocked fraction (ϕ). Inferred ϕ values from our cell population are compared with literature data from [52], [55], [54], [41], and [42]. The literature average curve in red is calculated as the mean of the ϕ values reported in these five studies. Dofetilide concentrations are shown on a logarithmic scale. Mode, median, and mean of the inferred ϕ distribution across cells at 3, 30, 100, and 300 nM are displayed as main statistics. Solid and dashed lines indicate individual literature values and the main statistic curve, respectively. Differences between mode, median, and mean illustrate cell-to-cell variability in drug response, contrasted against single-point literature estimates.

Taken together, Figure 6.2 demonstrates that the proposed inference approach not only reproduces documented pharmacodynamics of dofetilide, especially for [42], but also reveals previously uncharacterized population-level heterogeneity in I_{Kr} block. The divergence of statistics (mean, median, and mode) underscores the importance of using full distributional information rather than single point statistic to characterize drug effects in heterogeneous cell populations.

6.3.2 Model Prediction for Cumulative Ionic Currents

To illustrate the predictive capability of this framework, instead of computing the actual ionic currents which has been discussed in Section 5.3.1.5, I analyse the cumulative positive and negative ionic currents for the nine representative myocytes shown

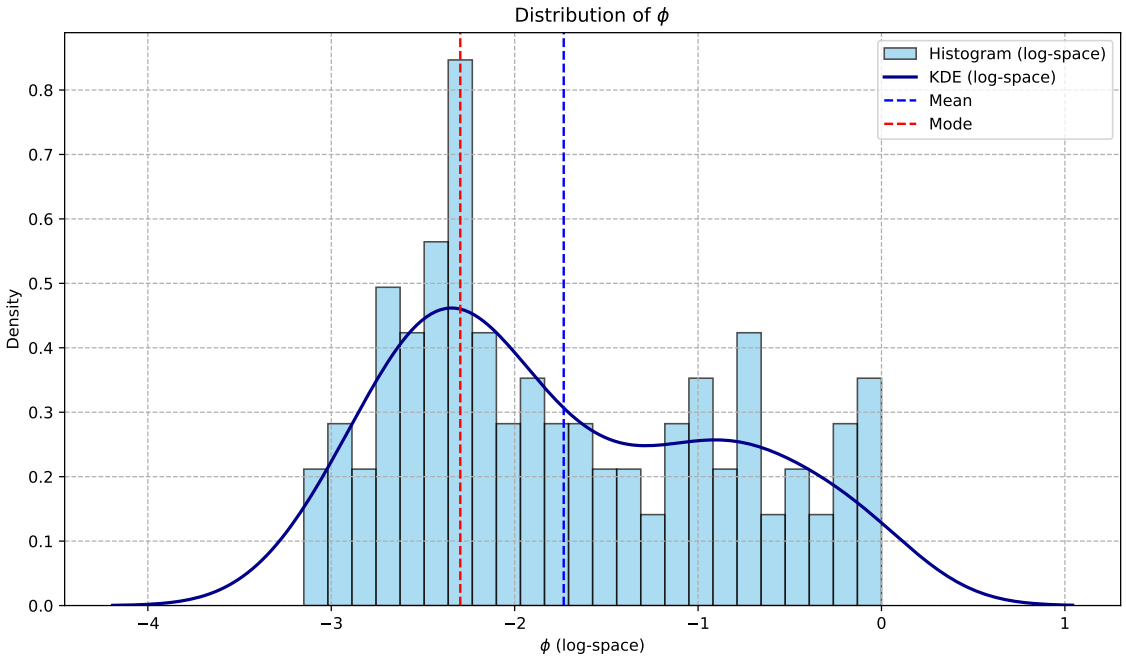

Figure 6.3: Histograms showing ϕ distributions in the log-transformation space for the 300 nM drug exposure condition. Red and blue dashed lines show the mode and the mean of ϕ, respectively. Kernel density estimation are shown in dark blue. Logarithmic scales are used and log means log10 here.

in Figure 6.1. The normalized cumulative currents $J_c^{\pm}(t)$ are defined as

$$J_c^{\pm}(t) = \pm \sum_{k=1}^{c} I_k^{\pm}(t) / \sum_{k=1}^{15} I_k^{\pm}(t), \quad c \in \{1, 2, ..., 8\} \tag{6.7}$$

$$I_k^{+}(t) = \max\left(I_k(t), 0\right), \qquad I_k^{-}(t) = \min\left(I_k(t), 0\right), \tag{6.8}$$

where $I_k(t)$ denotes the k-th ionic current of the Shannon model. The currents are ordered according to the set

$$[\text{Kr}, \text{Ks}, \text{K1}, \text{tos}, \text{CaL}, \text{Clb}, \text{NaK}, \text{NaCa}, \text{Na}, \text{Nab}, \text{tof}, \text{ClCa}, \text{Cab}, \text{Cap}, \text{Kp}].$$

Separating currents into positive and negative components allows the individual depolarizing and repolarizing contributions to be examined independently. The cumulative formulation preserves a strict ordering of magnitudes such that $|J_c^{\pm}(t)| < |J_{c+1}^{\pm}(t)|$, enabling currents to be visualized as layered contributions. When plotted in reverse order from largest to smallest magnitude, the complementary regions between $J_c^{\pm}(t)$ and $J_{c+1}^{\pm}(t)$ represent the incremental contribution of the $(c+1)$-th current.

The cumulative currents computed from the inferred cell-specific parameter sets are shown in Figure 6.5. Each coloured band represents the incremental contribution

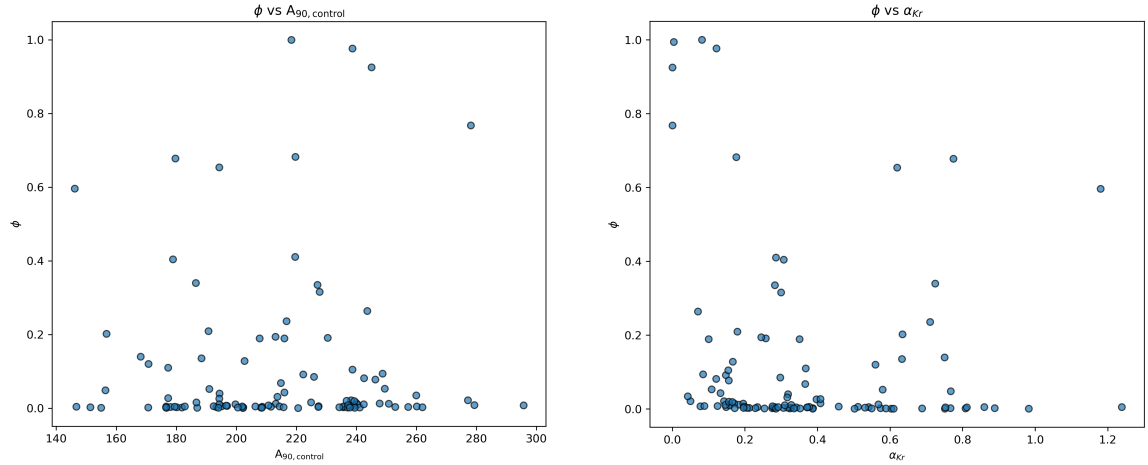

(a) ϕ versus experimentally measured control A_{90}.

(b) ϕ versus inferred $\hat{\alpha}_{\mathrm{Kr}}$.

Figure 6.4: Relationships between the inferred drug-response parameter ϕ and quantities potentially associated with its estimation in the 300 nM drug exposure. Panel (a) examines whether inferred ϕ values are associated with experimentally measured control A_{90}. Panel (b) examines whether inferred ϕ depends on $\hat{\alpha}_{\mathrm{Kr}}$, which could indicate compensatory interactions between model parameters during fitting.

of an individual ionic current, ordered according to its magnitude. The grey region denotes the combined contribution of currents that were not directly included in the parameter inference procedure.

Across all cells, the dominant outward repolarizing contribution is provided by potassium currents. Following dofetilide exposure, the contribution of I_{Kr} is visibly reduced, consistent with the known pharmacological action of the drug. However, the reduction in I_{Kr} is accompanied by variable compensatory increases in I_{Ks} and I_{K1} across cells. The magnitude of this compensation differs substantially between cells, highlighting heterogeneity in repolarization reserve.

In several post-drug models, inward currents, particularly I_{CaL}, contribute more prominently during the plateau phase. Cells exhibiting stronger inward plateau currents generally display longer AP durations, suggesting a reduced balance between inward and outward currents during repolarization. The residual cumulative current, shown in grey, represents the combined contribution of currents whose relative parameters were not included in the parameter inference procedure. Although these currents are not explicitly fitted, their contribution remains noticeable during the repolarization phase, indicating that repolarization is distributed across a broader set of ionic mechanisms.

Nevertheless, the fitted ionic current parameters account for the dominant variations in AP morphology across cells, while the remainder currents provide a back-

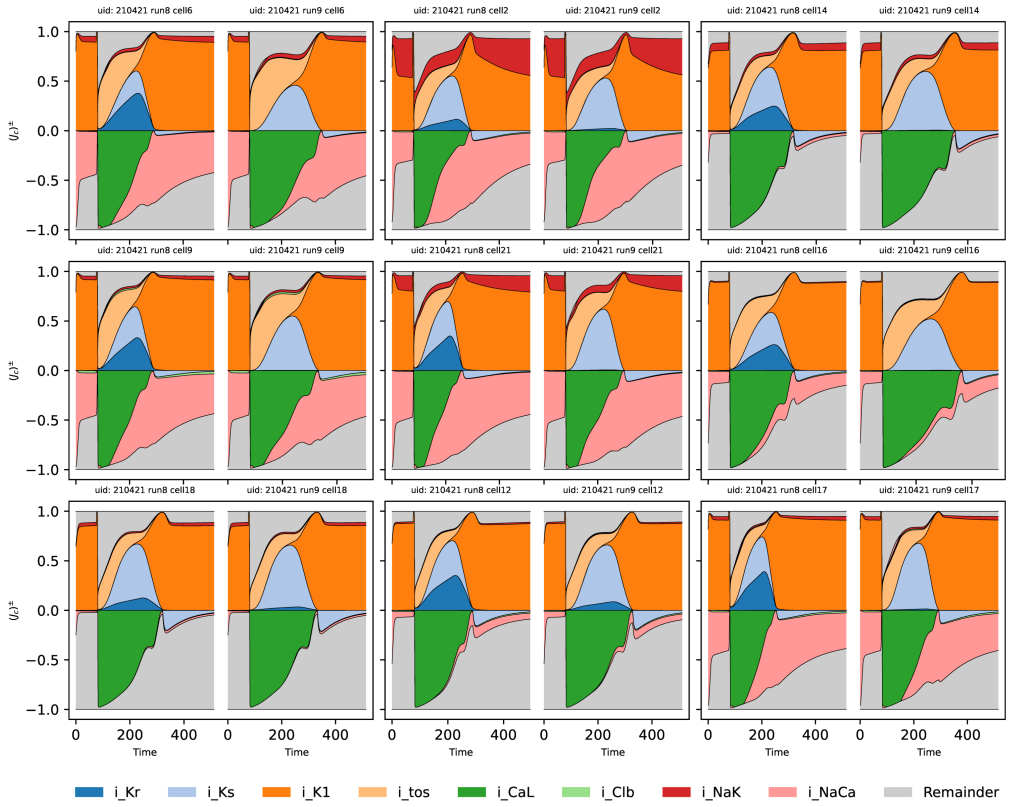

Figure 6.5: Normalized positive and negative cumulative currents $J_c^{\pm}$ as functions of time computed from the cell-specific models of the nine myocytes shown in figure 6.1. The cumulative currents are defined by equations (6.7, 6.8) in and coloured as specified in the figure legend.

ground repolarizing contribution that is relatively consistent across models.

6.3.3 Negative-control Validation of Drug-specific Parameter Inference

As a negative-control experiment, an additional parameter ϕ_{CaL} was included in the inference framework to determine whether the optimisation would incorrectly attribute the effects of dofetilide to block of the L-type calcium current. Since dofetilide is a highly selective I_{Kr} blocker, the expected value of ϕ_{CaL} is close to unity, indicating little or no inferred block of I_{CaL}.

Figure 6.6 shows a representative example of the resulting model fit together with summary statistics of the inferred ϕ_{CaL} values across the cell population. The representative fit demonstrates that the optimisation is able to reproduce the observed drug-induced changes in AP morphology while leaving the inferred ϕ_{CaL} value close to its physiologically expected value. This suggests that the optimisation primarily

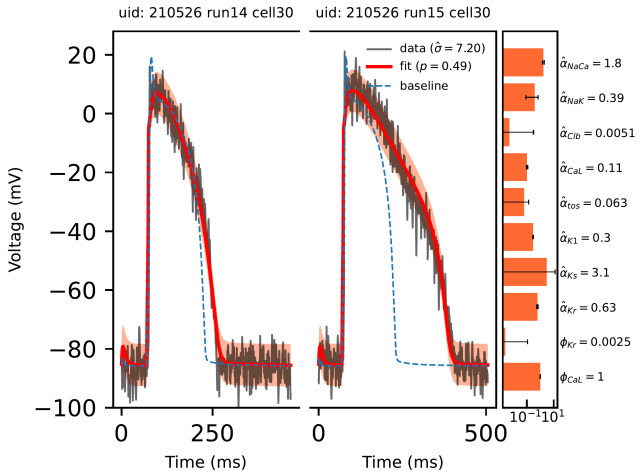

Summary statistics of inferred ϕ_{CaL}

(unblocked fraction of I_{CaL}; $n = 108$ cells)

Statistic	Value
Count (n)	108
Mean	0.965
Std Dev	0.057
Minimum	0.698
25% Percentile	0.950
Median (50%)	**0.989**
75% Percentile	0.999
Maximum	1.000
Skewness	−2.10
Kurtosis	5.80
Mode (hist-based)	0.99

Figure 6.6: Representative fit obtained when including an additional ϕ_{CaL} parameter for paired cells under 300 nM drug exposure together with summary statistics of the inferred ϕ_{CaL} values across the cell population. *Left:* Recorded AP traces (black) overlaid with model fit (red) and baseline (blue dashed); bar charts show inferred parameters. *Right:* Since dofetilide is a selective I_{Kr} blocker, ϕ_{CaL} is expected to remain close to 1. The median of 0.989 and mode of 0.99 confirm that the optimisation does not spuriously attribute dofetilide effects to I_{CaL} block, validating the negative-control criterion.

attributes the observed electrophysiological effects to changes in I_{Kr}, rather than compensating through artificial modification of unrelated ionic currents.

At the population level, the inferred ϕ_{CaL} values are strongly concentrated near unity. The median value is 0.989, the histogram-based mode is approximately 0.99, and the upper quartile is 0.999, indicating that the majority of cells exhibit little or no inferred I_{CaL} block. The mean value of 0.965 further supports this conclusion. Collectively, these statistics demonstrate that the optimisation naturally favours $\phi_{\mathrm{CaL}} \approx 1$ when fitting the dofetilide data.

These results suggest that the parameter estimation framework does not systematically compensate for dofetilide-induced APD prolongation by introducing spurious I_{CaL} block. Instead, the inferred values remain close to the physiologically expected value of $\phi_{\mathrm{CaL}} = 1$ for the vast majority of cells. The successful recovery of $\phi_{\mathrm{CaL}} \approx 1$ therefore provides evidence that the inference framework is capable of distinguishing the primary drug target from unrelated ionic currents. This negative-control experiment increases confidence in the physiological specificity and robustness of the proposed inference methodology.

6.3.4 Uncertainty on Estimates

Procedural uncertainty The Shannon model is a simplification of reality with some discrepancy from it, may also strongly influence the inferred parameters. In order to test simultaneous parameter estimation with dofetilide can give constrained parameter sets, I refit 21 pairs of cells with random initial guess within large range of boundary condition (from 0.0001 to 100) while mapping the values of V_{rest} and V_{plateau} to random values sampled from normal distributions with standard deviations of 1 mV from the means of -86 and 0 mV, respectively. Finally, I calculated the absolute value of relative difference $\frac{\mathbf{par_{fit1}} - \mathbf{par_{fit2}}}{\mathbf{par_{fit1}}}$ for each parameter. Basic summary statistics including ranges, mean, standard deviations and mode are listed in Table 6.2.

Count	Mean	Std	Min	25%	50% (Median)	75%	Max	Skewness	Kurtosis	Mode (hist-based)
186	0.315932	1.793418	0.000037	0.004214	0.02265	0.130944	22.335317	10.70203	122.902174	0.027956

Table 6.2: Descriptive statistics of the absolute relative differences between parameter estimates obtained from repeated fits with dofetilide under randomized initial conditions and perturbed V_{rest} and V_{plateau}. Statistics are computed across all parameters and cell pairs, summarizing the distribution of procedural uncertainty in the inferred parameters.

Figure 6.7 illustrates the procedural uncertainty analysis for two representative paired cells. Each row corresponds to a single biological cell pair (baseline and post-dofetilide), while the left and right panels show the results of two independent optimization runs initialized from randomized parameter values and perturbed V_{rest} and V_{plateau}. Despite the notable differences in initialization, the inferred AP waveforms are visually indistinguishable between repeated fits and closely match the experimental recordings in both baseline and post-drug conditions. Importantly, the estimated parameters and the drug action parameter ϕ are also highly consistent across runs. In these examples, parameters governing repolarization and drug response, including $\hat{\alpha}_{\text{Ks}}$, $\hat{\alpha}_{\text{Kr}}$, and ϕ, differ by less than approximately 6% between independent optimizations. Larger relative differences are observed only for a small subset of parameters such as $\hat{\alpha}_{\text{tos}}$, which have limited influence on the overall AP morphology. The uncertainty illustrated by the representative examples in Figure 6.7 is reflected more generally in the summary statistics reported in Table 6.2, which characterize the distribution of relative discrepancies across 21 repeated fits and parameters. Consistent with previous findings in Section 5.3.4.2, the majority of relative discrepancies were

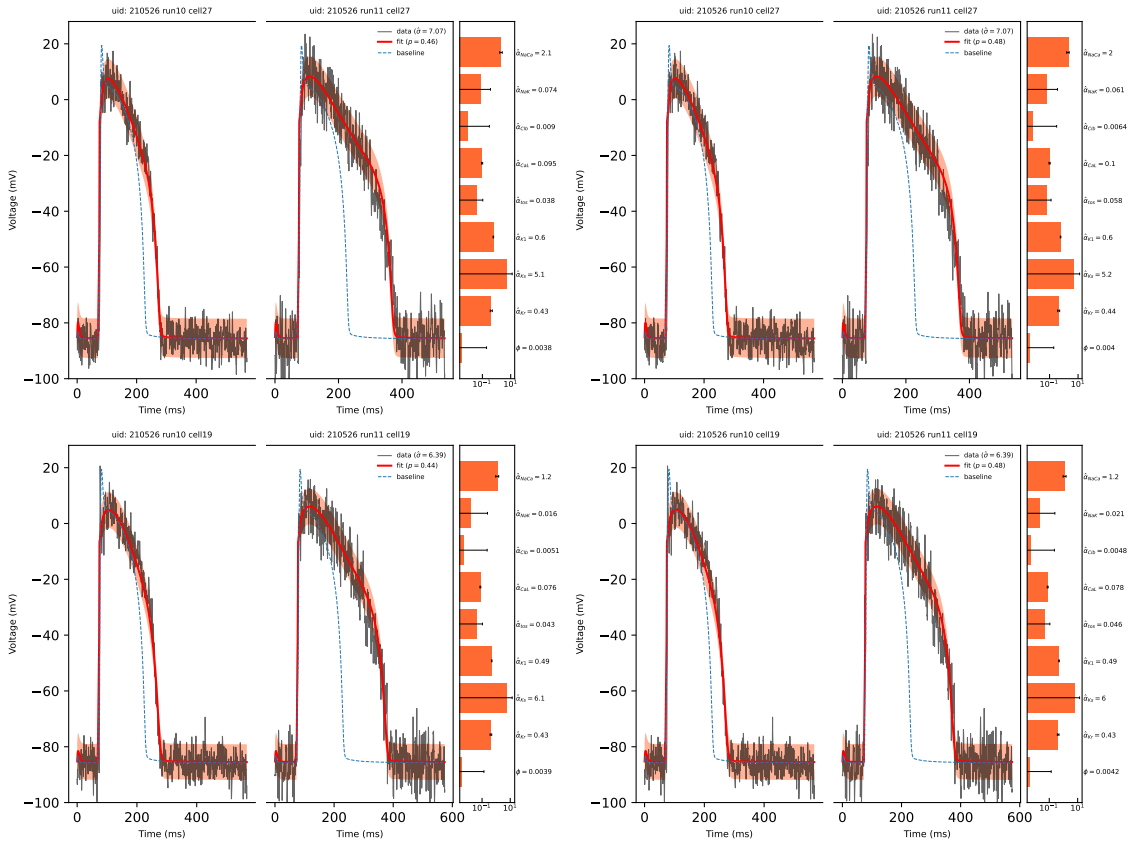

Figure 6.7: Uncertainty of simultaneous parameter estimation to randomized initial conditions under 100 nM dofetilide exposure. Each row corresponds to a single paired cell (baseline and post-dofetilide). Left and right panels show results from two independent optimization runs initialized from randomized parameter values and perturbed V_{rest} and V_{plateau}. Fitted AP waveforms and inferred parameters, including the drug action parameter ϕ, are nearly identical across runs, demonstrating low procedural uncertainty and strong convergence of the simultaneous fitting framework.

very small, with a median difference below 3%. The histogram-based mode is even smaller (≈ 0.028), indicating that the most frequently occurring differences across repeated fits are effectively negligible. A small number of very large discrepancies account for the long right tail of the distribution and these correspond to multiple parameter combinations generating nearly indistinguishable APs.

The close agreement between the median and mode demonstrates that the simultaneous fitting procedure with dofetilide retains the strong parameter constraining ability previously observed in the control-only study. In addition, the presence of paired data (before/after drug) provides extra structure that further restricts the feasible parameter space. Overall, these observations suggest that, for a given paired dataset, the simultaneous fitting procedure produces consistent and meaningful parameter estimates with minimal procedural uncertainty, providing useful parameter sets for further analysis.

Initial conditions uncertainty Another limitation of our study is that parameter es-

timation is performed on AP waveforms without prepacing of the model. Prepacing is the standard procedure with a periodic train of short stimulus pulses until the solution converges to a stable limit cycle.

In Section 5.3.4.1 this uncertainty was mitigated by showing that non-prepaced estimates can be converted to physiologically meaningful "prepaced" values by multiplying a common cell-specific factor derived from the ratios of late-time ionic fluxes. This operation effectively normalises away initial condition dependence.

In the present drug-modelling framework I retain this strategy, but an additional benefit arises from the introduction of the new drug response parameter ϕ, which represents the ratio of I_{Kr} after drug administration to that before administration. Because ϕ is defined as a ratio of two ionic current estimates obtained from the same cell, its sensitivity to initial condition uncertainty is greatly reduced. Specifically, if initial conditions induce a multiplicative shift in all parameters (for example, if both pre drug and post drug $\hat{\alpha}_{\text{Kr}}$ are scaled by the same factor), then

$$\phi = \frac{\hat{\alpha}_{\text{Kr}}^{\text{drug}}}{\hat{\alpha}_{\text{Kr}}^{\text{baseline}}}$$

remains invariant.

As shown in Table 6.3, for most cells the differences between ϕ and ϕ^{prep} are small, with average absolute difference $\Delta \approx 0.0037$ and average relative difference $\delta \approx 11\%$. This demonstrates that, for the majority of cells, the global scaling effects caused by uncertain initial conditions have minimal impact on the inferred drug-response parameter. A few cells, such as 210526_run13cell22, exhibit larger relative differences ($\delta > 150\%$), likely due to their very small baseline values, which make the ratio more sensitive to minor shifts. Despite these outliers, the overall pattern confirms that ϕ remains a meaningful and robust measure of I_{Kr} block, providing useful parameter sets for further dose-response analysis.

Thus, global scaling effect caused by uncertain initial conditions is very likely to cancel out in the computation of ϕ, making the inferred block parameter substantially more robust than the individual ionic current estimates. This cancellation property is particularly valuable because ϕ is the key pharmacodynamic quantity of interest.

Even if initial condition uncertainty introduces minor inaccuracies in absolute ionic current parameters, their ratio is preserved. Consequently, the inferred dose response relationships in Section 6.3.1 remain reliable even under substantial initial condition variability.

CellID with dofetilide	ϕ	ϕ^{prep}	$\Delta = \|\phi^{\text{prep}} - \phi\|$	$\delta = \left\|\frac{\phi^{\text{prep}}-\phi}{\phi}\right\|$
210511_run15cell9	0.013074911	0.014349802	0.001274891	0.097506715
210526_run13cell2	0.004425564	0.002641206	0.001784358	0.403192894
210526_run13cell17	0.004012951	0.004157526	0.000144575	0.036026884
210526_run13cell22	0.005930785	0.015102785	0.009172000	1.546507068
210526_run13cell13	0.001429645	0.002272737	0.000843092	0.589721232
210526_run13cell6	0.003302542	0.003573435	0.000270893	0.082025693
220824_run5cell10	0.048612120	0.041190281	0.007421839	0.152675410
220824_run5cell5	0.018694238	0.007882430	0.010811808	0.578349699
220824_run5cell7	0.006112224	0.004915006	0.001197218	0.195872856
Average			0.003658185	0.113521737

Table 6.3: ϕ values for eight pairs of cells with and without prepacing, and their differences.

6.3.5 Cross-Concentration Predictive Behaviour

Figure 6.8 summarizes the cross concentration predictive analysis. For each reference concentration (3, 30, 100, and 300 nM), the experimentally measured A_{90} distribution is compared with the distribution predicted using parameter sets inferred at that reference concentration and evaluated at all four target concentrations. Each panel displays kernel density estimates of experimental (solid red line) and predicted (dashed blue line) distributions, alongside the corresponding p-values from the Welch t-test (difference in means), Mann–Whitney U test (difference in medians), and Kolmogorov–Smirnov (KS) test (full-distribution comparison). This 4×3 grid forms a validation structure, enabling direct assessment of how well parameters inferred at one drug strength generalize to other degrees of I_{Kr} inhibition.

The cross concentration validation experiment demonstrates that the ability of ionic current parameters to generalize across drug concentrations depends strongly on the degree of I_{Kr} block at which the parameters were inferred. Models calibrated at 30 nM exhibited the most robust predictive performance, consistently reproducing the experimental A_{90} distributions at higher concentrations (e.g. 30 nM $\rightarrow$ 100

nM and 30 nM → 300 nM), with all three statistical tests yielding high p-values. This indicates that the ionic current parameters identified at 30 nM captures the repolarization dynamics that dominate under stronger I_{Kr} block. In contrast, models calibrated at higher concentrations (100 and 300 nM) showed good predictive accuracy only when extrapolated to concentrations at or above 30 nM, but consistently failed to reproduce the behaviour at 3 nM. This asymmetry reflects the strongly nonlinear dependence of repolarization on I_{Kr} availability: once I_{Kr} is heavily inhibited, the fitted parameters are shaped by a regime dominated by secondary repolarizing currents, and thus cannot reliably reconstruct the behaviour of cells operating under minimal block [122]. Conversely, 30 nM provides a perturbation that is large enough to reveal the major repolarization pathways, yet not so extreme as to collapse repolarization reserve, yielding parameter sets with the widest transferable range across drug concentrations.

In contrast, parameter sets inferred at the lowest concentration (3 nM) showed poor predictive accuracy when extrapolated to higher drug levels. At 3 nM, I_{Kr} block is minimal and the resulting APs closely resemble baseline behaviour. Under such weak perturbation, the parameter inference becomes poorly constrained that several combinations of I_{Kr}, I_{Ks} and I_{CaL} can reproduce the small changes in repolarization [1]. Consequently, the inferred parameters fail to capture the repolarization dynamics that dominate under strong I_{Kr} block, leading to systematic underestimation of A_{90} at 100 and 300 nM. This explains why all three tests robustly reject the predictions (typically $p < 10^{-3}$).

Taken together, these findings reveal an asymmetric structure in the predictive landscape: extrapolation between high concentrations is reliable, especially in the mid range (30-100 nM), while extrapolation across large differences in block strength (e.g. 3 nM → 300 nM) fails due to the strongly nonlinear response of repolarization to I_{Kr} suppression. This behaviour is consistent with the concept of nonlinear repolarization reserve, where the contributions of individual currents to repolarization vary dramatically as I_{Kr} is progressively inhibited. The results also support the practical conclusion that, in situations where experimental data are scarce, parameter sets inferred at intermediate drug concentrations provide the most transferable and

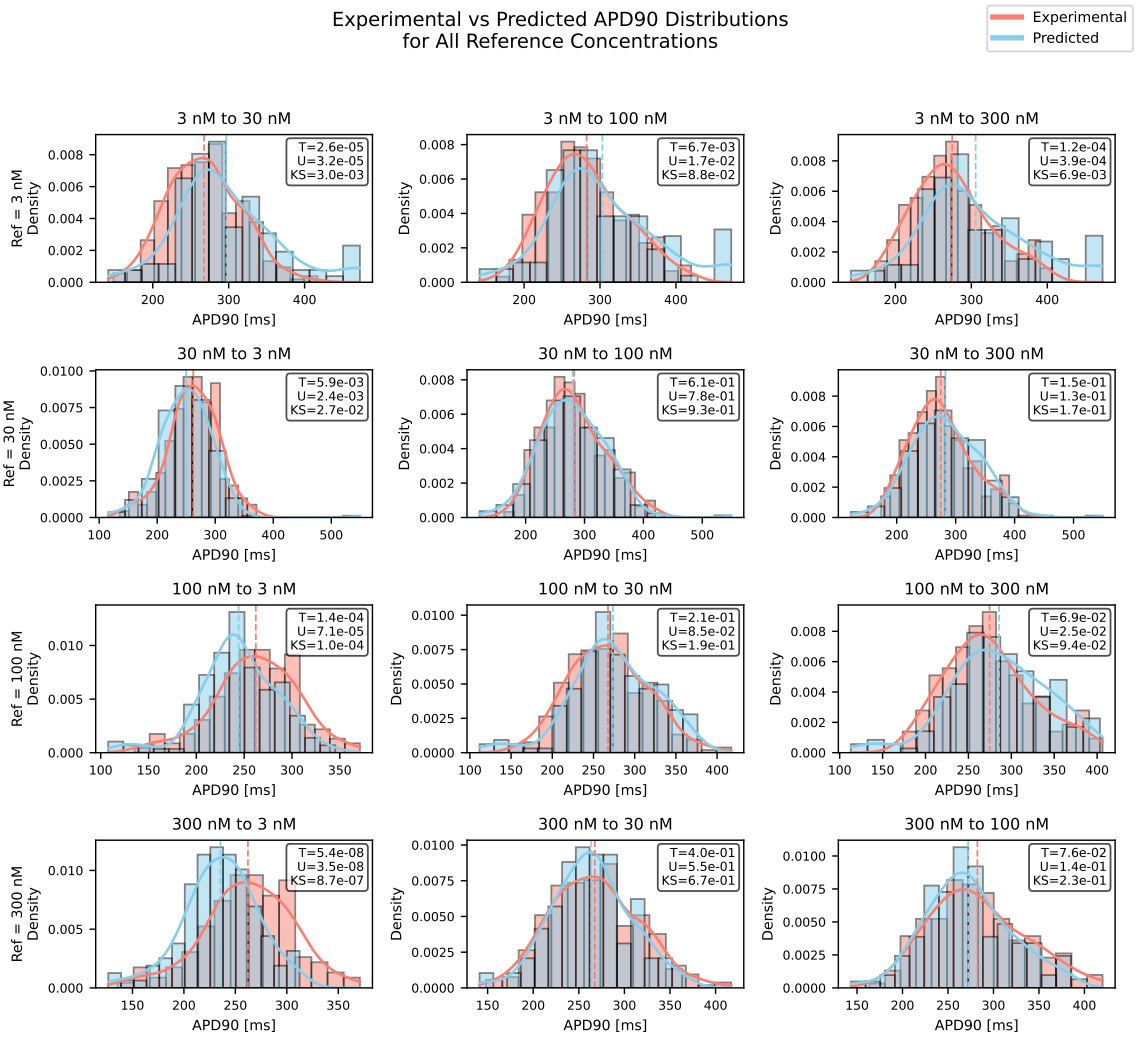

Figure 6.8: Cross concentration predictive performance for A_{90}. Experimental (solid red) and predicted (dashed blue) A_{90} distributions for all combinations of target concentrations. Each row corresponds to a reference concentration used for parameter estimation (3, 30, 100, and 300 nM), while each column shows predictions at a target concentration. p-values from the Welch t-test (T), Mann–Whitney U test (U), and Kolmogorov–Smirnov test (KS) are reported directly on each panel. High p-values ($p > 0.05$) indicate statistical agreement between the predicted and experimental distributions, while small p-values highlight systematic prediction failures.

physiologically informative representations of cellular electrophysiology.

6.3.6 Predictive A_{90} Dose Response Modelling Using the 30 nM Parameter Population

Having established that the 30 nM parameter population exhibited the strongest cross concentration predictive performance, I used this population as a generative model to predict AP prolongation across a continuum of dofetilide concentrations. For each concentration c, the pharmacodynamic effect on I_{Kr} was determined using the Hill

equation reported by [42], with Hill coefficient $n = 0.9$:

$$\varphi(c) = \frac{1}{1 + \left(\frac{c}{\mathrm{IC}_{50}}\right)^{n}},$$

The I_{Kr} parameter for each cell was then scaled as $\varphi(c)\,\hat{\alpha}_{Kr}$, while all other parameters remained fixed at their 30 nM values.

Using this formulation, the model was simulated over concentrations ranging from 1 to 1000 nM, generating a predicted A_{90} distribution at each concentration. For every concentration c, I computed the mean and standard deviation of the predicted ensemble. Figure 6.9 summarizes the resulting dose response profile. The mean A_{90} exhibited a smooth monotonic increase with concentration, reflecting progressive I_{Kr} inhibition, while the predicted standard deviation also increased with concentration, indicating enhanced cell-to-cell variability in repolarization under stronger block.

The predicted dose response curve generated from the 30 nM parameter population reveals several important features of dofetilide induced repolarization changes. First, the monotonic concentration AP duration relation is consistent with the expected pharmacology of I_{Kr} block, confirming that the parameter sets calibrated at 30 nM capture the dominant determinants of repolarization across a broad range of drug concentrations. Second, the widening of the predicted A_{90} distribution at higher concentrations reflects an amplification of intrinsic cell-to-cell variability. This behaviour is well aligned with experimental observations of increasing AP duration dispersion under strong I_{Kr} block, and with theoretical analyses of nonlinear repolarization sensitivity. Importantly, the ability of the 30 nM parameter ensemble to predict both the mean trend and the variance structure across unobserved concentrations supports the utility of intermediate strength perturbations for generating transferable electrophysiological parameter populations. These results further highlight that moderately blocked regimes provide the best balance between model identifiability and physiological relevance, enabling robust extrapolation to concentrations that were not experimentally measured.

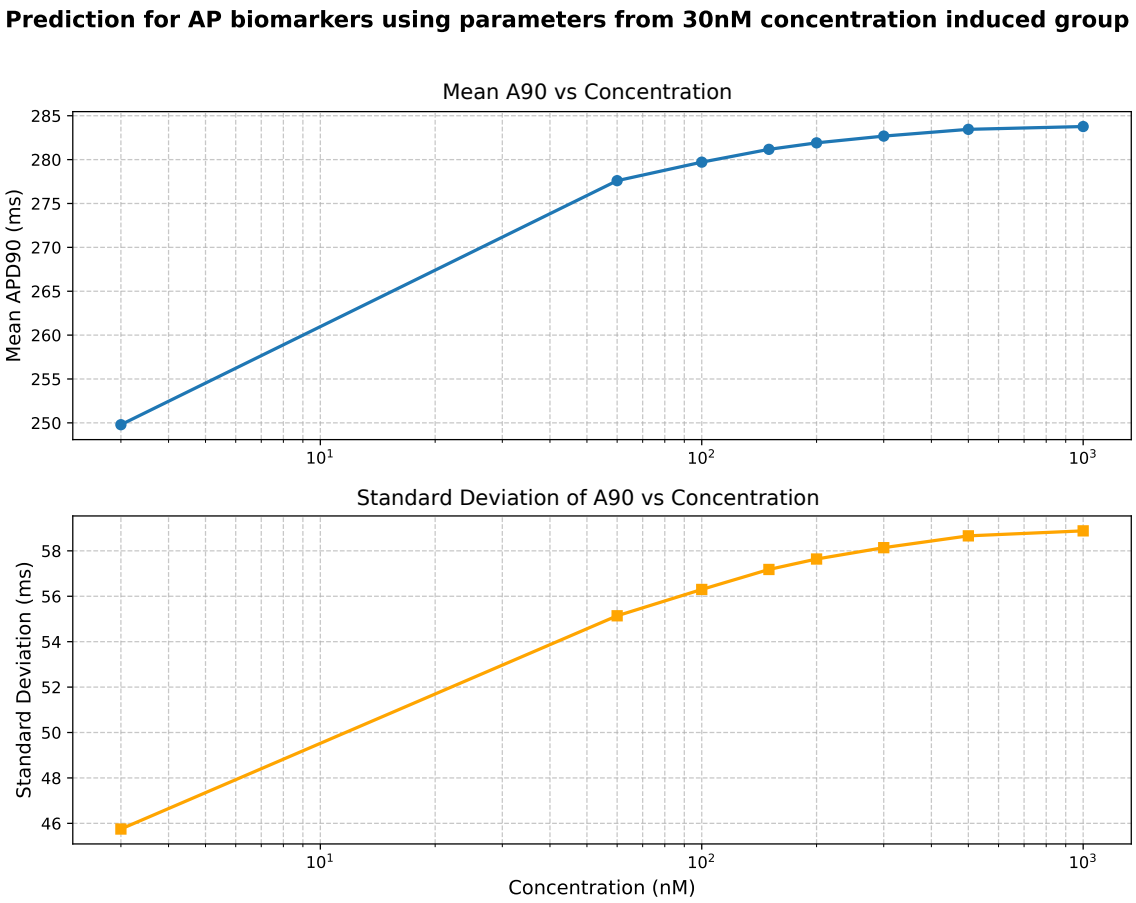

Figure 6.9: Predicted A_{90} dose response curve using the 30 nM parameter population. The 30 nM parameter ensemble was used as a generative model to simulate A_{90} distributions across dofetilide concentrations ranging from 1 to 1000 nM. For each concentration c, the unblocked fraction of I_{Kr} was determined from the Hill equation from [42] with Hill coefficient $n = 0.9$, and I_{Kr} parameters were scaled accordingly. (**Top**) Mean A_{90} as a function of concentration, showing a smooth monotonic increase with progressive I_{Kr} inhibition. (**Bottom**) Standard deviation of the predicted A_{90} distribution, revealing increased dispersion under stronger block. Together, the predictions demonstrate the ability of the 30 nM calibrated model to extrapolate reliably to previously untested drug concentrations.

6.4 Conclusion

In this chapter, I developed and applied a simultaneous parameter estimation framework to infer cell-specific electrophysiological properties and drug-response characteristics from paired AP recordings obtained before and after dofetilide exposure. Building on the single-condition fitting approach introduced in earlier chapters, I extended the inference procedure to explicitly incorporate pharmacological perturbation by modelling dofetilide action as a fractional block of the rapid delayed rectifier potassium current, I_{Kr}. The internal electrophysiological state of each cell was represented using the Shannon ventricular myocyte model, with a subset of ionic current parameters selected for estimation alongside a drug action parameter, φ.

Cell-specific parameters were inferred by fitting the model simultaneously to paired baseline and post-drug APs using a likelihood-based approach and gradient-

free global optimization. This simultaneous fitting strategy exploits the shared internal state of each cell across conditions while allowing drug-induced effects to be isolated in a mechanistically interpretable manner. I applied the framework to paired recordings obtained at multiple dofetilide concentrations and demonstrated that the resulting models accurately reproduce both baseline and drug-modified AP morphologies across a heterogeneous population of cells.

To assess the robustness of the inferred parameters, I performed a detailed procedural uncertainty analysis involving repeated optimizations from randomized initial conditions and perturbed voltage constraints. I further examined the predictive capability of the inferred drug-response parameters by using models calibrated at a single concentration to predict responses at other concentrations.

Headline results The simultaneous fitting framework consistently yielded high-quality fits to paired experimental recordings, with inferred parameters that were robust to substantial perturbations in optimization initialization values. Procedural uncertainty was small for the majority of parameters, with median relative discrepancies below 3% across repeated fits, and even smaller differences observed for parameters directly governing repolarization and drug response, including α_{Kr}, α_{Ks}, and the drug action parameter φ. Occasional large discrepancies were confined to a small subset of secondary parameters and were associated with alternative parameter combinations that generate nearly indistinguishable AP waveforms.

The estimated drug action parameter value ϕ exhibited substantial variability across cells, revealing pronounced population-level heterogeneity in the degree of I_{Kr} block induced by dofetilide. While the inferred distributions were consistent with established pharmacodynamics, especially [42], the divergence between their mean, median, and mode underscores the importance of characterizing drug effects using full distributional information rather than single-point summary statistics. Importantly, despite residual uncertainty in individual ionic current parameter scalings, ϕ remained practically identifiable within the simultaneous fitting framework, highlighting the advantage of paired baseline and post-drug recordings in constraining pharmacodynamic effects. I also note that initial condition uncertainty, arising from estimating parameters on single, non-prepaced APs, was mitigated in our framework.

In previous work (Section 5.3.4.1), non-prepaced parameters were converted to physiologically meaningful "prepaced" values via a common cell-specific scaling factor. In the current drug-response context, the inferred parameter ϕ, expressed as the ratio of I_{Kr} parameter post- versus pre-drug, further reduces sensitivity to initial condition variability. Because ϕ is computed as a ratio within the same cell, global multiplicative shifts in parameters cancel out, making ϕ substantially more robust than absolute estimates. Consequently, our dose-response inferences remain more reliable even under substantial initial condition uncertainty. Furthermore, using populations of models inferred at a single concentration, I demonstrated successful prediction of AP responses at nearby concentrations, with the most accurate and robust predictions obtained when inference was performed at an intermediate concentration (30 nM). These results indicate that calibration at an appropriately chosen perturbation level can capture drug-response characteristics that generalize across conditions.

Overall, the findings demonstrate that paired electrophysiological recordings substantially enhance parameter identifiability and enable robust inference of drug effects at the single-cell level, even in the presence of intrinsic biological variability and model non-uniqueness.

Limitations, extensions, and future directions Several limitations of the present study suggest avenues for future work. First, parameter estimation was performed using paired AP waveforms recorded at a fixed pacing rate, which limits the ability to constrain dynamic properties such as rate dependence and restitution. Incorporating multiple pacing frequencies, dynamic stimulation protocols, or trains of APs would provide additional information to further reduce parameter uncertainty, albeit at increased computational cost.

Second, drug action was represented using a simplified fractional block model acting on a single ionic current. While appropriate for dofetilide, which is a highly selective I_{Kr} blocker, extension to less selective compounds will require more complex pharmacodynamic formulations, potentially involving multiple currents or state-dependent binding, as indicated in [46]. Incorporating voltage-clamp data or complementary pharmacological measurements could further constrain such models.

More generally, while the fitting procedure substantially improves practical iden-

tifiability, the parameter estimation problem remains formally non-unique. Future work could address this by incorporating additional experimental modalities, such as calcium transient recordings, restitution measurements, or selective ion channel blockade, to further restrict the feasible parameter space. Alternative electrophysiological models and model selection strategies may also be explored to assess structural uncertainty.

Finally, the methodology presented here provides a foundation for population-based drug safety assessment using cell-specific digital twins. Extending the approach to additional compounds, broader concentration ranges, and human-derived cardiomyocytes represents a natural next step toward predictive, mechanism-based evaluation of pro-arrhythmic risk.

Chapter 7

Summary

7.1 Summary of Results, Strengths and Limitations

This thesis explores aspects of a central challenge in computational cardiac electrophysiology, namely the development and application of mechanistic AP models that are biophysically interpretable and capable of representing inter-cellular variability, with particular attention to their response under pharmacological perturbation. Through three closely related studies, this work contributes methodological and practical insights linking parameter sensitivity analysis, cell-specific model calibration, and drug-response modelling.

In Chapter 4, a comprehensive global Sobol sensitivity analysis of the Shannon rabbit ventricular myocyte model was performed to identify the ionic current conductances that most strongly govern variability in key electrophysiological AP biomarkers. Unlike previous studies relying on local perturbations around baseline parameters, this analysis quantified parameter influence across a broad physiological space and explicitly accounted for nonlinear interactions. A central and unexpected finding was the dominant role of the background chloride current, alongside a small subset of potassium and calcium-related conductances, in shaping AP duration and morphology. Crucially, these results demonstrated that a high-dimensional ionic model can be systematically reduced to a low-dimensional representation without substantial loss

of predictive accuracy. This provided not only mechanistic insight into repolarisation control but also a principled basis for parameter selection in subsequent parameter inference tasks.

Building directly on this foundation, Chapter 5 introduced a feasible methodology for constructing a large population of cell-specific AP models calibrated to fluorescence voltage recordings from over 1,200 rabbit ventricular myocytes. Rather than treating variability statistically at the population level alone, this work established a one-to-one correspondence between individual experimental cells and their fitted model representations. By fitting full AP waveforms, rather than isolated biomarkers, the resulting models captured the rich diversity of observed electrophysiological behaviour while preserving biophysical interpretability. Analysis of the inferred parameter distributions revealed that consistent AP phenotypes can emerge from complex and weakly correlated ionic conductances, revealing that cellular electrophysiology is governed by interacting mechanisms rather than single dominant parameters. This chapter demonstrated, for the first time at this large scale, that high-throughput, cell-level model personalization from optical voltage data is both feasible and useful.

Chapter 6 extended this personalized modelling framework into the pharmacological domain by developing a novel approach to mechanistic drug modelling based on paired AP recordings obtained from the same biological cell before and after drug application. Focusing on the clinically important I_{Kr} blocker dofetilide, this work introduced a simultaneous parameter estimation strategy that simultaneously inferred baseline ionic conductances and drug-induced inhibition factors. This paired data approach represents a significant methodological advance over traditional workflows that rely on population-averaged drug response curves or externally prescribed inhibition parameters. The results showed strong predictive performance at lower drug concentrations, especially 30nM, and revealed increasing variability at higher doses, highlighting both the strengths and current limits of conductance-based drug modelling. Importantly, this study enabled a direct comparison of published dofetilide I_{Kr} block values by assessing their consistency with paired experimental recordings and provided a rigorous test of whether conductances inferred from baseline data remain predictive under pharmacological perturbation, a critical requirement for transla-

tional in silico safety assessment.

Taken together, the contributions of this thesis advance the field in several key ways. First, it establishes a clear hierarchy of ionic importance in rabbit ventricular electrophysiology using a robust global sensitivity analysis framework. Second, it demonstrates a scalable and reproducible pipeline for generating large populations of cell-specific electrophysiological models from high-throughput experimental data. Third, it introduces a principled methodology for integrating paired drug-response measurements into mechanistic cardiac models, enabling direct inference and validation of pharmacodynamic effects at the single-cell level. Broadly, these advances move cardiac modelling beyond the paradigm of a single "representative" myocyte toward a framework that explicitly investigates biological variability while retaining predictive power.

Several limitations should be acknowledged. The modelling framework relies on a fixed underlying ionic structure and therefore inherits any assumptions and simplifications of the baseline Shannon model. Drug action was represented primarily through modulation of I_{Kr} conductance, which is appropriate for dofetilide but may not fully capture multi-channel drug effects at higher concentrations [46]. In addition, while fluorescence voltage recordings enable high-throughput measurements, they provide indirect measurements of membrane potential and do not directly constrain intracellular calcium or individual ionic currents. Nonetheless, these limitations do not undermine the central findings and they define clear and tractable directions for future refinement.

In conclusion, this thesis demonstrates that mechanistic cardiac AP models can be systematically simplified, individualized, and extended to drug-response prediction in a data-driven manner. By integrating sensitivity analysis, high-throughput parameter inference, and paired pharmacological modelling, this work provides a robust foundation for next generation in silico tools in cardiac safety pharmacology. As experimental datasets continue to grow in scale and richness, the approaches developed here position mechanistic modelling to play an increasingly central role in personalized medicine, early-stage drug evaluation, and the quantitative understanding of cardiac electrophysiological variability.

7.2 Future Work

The results of Chapters 4, 5, 6 highlight the significant role of cellular electrophysiological variability in shaping cardiac AP dynamics. In particular, sensitivity analysis and population-based modelling demonstrate that relatively small changes in ionic conductances can produce large variations in AP behaviour at the single-cell level. However, cardiac cells do not operate in isolation and instead, they form electrically coupled networks in which intercellular interactions critically modulate prominent behaviour.

Experimental and computational studies have shown that dispersion of repolarization is a key substrate for electrical instability and arrhythmia initiation, and that gap junction coupling plays a dual role by both stabilizing electrical activity and shaping spatial gradients in AP duration [6, 123]. Importantly, prior work suggests that the spatial arrangement of hyper responder cells, rather than their mere presence, can critically influence electrical dynamics [124]. Despite these advances, the interaction between intrinsic cellular heterogeneity and intercellular coupling remains incompletely understood, particularly in the context of spatially localized abnormalities.

Recent experimental evidence in acquired long QT syndrome further motivates this line of investigation. It has been shown that drug-induced prolongation of repolarization can lead to steep spatial gradients of AP duration, from which premature ventricular complexes (PVCs) may arise [125]. One plausible mechanism underlying this observation is that pharmacological intervention induces heterogeneous responses at the cellular level, such that a subset of cells effectively transitions from a normal responder to a hyper responder phenotype following drug exposure. When embedded in a coupled network, such mixed populations may naturally give rise to localized AP duration gradients capable of triggering ectopic activity.

Motivated by these findings, future work focuses on explicitly modelling networks of coupled normal responder and hyper responder cells to investigate how cellular heterogeneity, spatial organization, and coupling strength jointly shape AP dynamics. This approach provides a mechanistic bridge between single-cell variability identified

in earlier projects and tissue-level phenomena observed experimentally, offering a controlled framework for exploring how drug-induced cellular changes may translate into arrhythmogenic substrates.

References

[1] Z. Yang., H. Gao., S. R. D, and S. G. L, "Dominant ionic currents in rabbit ventricular action potential dynamics," *PLoS ONE*, vol. 20, no. 7, pp. 1–25, Jul. 2025. [Online]. Available: https://doi.org/10.1371/journal.pone.0328261 i, 1, 46, 83, 135

[2] R. D. Simitev, R. J. Gilchrist, Z. Yang, R. C. Myles, F. L. Burton, and G. L. Smith, "A large population of cell-specific action potential models replicating fluorescence recordings of voltage in rabbit ventricular myocytes," *Royal Society Open Science*, vol. 12, no. 3, p. 241539, 2025. [Online]. Available: https://doi.org/10.1098/rsos.241539 i, 2, 73, 76, 101, 102

[3] T. R. Shannon, F. Wang, J. Puglisi, C. Weber, and D. M. Bers, "A mathematical treatment of integrated ca dynamics within the ventricular myocyte," *Biophysical Journal*, vol. 87, no. 5, pp. 3351–3371, 2004. [Online]. Available: https://doi.org/10.1529/biophysj.104.047449 xii, 1, 3, 4, 6, 12, 34, 39, 40, 47, 48, 49, 60, 66, 68, 81, 83, 86, 88, 102, 116

[4] B. Amuzescu, R. Airini, F. B. Epureanu, S. A. Mann, T. Knott, and B. M. Radu, "Evolution of mathematical models of cardiomyocyte electrophysiology," *Math. Biosci.*, vol. 334, p. 108567, 2021. [Online]. Available: https://doi.org/10.1016/j.mbs.2021.108567 3, 12, 28, 84

[5] T. J. Snowden, P. H. van der Graaf, and M. J. Tindall, "Methods of model reduction for large-scale biological systems: A survey of current methods and trends," *Bulletin of Mathematical Biology*, vol. 79, no. 7, pp. 1449–1486, 2017. [Online]. Available: https://doi.org/10.1007/s11538-017-0277-2 3

[6] Q. Lachaud, M. H. N. Aziz, F. L. Burton, N. Macquaide, R. C. Myles, R. D. Simitev, and G. L. Smith, "Electrophysiological heterogeneity in large populations of rabbit ventricular cardiomyocytes," *Cardiovascular Research*, vol. 118, no. 15, pp. 3112–3125, 2022. [Online]. Available: http://dx.doi.org/10.1093/cvr/cvab375 3, 10, 12, 47, 48, 73, 80, 81, 96, 110, 145

[7] P. Gemmell, K. Burrage, B. Rodriguez, and T. A. Quinn, "Population of computational rabbit-specific ventricular action potential models for investigating sources of variability in cellular repolarisation," *PLoS ONE*, vol. 9, no. 2, p. e90112, 2014. [Online]. Available: http://dx.doi.org/10.1371/journal.pone.0090112 4, 66

[8] E. A. Sobie, "Parameter sensitivity analysis in electrophysiological models using multivariable regression," *Biophysical Journal*, vol. 96, no. 4, pp. 1264–1274, 2009. [Online]. Available: https://doi.org/10.1016/j.bpj.2008.10.056 4

[9] C. H. Luo and Y. Rudy, "A model of the ventricular cardiac action potential. depolarization, repolarization, and their interaction," *Circulation Research*, vol. 68, no. 6, pp. 1501–1526, 1991. [Online]. Available: http://dx.doi.org/10.1161/01.res.68.6.1501 4, 5

[10] J. J. Fox, J. L. McHarg, and R. F. Gilmour, Jr., "Ionic mechanism of electrical alternans," *American Journal of Physiology-Heart and Circulatory Physiology*, vol. 282, no. 2, pp. H516–H530, 2002. [Online]. Available: http://dx.doi.org/10.1152/ajpheart.00612.2001 4

[11] Y. Kurata, I. Hisatome, H. Matsuda, and T. Shibamoto, "Dynamical mechanisms of pacemaker generation in ik1-downregulated human ventricular myocytes: Insights from bifurcation analyses of a mathematical model," *Biophysical Journal*, vol. 89, no. 4, pp. 2865–2887, 2005. [Online]. Available: http://dx.doi.org/10.1529/biophysj.105.060830 4

[12] S. Coveney and R. H. Clayton, "Sensitivity and uncertainty analysis of two

human atrial cardiac cell models using gaussian process emulators," *Frontiers in Physiology*, vol. 11, 2020. [Online]. Available: http://dx.doi.org/10.3389/fphys.2020.00364 4, 41, 67

[13] M. Courtemanche, R. J. Ramirez, and S. Nattel, "Ionic mechanisms underlying human atrial action potential properties: insights from a mathematical model," *American Journal of Physiology-Heart and Circulatory Physiology*, vol. 275, no. 1, pp. H301–H321, 1998. [Online]. Available: http://dx.doi.org/10.1152/ajpheart.1998.275.1.H301 5, 7, 16

[14] M. M. Maleckar, J. L. Greenstein, W. R. Giles, and N. A. Trayanova, "K+ current changes account for the rate dependence of the action potential in the human atrial myocyte," *American Journal of Physiology-Heart and Circulatory Physiology*, vol. 297, no. 4, pp. H1398–H1410, 2009. [Online]. Available: http://dx.doi.org/10.1152/ajpheart.00411.2009 5

[15] L. Romero, E. Pueyo, M. Fink, and B. Rodríguez, "Impact of ionic current variability on human ventricular cellular electrophysiology," *American Journal of Physiology-Heart and Circulatory Physiology*, vol. 297, no. 4, pp. H1436–H1445, 2009. [Online]. Available: http://dx.doi.org/10.1152/ajpheart.00263.2009 5, 12, 28

[16] K. H. W. J. ten Tusscher and A. V. Panfilov, "Alternans and spiral breakup in a human ventricular tissue model," *American Journal of Physiology-Heart and Circulatory Physiology*, vol. 291, no. 3, pp. H1088–H1100, 2006. [Online]. Available: https://doi.org/10.1152/ajpheart.00109.2006 5, 6, 7, 8

[17] E. T. Y. Chang, M. Strong, and R. H. Clayton, "Bayesian sensitivity analysis of a cardiac cell model using a gaussian process emulator," *PLOS ONE*, vol. 10, no. 6, p. e0130252, 2015. [Online]. Available: http://dx.doi.org/10.1371/journal.pone.0130252 5

[18] L. Romero, B. Carbonell, B. Trenor, B. Rodríguez, J. Saiz, and J. M. Ferrero, "Systematic characterization of the ionic basis of rabbit cellular electrophysiology using two ventricular models," *Progress in Biophysics and*

Molecular Biology, vol. 107, no. 1, pp. 60–73, 2011. [Online]. Available: http://dx.doi.org/10.1016/j.pbiomolbio.2011.06.012 5, 9, 10, 48, 66

[19] A. Mahajan, Y. Shiferaw, D. Sato, A. Baher, R. Olcese, and ..., "A rabbit ventricular action potential model replicating cardiac dynamics at rapid heart rates," *Biophysical Journal*, vol. 94, no. 2, pp. 392–410, 2008. [Online]. Available: http://dx.doi.org/10.1529/biophysj.106.98160 6, 47, 73

[20] R. H. Johnstone *et al.*, "Uncertainty and variability in models of the cardiac action potential: Can we build trustworthy models?" *Journal of Molecular and Cellular Cardiology*, vol. 96, pp. 49–62, 2016. [Online]. Available: http://dx.doi.org/10.1016/j.yjmcc.2015.11.018 6, 41, 90, 104

[21] G. Del Corso, R. Verzicco, and F. Viola, "Sensitivity analysis of an electrophysiology model for the left ventricle," *Journal of The Royal Society Interface*, vol. 17, no. 171, p. 20200532, 2020. [Online]. Available: http://dx.doi.org/10.1098/rsif.2020.0532 6

[22] E. T. Chang and R. H. Clayton, "Uncertainty and sensitivity analysis of the courtemanche-ramirez-nattel human atrial cell model using gaussian process emulators," in *2015 Computing in Cardiology Conference (CinC)*. IEEE, 2015, pp. 857–860. [Online]. Available: http://dx.doi.org/10.1109/CIC.2015.7411046 7, 41

[23] P. Pathmanathan, J. M. Cordeiro, and R. A. Gray, "Comprehensive uncertainty quantification and sensitivity analysis for cardiac action potential models," *Frontiers in Physiology*, vol. 10, 2019. [Online]. Available: http://dx.doi.org/10.3389/fphys.2019.00721 7

[24] M. T. Mora, J. M. Ferrero, L. Romero, and B. Trenor, "Sensitivity analysis revealing the effect of modulating ionic mechanisms on calcium dynamics in simulated human heart failure," *PLOS ONE*, vol. 12, no. 11, p. e0187739, 2017. [Online]. Available: http://dx.doi.org/10.1371/journal.pone.0187739 8

[25] T. O'Hara, L. Virág, A. Varró, and Y. Rudy, "Simulation of the undiseased human cardiac ventricular action potential: Model formulation

and experimental validation," *PLoS Computational Biology*, vol. 7, no. 5, p. e1002061, 2011. [Online]. Available: http://dx.doi.org/10.1371/journal.pcbi.1002061 8, 9, 15, 18, 19, 20

[26] A. Sadrieh, S. A. Mann, R. N. Subbiah, L. Domanski, J. A. Taylor, J. I. Vandenberg, and A. P. Hill, "Quantifying the origins of population variability in cardiac electrical activity through sensitivity analysis of the electrocardiogram," *The Journal of Physiology*, vol. 591, no. 17, pp. 4207–4222, 2013. [Online]. Available: http://dx.doi.org/10.1113/jphysiol.2013.251710 8

[27] J. Parikh, P. Di Achille, J. Kozloski, and V. Gurev, "Global sensitivity analysis of ventricular myocyte model-derived metrics for proarrhythmic risk assessment," *Frontiers in Pharmacology*, vol. 10, p. 1054, 2019. [Online]. Available: https://doi.org/10.3389/fphar.2019.01054 9

[28] M. Renardy, C. Hult, S. Evans, J. J. Linderman, and D. E. Kirschner, "Global sensitivity analysis of biological multiscale models," *Current Opinion in Biomedical Engineering*, vol. 11, pp. 109–116, 2019. [Online]. Available: http://dx.doi.org/10.1016/j.cobme.2019.09.012 10

[29] I. M. Sobol, "Global sensitivity indices for nonlinear mathematical models and their monte carlo estimates," *Mathematics and Computers in Simulation*, vol. 55, no. 1-3, pp. 271–280, 2001. [Online]. Available: https://doi.org/10.1016/s0378-4754(00)00270-6 10, 41

[30] C. Antzelevitch, S. Sicouri, S. H. Litovsky, A. Lukas, S. C. Krishnan, J. M. Di Diego, G. A. Gintant, and D.-W. Liu, "Heterogeneity within the ventricular wall. electrophysiology and pharmacology of epicardial, endocardial, and m cells." *Circulation research*, vol. 69, no. 6, pp. 1427–1449, 1991. [Online]. Available: https://doi.org/10.1161/01.RES.69.6.1427 11, 27

[31] J. Feng, L. Yue, Z. Wang, and S. Nattel, "Ionic mechanisms of regional action potential heterogeneity in the canine right atrium," *Circulation research*, vol. 83, no. 5, pp. 541–551, 1998. [Online]. Available: https://doi.org/10.1161/01.RES.83.5.541 11, 27

[32] O. J. Britton, A. Bueno-Orovio, K. Van Ammel, H. R. Lu, R. Towart, D. J. Gallacher, and B. Rodriguez, "Experimentally calibrated population of models predicts and explains intersubject variability in cardiac cellular electrophysiology," *Proceedings of the National Academy of Sciences*, vol. 110, no. 23, pp. E2098–E2105, 2013. [Online]. Available: https://doi.org/10.1073/pnas.1304382110 11, 12, 27

[33] P.-C. Yang and C. E. Clancy, "In silico prediction of sex-based differences in human susceptibility to cardiac ventricular tachyarrhythmias," *Frontiers in physiology*, vol. 3, p. 360, 2012. [Online]. Available: https://doi.org/10.3389/fphys.2012.00360 11, 27

[34] D. G. Whittaker, M. Clerx, C. L. Lei, D. J. Christini, and G. R. Mirams, "Calibration of ionic and cellular cardiac electrophysiology models," *WIREs Systems Biology and Medicine*, vol. 12, no. 2, p. e1482, 2020. [Online]. Available: https://doi.org/10.1002/wsbm.1482 11

[35] H. Ni, S. Morotti, and E. Grandi, "A heart for diversity: simulating variability in cardiac arrhythmia research," *Frontiers in Physiology*, vol. 9, p. 958, 2018. [Online]. Available: https://doi.org/10.3389/fphys.2018.00958 11, 28, 30

[36] S. Dokos and N. H. Lovell, "Parameter estimation in cardiac ionic models," *Progress in Biophysics and Molecular Biology*, vol. 85, no. 2-3, pp. 407–431, 2004. [Online]. Available: https://doi.org/10.1016/j.pbiomolbio.2004.02.002 12, 29

[37] M. C. Müllenbroich, A. Kelly, C. Acker, G. Bub, T. Bruegmann, A. Di Bona, E. Entcheva, C. Ferrantini, P. Kohl, S. E. Lehnart *et al.*, "Novel optics-based approaches for cardiac electrophysiology: a review," *Frontiers in physiology*, vol. 12, p. 769586, 2021. [Online]. Available: https://doi.org/10.3389/fphys.2021.769586 12, 110

[38] P. Lee, L. Hou, F. J. Alibhai, R. Al-Attar, A. Simón-Chica, A. Redondo-Rodríguez, Y. Nie, M. Mirotsou, M. A. Laflamme, G. Swaminath *et al.*, "A fully-automated low-cost cardiac monolayer optical mapping robot," *Frontiers*

in Cardiovascular Medicine, vol. 10, p. 1096884, 2023. [Online]. Available: https://doi.org/10.3389/fcvm.2023.1096884 12

[39] S. Arridge, P. Maass, O. Öktem, and C. B. Schönlieb, "Solving inverse problems using data-driven models," *Acta Numerica*, vol. 28, pp. 1–174, 2019. [Online]. Available: https://doi.org/10.1017/S0962492919000059 12

[40] H. Rasmussen, M. Allen, K. Blackburn, G. Butrous, and H. Dalrymple, "Dofetilide, a novel class iii antiarrhythmic agent," *Journal of cardiovascular pharmacology*, vol. 20, pp. S96–S105, 1992. 13

[41] K. Tsujimae, S. Suzuki, S. Murakami, and Y. Kurachi, "Frequency-dependent effects of various I_{Kr} blockers on cardiac action potential duration in a human atrial model," *American Journal of Physiology-Heart and Circulatory Physiology*, vol. 293, no. 1, pp. H660–H669, 2007. [Online]. Available: https://doi.org/10.1152/ajpheart.01083.2006 13, 15, 21, 31, 123, 124, 125, 126

[42] Z. Li, S. Dutta, J. Sheng, P. N. Tran, W. Wu, K. Chang, T. Mdluli, D. G. Strauss, and T. Colatsky, "Improving the in silico assessment of proarrhythmia risk by combining herg (human ether-à-go-go-related gene) channel–drug binding kinetics and multichannel pharmacology," *Circulation: Arrhythmia and Electrophysiology*, vol. 10, no. 2, p. e004628, 2017. [Online]. Available: https://doi.org/10.1161/CIRCEP.116.004628 13, 15, 21, 31, 119, 123, 126, 137, 138, 139

[43] P. Groot-Kormelink, P. Tranter, and M. Gosling, "Maximising the efficiency and application of automated planar patch clamp electrophysiology-optimisation of cell-based reagents," *EUROPEAN PHARMACEUTICAL REVIEW*, vol. 12, no. 5, p. 39, 2007. 13

[44] J. Dunlop, M. Bowlby, R. Peri, D. Vasilyev, and R. Arias, "High-throughput electrophysiology: an emerging paradigm for ion-channel screening and physiology," *Nature reviews Drug discovery*, vol. 7, no. 4, pp. 358–368, 2008. [Online]. Available: https://doi.org/10.1038/nrd2552 13

[45] P. Lee, K. Wang, C. E. Woods, P. Yan, P. Kohl, P. Ewart, L. M. Loew, D. A. Terrar, and C. Bollensdorff, "Cardiac electrophysiological imaging systems scalable for high-throughput drug testing," *Pflügers Archiv-European Journal of Physiology*, vol. 464, no. 6, pp. 645–656, 2012. [Online]. Available: https://doi.org/10.1007/s00424-012-1149-0 13

[46] Z. Li, B. J. Ridder, X. Han, W. W. Wu, J. Sheng, P. N. Tran, M. Wu, A. Randolph, R. H. Johnstone, G. R. Mirams *et al.*, "Assessment of an in silico mechanistic model for proarrhythmia risk prediction under the ci pa initiative," *Clinical Pharmacology & Therapeutics*, vol. 105, no. 2, pp. 466–475, 2019. [Online]. Available: https://doi.org/10.1002/cpt.1184 16, 140, 144

[47] S. Dutta, K. C. Chang, K. A. Beattie, J. Sheng, P. N. Tran, W. W. Wu, M. Wu, D. G. Strauss, T. Colatsky, and Z. Li, "Optimization of an in silico cardiac cell model for proarrhythmia risk assessment," *Frontiers in Physiology*, vol. 8, p. 616, 2017. [Online]. Available: https://doi.org/10.3389/fphys.2017.00917 17, 19

[48] S. A. Mann, M. Imtiaz, A. Winbo, A. Rydberg, M. D. Perry, J.-P. Couderc, B. Polonsky, S. McNitt, W. Zareba, A. P. Hill *et al.*, "Convergence of models of human ventricular myocyte electrophysiology after global optimization to recapitulate clinical long qt phenotypes," *Journal of molecular and cellular cardiology*, vol. 100, pp. 25–34, 2016. [Online]. Available: https://doi.org/10.1016/j.yjmcc.2016.09.011 17

[49] T. Krogh-Madsen, A. F. Jacobson, F. A. Ortega, and D. J. Christini, "Global optimization of ventricular myocyte model to multi-variable objective improves predictions of drug-induced torsades de pointes," *Frontiers in Physiology*, vol. 8, p. 1059, 2017. [Online]. Available: https://doi.org/10.3389/fphys.2017.01059 18

[50] C. T. Bot, A. R. Kherlopian, F. A. Ortega, D. J. Christini, and T. Krogh-Madsen, "Rapid genetic algorithm optimization of a mouse computational model: benefits for anthropomorphization of neonatal mouse

cardiomyocytes," *Frontiers in physiology*, vol. 3, p. 421, 2012. [Online]. Available: https://doi.org/10.3389/fphys.2012.00421 20

[51] S. V. Pandit, R. B. Clark, W. R. Giles, and S. S. Demir, "A mathematical model of action potential heterogeneity in adult rat left ventricular myocytes," *Biophysical journal*, vol. 81, no. 6, pp. 3029–3051, 2001. [Online]. Available: https://doi.org/10.1016/S0006-3495(01)75943-7 20

[52] D. J. Snyders and A. Chaudhary, "High affinity open channel block by dofetilide of herg expressed in a human cell line." *Molecular pharmacology*, vol. 49, no. 6, pp. 949–955, 1996. [Online]. Available: https://doi.org/10.1016/S0026-895X(25)09019-4 21, 123, 126

[53] T. Brennan, M. Fink, and B. Rodriguez, "Multiscale modelling of drug-induced effects on cardiac electrophysiological activity," *European Journal of Pharmaceutical Sciences*, vol. 36, no. 1, pp. 62–77, 2009. [Online]. Available: https://doi.org/10.1016/j.ejps.2008.09.013 21, 116

[54] W. J. Crumb Jr, J. Vicente, L. Johannesen, and D. G. Strauss, "An evaluation of 30 clinical drugs against the comprehensive in vitro proarrhythmia assay (cipa) proposed ion channel panel," *Journal of pharmacological and toxicological methods*, vol. 81, pp. 251–262, 2016. [Online]. Available: https://doi.org/10.1016/j.vascn.2016.03.009 21, 31, 123, 126

[55] J. Kramer, C. A. Obejero-Paz, G. Myatt, Y. A. Kuryshev, A. Bruening-Wright, J. S. Verducci, and A. M. Brown, "MICE models: superior to the herg model in predicting torsade de pointes," *Scientific reports*, vol. 3, no. 1, p. 2100, 2013. [Online]. Available: https://doi.org/10.1038/srep02100 21, 31, 109, 110, 123, 126

[56] J. Sundnes, G. T. Lines, X. Cai, B. F. Nielsen, K.-A. Mardal, and A. Tveito, *Computing the electrical activity in the heart*. Springer Science & Business Media, 2007, vol. 1. [Online]. Available: https://doi.org/10.1007/3-540-33437-8 23, 24, 25

[57] F. H. Martini, J. L. Nath, and E. F. Bartholomew, "Anatomy and physiology," 2005. 24

[58] C. A. Souders, S. L. Bowers, and T. A. Baudino, "Cardiac fibroblast: the renaissance cell," *Circulation research*, vol. 105, no. 12, pp. 1164–1176, 2009. [Online]. Available: https://doi.org/10.1161/CIRCRESAHA.109.209809 24

[59] S. Chen and S. Cohen, "Chapter 18 - principles of cardiovascular tissue engineering," in *Tissue Engineering (Third Edition)*, third edition ed., J. De Boer, C. A. Blitterswijk, J. A. Uquillas, and N. Malik, Eds. Academic Press, 2023, pp. 629–660. [Online]. Available: https://www.sciencedirect.com/science/article/pii/B9780128244593000184 24

[60] J. Keener and J. Sneyd, *Mathematical physiology 1: Cellular physiology*. Springer New York, NY, USA, 2009, vol. 2. 25, 33, 34

[61] F. B. Sachse, *Computational cardiology: modeling of anatomy, electrophysiology, and mechanics*. Springer Science & Business Media, 2004, vol. 2966. [Online]. Available: https://doi.org/10.1007/b96841 25, 27

[62] R. L. Winslow, J. Rice, S. Jafri, E. Marban, and B. O'Rourke, "Mechanisms of altered excitation-contraction coupling in canine tachycardia-induced heart failure, ii: model studies," *Circulation research*, vol. 84, no. 5, pp. 571–586, 1999. [Online]. Available: https://doi.org/10.1161/01.res.84.5.571 26

[63] E. Passini, A. Mincholé, R. Coppini, E. Cerbai, B. Rodriguez, S. Severi, and A. Bueno-Orovio, "Mechanisms of pro-arrhythmic abnormalities in ventricular repolarisation and anti-arrhythmic therapies in human hypertrophic cardiomyopathy," *Journal of Molecular and Cellular Cardiology*, vol. 96, pp. 72–81, 2016. [Online]. Available: https://doi.org/10.1016/j.yjmcc.2015.09.003 27

[64] X. Zhou, A. Bueno-Orovio, M. Orini, B. Hanson, M. Hayward, P. Taggart, P. D. Lambiase, K. Burrage, and B. Rodriguez, "In vivo and in silico investigation into mechanisms of frequency dependence of repolarization alternans in human

ventricular cardiomyocytes," *Circulation Research*, vol. 118, no. 2, pp. 266–278, 2016. [Online]. Available: https://doi.org/10.1161/circresaha.115.307836 27

[65] M. Niepel, S. L. Spencer, and P. K. Sorger, "Non-genetic cell-to-cell variability and the consequences for pharmacology," *Current Opinion in Chemical Biology*, vol. 13, no. 5-6, pp. 556–561, 2009. [Online]. Available: https://doi.org/10.1016/j.cbpa.2009.09.015 27

[66] C. L. Lei *et al.*, "Considering discrepancy when calibrating a mechanistic electrophysiology model," *Philosophical Transactions of the Royal Society A*, vol. 378, no. 2173, p. 20190349, 2020. [Online]. Available: https://doi.org/10.1098/rsta.2019.0349 28, 30

[67] R. Winslow, S. Cortassa, B. O'Rourke, Y. L. Hashambhoy, J. J. Rice, and J. L. Greenstein, "Integrative modeling of the cardiac ventricular myocyte," *WIREs Systems Biology and Medicine*, vol. 3, no. 4, pp. 392–413, 2011. [Online]. Available: https://doi.org/10.1002/wsbm.122 28

[68] A. Muszkiewicz, O. J. Britton, P. Gemmell, E. Passini, C. Sánchez, X. Zhou, and A. Carusi, "Variability in cardiac electrophysiology: using experimentally-calibrated populations of models to move beyond the single virtual physiological human paradigm," *Progress in Biophysics and Molecular Biology*, vol. 120, no. 1-3, pp. 115–127, 2016. [Online]. Available: https://doi.org/10.1016/j.pbiomolbio.2015.12.002 28

[69] S. Morotti and E. Grandi, "Logistic regression analysis of populations of electrophysiological models to assess proarrhythmic risk," *MethodsX*, vol. 4, pp. 25–34, 2017. [Online]. Available: https://doi.org/10.1016/j.mex.2016.12.002 29

[70] Z. Syed, E. Vigmond, S. Nattel, and L. J. Leon, "Atrial cell action potential parameter fitting using genetic algorithms," *Medical and Biological Engineering and Computing*, vol. 43, no. 5, pp. 561–571, 2005. [Online]. Available: https://doi.org/10.1007/bf02351029 29

[71] C. T. Bot, A. R. Kherlopian, F. A. Ortega, D. J. Christini, and T. Krogh-Madsen, "Rapid genetic algorithm optimization of a mouse computational model: benefits for anthropomorphization of neonatal mouse cardiomyocytes," *Frontiers in Physiology*, vol. 3, p. 421, 2012. [Online]. Available: https://doi.org/10.3389/fphys.2012.00421 29

[72] W. Groenendaal, F. A. Ortega, A. R. Kherlopian, A. C. Zygmunt, T. Krogh-Madsen, and D. J. Christini, "Cell-specific cardiac electrophysiology models," *PLoS Computational Biology*, vol. 11, no. 4, p. e1004242, 2015. [Online]. Available: https://doi.org/10.1371/journal.pcbi.1004242 29

[73] T. Krogh-Madsen and D. J. Christini, "Slow $[Na^+]_i$ dynamics impacts arrhythmogenesis and spiral wave reentry in cardiac myocyte ionic model," *Chaos: An Interdisciplinary Journal of Nonlinear Science*, vol. 27, no. 9, 2017. [Online]. Available: https://doi.org/10.1063/1.4999475 29, 62

[74] M. Aziz and R. D. Simitev, "Estimation of parameters for an archetypal model of cardiomyocyte membrane potentials," *International Journal of Bioautomation*, vol. 26, no. 3, pp. 255–272, 2022. [Online]. Available: https://doi.org/10.7546/ijba.2022.26.3.000832 29

[75] M. Lei, L. Wu, D. A. Terrar, and C. L.-H. Huang, "Modernized classification of cardiac antiarrhythmic drugs," *Circulation*, vol. 138, no. 17, pp. 1879–1896, 2018. [Online]. Available: https://doi.org/10.1161/CIRCULATIONAHA.118.035455 30

[76] R. FitzHugh, "Impulses and physiological states in theoretical models of nerve membrane," *Biophysical journal*, vol. 1, no. 6, pp. 445–466, 1961. [Online]. Available: https://doi.org/10.1016/s0006-3495(61)86902-6 33

[77] A. L. Hodgkin, A. F. Huxley, and B. Katz, "Measurement of current-voltage relations in the membrane of the giant axon of loligo," *The Journal of physiology*, vol. 116, no. 4, p. 424, 1952. [Online]. Available: https://doi.org/10.1113/jphysiol.1952.sp004716 33, 38

[78] D. Noble, "A modification of the hodgkin—huxley equations applicable to purkinje fibre action and pacemaker potentials," *The Journal of physiology*, vol. 160, no. 2, p. 317, 1962. [Online]. Available: https://doi.org/10.1113/jphysiol.1962.sp006849 33

[79] Physiome Project, "Shannon, wang, puglisi, weber, bers, 2004 – cellml model repository." [Online]. Available: https://models.physiomeproject.org/exposure/d72a36fe0b7e121068c96bcb1ff6044a/shannon_wang_puglisi_weber_bers_2004_a.cellml/view 40

[80] I. M. Sobol, "Uniformly distributed sequences with an additional uniform property," *USSR Computational Mathematics and Mathematical Physics*, vol. 16, no. 5, pp. 236–242, 1976. [Online]. Available: https://doi.org/10.1016/0041-5553(76)90154-3 40, 49, 52

[81] A. Tarantola, *Inverse Problem Theory and Methods for Model Parameter Estimation*. SIAM, 2005. 43

[82] E. Marder and J.-M. Goaillard, "Variability, compensation, and homeostasis in neuron and network function," *Nature Reviews Neuroscience*, vol. 7, pp. 563–574, 2006. [Online]. Available: https://doi.org/10.1038/nrn1949 43

[83] N. Hansen, S. D. Müller, and P. Koumoutsakos, "Reducing the time complexity of the derandomized evolution strategy with covariance matrix adaptation (cma-es)," *Evolutionary computation*, vol. 11, no. 1, pp. 1–18, 2003. [Online]. Available: https://doi.org/10.1162/106365603321828970 43, 83

[84] T. Glasmachers, T. Schaul, S. Yi, D. Wierstra, and J. Schmidhuber, "Exponential natural evolution strategies," in *Proceedings of the 12th annual conference on Genetic and evolutionary computation*, 2010, pp. 393–400. [Online]. Available: https://doi.org/10.1145/1830483.1830557 43, 44, 118

[85] M. Clerx, M. Robinson, B. Lambert, C. L. Lei, S. Ghosh, G. R. Mirams, and D. J. Gavaghan, "Probabilistic inference on noisy time series (pints)," *arXiv preprint arXiv:1812.07388*, 2018. [Online]. Available: https://doi.org/10.5334/jors.252 44, 83, 91, 118

[86] C. M. Lloyd, J. R. Lawson, P. J. Hunter, and P. F. Nielsen, "The cellml model repository," *Bioinformatics*, vol. 24, no. 18, pp. 2122–2123, 2008. [Online]. Available: http://dx.doi.org/10.1093/bioinformatics/btn390 48

[87] M. Clerx, P. Collins, E. de Lange, and P. G. Volders, "Myokit: A simple interface to cardiac cellular electrophysiology," *Progress in Biophysics and Molecular Biology*, vol. 120, no. 1-3, pp. 100–114, 2016. [Online]. Available: http://dx.doi.org/10.1016/j.pbiomolbio.2015.12.008 48

[88] A. C. Hindmarsh, P. N. Brown, K. E. Grant, S. L. Lee, R. Serban, D. E. Shumaker, and C. S. Woodward, "Sundials: Suite of nonlinear and differential/algebraic equation solvers," *ACM Transactions on Mathematical Software*, vol. 31, no. 3, pp. 363–396, 2005. [Online]. Available: http://dx.doi.org/10.1145/1089014.1089020 48

[89] M. J. Jansen, "Analysis of variance designs for model output," *Computer Physics Communications*, vol. 117, no. 1-2, pp. 35–43, 1999. [Online]. Available: http://dx.doi.org/10.1016/S0010-4655(98)00154-4 52

[90] J. Herman and W. Usher, "SALib: An open-source python library for sensitivity analysis," *The Journal of Open Source Software*, vol. 2, no. 9, 2017. [Online]. Available: https://doi.org/10.21105/joss.00097 53

[91] B. Efron and R. J. Tibshirani, *An introduction to the bootstrap*. New York, NY: Chapman and Hall, 1993. [Online]. Available: https://doi.org/10.1201/9780429246593 53

[92] Z. Qu, G. Hu, A. Garfinkel, and J. N. Weiss, "Nonlinear and stochastic dynamics in the heart," *Physics reports*, vol. 543, no. 2, pp. 61–162, 2014. [Online]. Available: https://doi.org/10.1016/j.physrep.2014.05.002 56

[93] M. C. Cross and P. C. Hohenberg, "Pattern formation outside of equilibrium," *Reviews of Modern Physics*, vol. 65, no. 3, pp. 851–1112, 1993. [Online]. Available: http://dx.doi.org/10.1103/RevModPhys.65.851 57

[94] J. Nossent, P. Elsen, and W. Bauwens, "Sobol'sensitivity analysis of a complex environmental model," *Environmental modelling & software*, vol. 26, no. 12, pp. 1515–1525, 2011. [Online]. Available: https://doi.org/10.1016/j.envsoft.2011.08.010 62

[95] E. Grandi, S. V. Pandit, N. Voigt, A. J. Workman, D. Dobrev, J. Jalife, and D. M. Bers, "Human atrial action potential and ca2+ model: sinus rhythm and chronic atrial fibrillation," *Circulation Research*, vol. 109, no. 9, pp. 1055–1066, 2011. [Online]. Available: https://doi.org/10.1161/CIRCRESAHA.111.253955 62

[96] D. Duan, "Phenomics of cardiac chloride channels: the systematic study of chloride channel function in the heart," *The Journal of Physiology*, vol. 587, no. 10, pp. 2163–2177, 2009. [Online]. Available: http://dx.doi.org/10.1113/jphysiol.2008.165860 62

[97] M. Hiraoka, "Role of cardiac chloride currents in changes in action potential characteristics and arrhythmias," *Cardiovascular Research*, vol. 40, no. 1, pp. 23–33, 1998. [Online]. Available: http://dx.doi.org/10.1016/s0008-6363(98)00173-4 62, 66

[98] E. Carmeliet, "K+channels and control of ventricular repolarization in the heart," *Fundamental & Clinical Pharmacology*, vol. 7, no. 1, pp. 19–28, 1993. [Online]. Available: http://dx.doi.org/10.1111/j.1472-8206.1993.tb00214.x 62

[99] A. Varró, D. A. Lathrop, S. B. Hester, P. P. Nánási, and J. G. Y. Papp, "Ionic currents and action potentials in rabbit, rat, and guinea pig ventricular myocytes," *Basic Research in Cardiology*, vol. 88, no. 2, pp. 93–102, 1993. [Online]. Available: https://doi.org/10.1007/bf00798257 62

[100] X. Wu and H. P. Larsson, "Insights into cardiac iks (kcnq1/kcne1) channels regulation," *International Journal of Molecular Sciences*, vol. 21, no. 24, p. 9440, 2020. [Online]. Available: https://doi.org/10.3390/ijms21249440 63

[101] A. S. Dhamoon and J. Jalife, "The inward rectifier current (ik1) controls cardiac excitability and is involved in arrhythmogenesis," *Heart*

Rhythm, vol. 2, no. 3, pp. 316–324, 2005. [Online]. Available: http://dx.doi.org/10.1016/j.hrthm.2004.11.012 63

[102] Y. Shimoni, R. B. Clark, and W. R. Giles, "Role of an inwardly rectifying potassium current in rabbit ventricular action potential," *The Journal of Physiology*, vol. 448, no. 1, pp. 709–727, 1992. [Online]. Available: https://doi.org/10.1113/jphysiol.1992.sp019066 63

[103] N. Niwa and J. M. Nerbonne, "Molecular determinants of cardiac transient outward potassium current (ito) expression and regulation," *Journal of molecular and cellular cardiology*, vol. 48, no. 1, pp. 12–25, 2010. [Online]. Available: https://doi.org/10.1016/j.yjmcc.2009.07.013 63

[104] K. Linz and R. Meyer, "Profile and kinetics of l-type calcium current during the cardiac ventricular action potential compared in guinea-pigs, rats and rabbits," *Pflügers Archiv*, vol. 439, no. 5, pp. 588–599, 2000. [Online]. Available: http://dx.doi.org/10.1007/s004249900212 63

[105] M. J. Shattock *et al.*, "Na+/ca2+ exchange and na+/k+-atpase in the heart," *The Journal of Physiology*, vol. 593, no. 6, pp. 1361–1382, 2015. [Online]. Available: https://doi.org/10.1113/jphysiol.2014.282319 63

[106] C. R. Weber, V. Piacentino, K. S. Ginsburg, S. R. Houser, and D. M. Bers, "Na+-ca2+ exchange current and submembrane [ca2+] during the cardiac action potential," *Circulation Research*, vol. 90, no. 2, pp. 182–189, 2002. [Online]. Available: https://doi.org/10.1161/hh0202.103940 63

[107] O. J. Britton, A. Bueno-Orovio, L. Virág, A. Varró, and B. Rodriguez, "The electrogenic na+/k+ pump is a key determinant of repolarization abnormality susceptibility in human ventricular cardiomyocytes: A population-based simulation study," *Frontiers in Physiology*, vol. 8, 2017. [Online]. Available: http://dx.doi.org/10.3389/fphys.2017.00278 63

[108] R. M. Shaw and Y. Rudy, "Ionic mechanisms of propagation in cardiac tissue: Roles of the sodium and l-type calcium currents during reduced excitability

and decreased gap junction coupling," *Circulation Research*, vol. 81, no. 5, pp. 727–741, 1997. [Online]. Available: https://doi.org/10.1161/01.res.81.5.727 64

[109] N. Jost *et al.*, "Restricting excessive cardiac action potential and qt prolongation: A vital role for i ks in human ventricular muscle," *Circulation*, vol. 112, no. 10, pp. 1392–1399, 2005. [Online]. Available: http://dx.doi.org/10.1161/CIRCULATIONAHA.105.550111 66

[110] M. Varshneya, X. Mei, and E. A. Sobie, "Prediction of arrhythmia susceptibility through mathematical modeling and machine learning," *Proceedings of the National Academy of Sciences*, vol. 118, no. 37, 2021. [Online]. Available: https://doi.org/10.1073/pnas.2104019118 67

[111] K. Y. Bogdanov, T. M. Vinogradova, and E. G. Lakatta, "Sinoatrial nodal cell ryanodine receptor and na+-ca2+ exchanger: molecular partners in pacemaker regulation," *Circulation Research*, vol. 88, no. 12, pp. 1254–1258, 2001. [Online]. Available: https://doi.org/10.1161/hh1201.092095 67

[112] J. Winter and M. J. Shattock, "Geometrical considerations in cardiac electrophysiology and arrhythmogenesis," *Europace*, vol. 18, no. 3, pp. 320–331, 2016. [Online]. Available: https://doi.org/10.1093/europace/euv307 70

[113] K. Csilléry, M. G. Blum, O. E. Gaggiotti, and O. François, "Approximate bayesian computation (abc) in practice," *Trends in ecology & evolution*, vol. 25, no. 7, pp. 410–418, 2010. [Online]. Available: https://doi.org/10.1016/j.tree.2010.04.001 73

[114] J. Skilling, "Nested sampling for general bayesian computation," 2006. [Online]. Available: https://doi.org/10.1214/06-BA127 73

[115] W. H. Press, *Numerical recipes 3rd edition: The art of scientific computing*. Cambridge university press, 2007. [Online]. Available: https://doi.org/10.5555/1403886 79, 88

[116] V. N. Biktashev, R. Suckley, Y. E. Elkin, and R. D. Simitev, "Asymptotic analysis and analytical solutions of a model of cardiac excitation," *Bulletin of mathematical biology*, vol. 70, no. 2, pp. 517–554, 2008. [Online]. Available: https://doi.org/10.1007/s11538-007-9267-0 84

[117] R. Bardenet, O. Cappé, G. Fort, and B. Kégl, "Adaptive mcmc with online relabeling," 2015. [Online]. Available: https://doi.org/10.3150/13-bej578 91

[118] M. McIntosh, S. Cobbe, and G. Smith, "Heterogeneous changes in action potential and intracellular ca2+ in left ventricular myocyte sub-types from rabbits with heart failure," *Cardiovascular research*, vol. 45, no. 2, pp. 397–409, 2000. [Online]. Available: https://doi.org/10.1016/S0008-6363(99)00360-0 102, 103

[119] A. Baartscheer, C. A. Schumacher, M. Van Borren, C. Belterman, R. Coronel, and J. Fiolet, "Increased na+/h+-exchange activity is the cause of increased [na+] i and underlies disturbed calcium handling in the rabbit pressure and volume overload heart failure model," *Cardiovascular research*, vol. 57, no. 4, pp. 1015–1024, 2003. [Online]. Available: https://doi.org/10.1016/S0008-6363(02)00809-X 102, 103

[120] D. A. Brown, M. A. Aon, F. G. Akar, T. Liu, N. Sorarrain, and B. O'Rourke, "Effects of 4-chlorodiazepam on cellular excitation–contraction coupling and ischaemia–reperfusion injury in rabbit heart," *Cardiovascular research*, vol. 79, no. 1, pp. 141–149, 2008. [Online]. Available: https://doi.org/10.1093/cvr/cvn053 102, 103

[121] R. D. Simitev, R. J. Gilchrist, R. C. Myles, F. L. Burton, and G. L. Smith, "Code and data for estimation of parameters in mathematical models of myocyte action potentials (20240514t1350)," 2024. [Online]. Available: https://doi.org/10.5281/zenodo.11191649 114

[122] G. R. Mirams, Y. Cui, A. Sher, M. Fink, J. Cooper, B. M. Heath, N. C. McMahon, D. J. Gavaghan, and D. Noble, "Simulation of multiple ion channel block provides improved early prediction of compounds' clinical torsadogenic

risk," *Cardiovascular research*, vol. 91, no. 1, pp. 53–61, 2011. [Online]. Available: https://doi.org/10.1093/cvr/cvr044 135

[123] M. P. Nash and A. V. Panfilov, "Electromechanical model of excitable tissue to study reentrant cardiac arrhythmias," *Progress in Biophysics and Molecular Biology*, vol. 85, no. 2, pp. 501–522, 2004, modelling Cellular and Tissue Function. [Online]. Available: https://www.sciencedirect.com/science/article/pii/S0079610704000239 145

[124] R. H. Clayton *et al.*, "Models of cardiac tissue electrophysiology: Progress, challenges and open questions," *Progress in Biophysics and Molecular Biology*, vol. 104, pp. 22–48, 2011. [Online]. Available: https://doi.org/10.1016/j.pbiomolbio.2010.05.008 145

[125] C. Alexander, M. J. Bishop, R. J. Gilchrist, F. L. Burton, G. L. Smith, and R. C. Myles, "Initiation of ventricular arrhythmia in the acquired long qt syndrome," *Cardiovascular Research*, vol. 119, no. 2, pp. 465–476, 2023. [Online]. Available: https://doi.org/10.1093/cvr/cvac103 145